Design of Active and Passive Photonic Components for an Optical Transmitter in Silicon-on-Insulator Technology

Von der Fakultät Informatik, Elektrotechnik und Informationstechnik
der Universität Stuttgart zur Erlangung der Würde eines
Doktor-Ingenieurs (Dr.-Ing.) genehmigte Abhandlung

Vorgelegt von
María Félix Rosa
aus Madrid

Hauptberichter:	Prof. Dr.-Ing. Manfred Berroth
Mitberichter:	Prof. Dr.-Ing. Norbert Frühauf
Tag der mündlichen Prüfung:	19. Dezember 2022

Institut für Elektrische und Optische Nachrichtentechnik
der Universität Stuttgart

2022

Contents

Abbreviations and Constants

Abbreviations

Abbreviation	*Description*
1D	One-dimensional
1DGC	One-dimensional grating coupler
1DGCS	One-dimensional grating coupler working as polarization splitter
2D	Two-dimensional
2DFGC	Two-dimensional focusing grating coupler
2DGC	Two-dimensional grating coupler
2DGCS	Two-dimensional grating coupler working as polarization splitter
2DPDC	Two-dimensional polarization diversity coupler
3D	Three-dimensional
ADC	Analog-to-digital converter
ADS	Advanced Design System (Commercial software)
Al	Aluminum
AlSiCu	Aluminum-silicon-copper
BCB	Benzocyclobutene
BOX	Buried oxide
BPSK	Binary phase-shift keying
BW	Bandwidth
CMOS	Complementary metal-oxide-semiconductor
CPW	Coplanar waveguide
DPSK	Differential phase-shift keying
DP-QPSK	Dual polarization quadrature phase-shift keying
DUT	Device under test
EO	Electro-optical
EPIC	Electronic-photonic integrated circuit
ER	Extinction ratio
EDFA	Erbium doped fiber amplifier

FDTD	Finite-difference time-domain
FEM	Finite element method
GC	Grating coupler
GSG	Ground-signal-ground
IHP	Leibniz Institute for High Performance Microelectronics
IL	Insertion loss
IMS CHIPS	Institut für Mikroelektronik Stuttgart
InP	Indium phosphide
i-Si	Intrinsic silicon
LED	Light-emitting diode
LO	Local oscillator
MMI	Multimode interference coupler
MoM	Method of moments
MZI	Mach-Zehnder interferometer
MZM	Mach-Zehnder modulator
NRZ	Nonreturn-to-zero
OOK	On-off keying
PC	Personal computer
PCF	Photonic crystal fiber
PMF	Polarization-maintaining fiber
QAM	Quadrature amplitude modulation
QPSK	Quadrature phase-shift keying
RF	Radio frequency
SEM	Scanning electron microscope
Si	Silicon
SiO_2	Silicon dioxide
SMF	Single mode fiber
SOI	Silicon-on-insulator
TE	Transversal electric
TIA	Transimpedance amplifier
TIR	Total internal reflection
TL	Transmission line
TM	Transversal magnetic
TWE	Traveling wave electrode
VNA	Vector network analyzer

Constants

Constant	*Description*
c_0	Speed of light in vacuum, $c_0 = 2.99792\ldots \cdot 10^8\ \frac{\mathrm{m}}{\mathrm{s}}$
e	Euler's number, $e = 2.71828\ldots$
j, i	Imaginary unit, $j^2 = i^2 = -1$
π	Pi, $\pi = 3.14159\ldots$
q	Elementary charge, $q = 1.60218\ldots \cdot 10^{-19}\,\mathrm{C}$
ϵ_0	Permittivity in vacuum, $\epsilon_0 = 8.85419\ldots \cdot 10^{-12}\ \frac{\mathrm{F}}{\mathrm{m}}$
μ_0	Permeability in vacuum, $\mu_0 = 1.25664\ldots \cdot 10^{-6}\ \frac{\mathrm{H}}{\mathrm{m}}$

Zusammenfassung

Diese Ausarbeitung stellt Forschungsarbeiten an aktiven und passiven nanooptischen Strukturen mit Silizium-auf-Isolator-Technologie für die Hochgeschwindigkeitsdatenkommunikation dar. Die eingesetzte Technologie ist kostengünstig und CMOS-kompatibel. Somit ist die Integration von optischen und elektrischen Schaltungen auf demselben Chip möglich. Die Arbeit gliedert sich in zwei Teile, die die zwei untersuchten Strukturen vorstellen: den zweidimensionalen Gitterkoppler und den optischen Modulator.

Das erste Kapitel stellt die Motivation und die Ziele der Arbeit dar. Im zweiten Kapitel wird das Design sowie die Simulation der zweidimensionalen Gitterkoppler beschrieben. Hierbei handelt es sich um eine passive Struktur, die den Lichtstrahl aus der Glasfaser in den optischen Wellenleiter einkoppelt. Untersucht werden zweidimensionale Gitterkoppler mit orthogonalen und fokussierenden Gittern. Die geometrischen Parameter werden hinsichtlich höherer Kopplungseffizienz und Spaltung der zwei senkrechten Polarisierungen des eingekoppelten Lichts auf die zwei Ausgänge des Kopplers optimiert. Folglich entsteht zu jeder Polarisierung ein Informationskanal und dadurch wird die Datenrate verdoppelt. Für einen periodischen senkrechten zweidimensionalen Gitterkoppler wird eine simulierte Kopplungseffizienz von $-1,9\,\mathrm{dB}$ und $-2,1\,\mathrm{dB}$ für die TE- bzw. für die TM-Polarisierung erreicht. Die Kopplungseffizienz wird durch Verwendung aperiodischer Gitter erhöht, sodass eine simulierte Effizienz von $-1,7\,\mathrm{dB}$ für die TE-Polarisierung und von $-1,9\,\mathrm{dB}$ für die TM-Polarisierung auf einer Telekommunikations-Wellenlänge von 1550 nm erreicht werden. Darüber hinaus werden fokussierende Gitterkoppler zwecks Flächenreduzierung der Kopplungsstruktur erstellt. Die räumlichen Parameter von Gitter und Taper werden auf maximale Kopplungseffizienz optimiert. In diesem Zuge werden angepasste Taper für jedes fokussierende Gitter entwickelt. Das Design und die Simulation unterschiedlicher fokussierender Gitterkoppler und Taper werden vorgestellt. Erreicht wird eine gesamte Kopplungseffizienz von $-3,1\,\mathrm{dB}$ und eine 1 dB-Bandbreite von 40 nm, mit einem Gitterkoppler dessen Seitenlängen weniger als $13\,\mu\mathrm{m}$ breit sind und mit einem angepassten Taper von $26,2\,\mu\mathrm{m}$. Die Kopplungseffizienz beträgt bei Verwendung eines $100\,\mu\mathrm{m}$ langen adiabatischen Tapers $-2,4\,\mathrm{dB}$. Dies stellt ein vielversprechendes Ergebnis im Hinblick auf vergleichbare Strukturen mit sich verjüngenden Wellenleitern dar. Zum Ende dieses

Kapitels werden Messergebnisse von speziell gefertigten zweidimensionalen fokussierenden Gitterkopplern mit angepasstem Taper vorgestellt. Für die Designvalidierung wird eine Prototypenstruktur vom Institut für Mikroelektronik Stuttgart (IMS CHIPS) hergestellt. Durch Hinzufügen eines Metallspiegels auf der Rückseite, um Lichtverluste ins Substrat zu vermeiden und somit die Kopplungseffizienz zu erhöhen, kann diese Struktur zukünftig optimiert werden.
Das dritte Kapitel behandelt die Lichtmodulation durch elektrische Signale mittels der entwickelten aktiven optischen Struktur. Schlüsselparameter für die Auslegung dieser Struktur wie geometrische Dimensionen, Dotierungsprofil und elektrische Eigenschaften sowie deren Einfluss auf die Modulatorleistung werden detailliert beschrieben. Verschiedene Modulatoren werden zusammen mit unterschiedlichen optischen und elektrischen Teststrukturen mit der neuen Technologie des IMS CHIPS fabriziert. Der erste gefertigte optische Modulator mit dieser Technologie wird erfolgreich charakterisiert. Hierbei handelt es sich um einen Mach-Zehnder-Modulator, der eine gemessene Modulationseffizienz von $3,1\,\mathrm{Vcm}$ bei $2\,\mathrm{V}$ Sperrspannung aufweist. Die On-Chip-Einfügedämpfung beträgt $4,2\,\mathrm{dB}$ für den Betriebspunkt mit der maximalen Lichtabsorption. Koplanare Leitungen mit einer $3\,\mathrm{dB}$-Bandbreite größer als $50\,\mathrm{GHz}$ werden entwickelt und gemessen, um als Wanderwellenelektrode des Modulators verwendet zu werden. Der Einfluss des Phasenschiebers des Modulators unterhalb der Leitung wird analysiert und durch einen äquivalenten Schaltkreis modelliert. Die koplanare Leitung des Modulators wird charakterisiert. Die Messungen zeigen eine $3\,\mathrm{dB}$-Bandbreite von $27\,\mathrm{GHz}$ und eine $6\,\mathrm{dB}$-Bandbreite von $30\,\mathrm{GHz}$ mit einer Sperrspannung von $2\,\mathrm{V}$. Letztere entspricht theoretisch der $3\,\mathrm{dB}$ elektro-optischen Bandbreite des Modulators.
Außerdem werden Modulatoren und Teststrukturen in einer zusätzlichen Technologie mit $220\,\mathrm{nm}$ Silizium-auf-Isolator-Substrat am Leibniz-Institut für innovative Mikroelektronik (IHP) simuliert und hergestellt. Optische und elektrische Messungen der relevantesten Designs werden vorgestellt. Für einen Push-Pull-Modulator mit einer $6\,\mathrm{dB}$-Bandbreite der Wanderwellenelektrode von $10\,\mathrm{GHz}$ wird eine Modulationseffizienz von $0,25\,\mathrm{Vcm}$ unter $2\,\mathrm{V}$ Sperrspannung nachgewiesen.
Abschließend werden die wichtigsten Ergebnisse als Fazit hervorgehoben und ein Ausblick für weitere, auf dieser Arbeit aufbauende Untersuchungen gegeben.

Abstract

This work presents research on active and passive nanooptical structures on silicon-on-insulator technology for high speed data communication. The utilized technology is cost efficient and complementary metal-oxide-semiconductor (CMOS) compatible allowing the integration of optical and electrical circuits on the same die. The work consists of two parts presenting the two main structures that are investigated: the two-dimensional grating coupler and the optical modulator.

The first chapter introduces the motivation and the goal of the work. The second chapter describes the design and simulation of two-dimensional grating couplers. This is a passive structure used to couple light from the optical fiber into the optical waveguides embedded on a die. Two-dimensional grating couplers with an orthogonal and a focusing grid are investigated. The geometrical parameters of the structure are optimized to achieve high coupling efficiencies and enable the splitting of the two orthogonal polarizations of the input light, i.e. the transversal electric (TE) from the transversal magnetic (TM) polarization, into the two outputs of the coupler. This allows the transmission of one information channel at each polarization increasing the data rate. For periodic orthogonal two-dimensional grating couplers a simulated coupling efficiency of $-1.9\,\mathrm{dB}$ and $-2.1\,\mathrm{dB}$ are achieved for TE and TM polarizations, respectively. The coupling efficiency is enhanced by the use of an aperiodic grating achieving a simulated coupling efficiency of $-1.7\,\mathrm{dB}$ for TE and $-1.9\,\mathrm{dB}$ for TM polarization at the telecommunication wavelength of $1550\,\mathrm{nm}$. In addition, two-dimensional focusing grating couplers are designed in order to reduce the area of the coupling structure. The spatial dimension of the grating and the taper, used to guide the optical signal from the grating coupler to a single mode waveguide, are optimized maximizing the coupling efficiency. Customized tapers are developed for each focusing grating design. The design and simulation of different focusing grating couplers and tapers are presented achieving a total coupling efficiency of $-3.1\,\mathrm{dB}$ and a $1\,\mathrm{dB}$-bandwidth of $40\,\mathrm{nm}$ with a grating coupler with a side width of less than $13\,\mu\mathrm{m}$ and a customized taper of $26.2\,\mu\mathrm{m}$. Using an adiabatic taper with a length of $100\,\mu\mathrm{m}$, the coupling efficiency is $-2.4\,\mathrm{dB}$, which is a promising result for a comparably structure which includes the tapered waveguide. At the end of the chapter the measurement re-

sults of a fabricated two-dimensional focusing grating coupler with customized taper is presented. A prototypical structure is fabricated at *Institut für Mikroelektronik Stuttgart* (IMS CHIPS) for design validation, which can be optimized in future adding a backside metal mirror to avoid light losses into the substrate increasing the coupling efficiency.
The third chapter concentrates on the modulation of light by applying an electrical signal by means of the designed active optical structure. Key parameters for the design of these structures as the geometrical dimensions, the doping profile and the electrical properties are described in detail as well as the impact on the performance of the modulator if these parameters are modified. Different designs of modulators together with various optical and electrical test structures are fabricated with the novel technology of IMS CHIPS. The first fabricated optical modulator using this technology is successfully measured. This is a Mach-Zehnder modulator which exhibits a measured modulation efficiency of 3.1 Vcm at 2 V reverse bias voltage. The total insertion loss on-chip is 4.2 dB for the operating point with the maximum absorption of light. Transmission lines with a 3 dB electrical bandwidth higher than 50 GHz are designed and measured to be used as traveling wave electrode of the modulator. The influence of the phase shifter of the modulator below the transmission lines is analyzed and an equivalent circuit model is developed. The electrical coplanar lines of the modulator are measured showing a 3 dB electrical bandwidth of 27 GHz and a 6 dB electrical bandwidth of 30 GHz at 2 V reverse bias voltage, which theoretically corresponds with the 3 dB electro-optical bandwidth of the modulator. Additionally, modulators and test structures are designed and fabricated in a different technology with a 220 nm silicon-on-insulator substrate at the Leibniz Institute for High Performance Microelectronics (IHP). Optical and electrical measurements of the most relevant designs are presented. A modulation efficiency of 0.25 Vcm at 2 V bias voltage is demonstrated for a push-pull modulator with a 6 dB electrical bandwidth of the traveling wave electrode of 10 GHz.
Finally, the most important results are outlined as conclusion and an outlook for further investigations based on the research of this work is given at the end of the thesis.

1 Introduction

1.1 Motivation

Nowadays, the increasing data rates in backhaul nets demand the development of high speed optical links in the 100 Gb/s range. For the transmission and detection of a high data rate optical signal, the development of high performance optoelectronics circuits is required. This thesis focuses on the transmitter side of the optical link. Besides of the bandwidth and efficiency of the devices, important aspects for the industry are the cost and the fabrication complexity. Therefore, this research is based on the design of photonic structures on a cost effective silicon (Si) platform simplifying the fabrication method by limiting the number of mask layers used in the photolithographic and doping process.
A high speed data link can be achieved by using a high speed dual polarization quadrature phase-shift keying (DP-QPSK) modulator as transmitter and an optical coherent receiver for dual polarization multiplex signals. A scheme of a DP-QPSK optical communication link is presented in Figure 1.1.

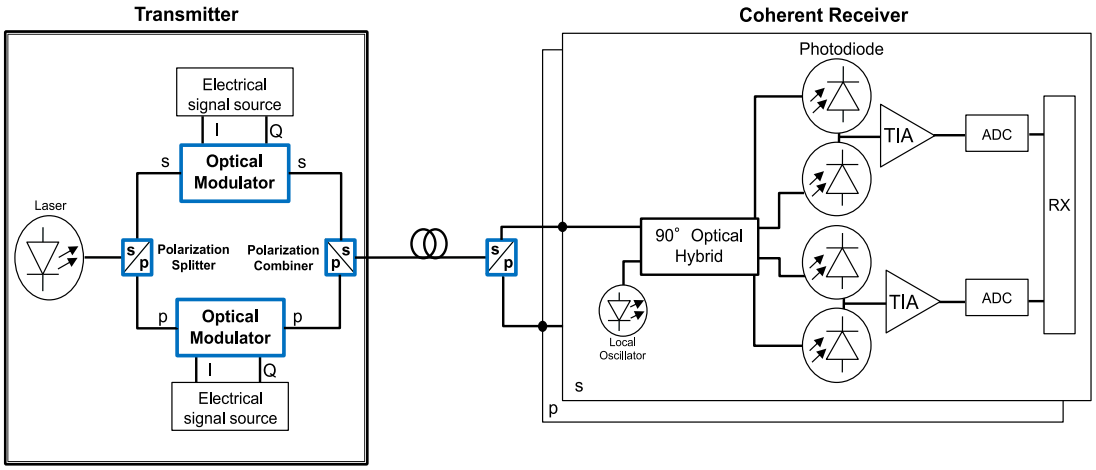

Figure 1.1: Block diagram of a DP-QPSK optical communication link for high data rates.

The DP-QPSK optical modulator is a device composed of passive and active photonic structures. Firstly, the light coming from a laser is split into two orthogonal polarizations,

s- and p-polarization. Afterwards, each polarization is sent to an optical modulator where the phase is shifted by applying an electrical signal. Then, the two optical paths are again combined by means of a polarization combiner. Thereby, the transmission of symbols per time unit is duplicated, since different information can be sent on each of the two orthogonal polarizations of the light. On the receiver side, the polarizations are split again. A 90° multimode interferometer can be used to transmit the 90° shifted symbols through different optical paths to be detected later by photodiodes. The optical signal is changed to an electrical signal and it is amplified by a transimpedance amplifier (TIA). Finally, the signal is sent to an analog-to-digital converter (ADC) and is processed by a digital electrical receiver.

1.2 Objective

The goal of this work is the development of a high performance polarization splitter and combiner and a high speed optical modulator, highlighted in Figure 1.1. In order to reduce the complexity of the transmitter, the target is to use the same modulator for both optical paths of the orthogonal polarizations. That means, the polarization splitter has to separate the two polarizations and additionally convert one of them into the other. Hence, the same optical modulator, optimized for only one polarization, can be used for both paths. Besides, the same design can be used as polarization combiner, since the functionality of the structure is bidirectional. The embedded structures are developed using a silicon-on-insulator (SOI) platform avoiding other more expensive materials such as indium phosphide (InP).

2 Two-dimensional grating couplers

Over the last years, integrated silicon photonic circuits have been developed and improved for their application in data communication technology. The SOI technology appears as the best solution to fabricate photonic devices due to the compatibility of the low cost complementary metal-oxide-semiconductor (CMOS) fabrication process and the large refractive index difference between Si and silicon dioxide (SiO_2). Over the last decade, a significant progress has been achieved improving the performance of active and passive silicon photonic devices such as coupling structures, photodetectors, waveguides or modulators. However, there are still some problems regarding this technology. The reduction of size implies a challenge on the coupling process of the light between the optical fiber and the embedded Si waveguide. The diameter of the single mode fiber (SMF) core is around 10 µm. However, a standard single mode SOI-waveguide has a width and a height of around 400 nm and 250 nm, respectively. Another important feature is the polarization dependence of the optical devices, which is why most of the silicon circuits are only optimized for one polarization. One approach to solve the coupling problem is the use of grating couplers (GC). These Bragg structures are able to diffract the incident vertical light coming from the fiber into the horizontal integrated waveguides. Those couplers are compact structures which can efficiently couple the incident light on chip. Going even further in the design of grating structures, two-dimensional grating couplers are a solution to solve both mentioned problems. On the one hand, the coupling of light and on the other hand, the polarization dependence. These structures couple and split two orthogonal fiber polarizations, s and p, into two transversal electric (TE) waveguide modes. The optimization of these structures has become a challenge in the design of GCs. In this work, different designs are presented to achieve a high coupling efficiency of two orthogonal polarizations with a high extinction ratio and a wide optical bandwidth (BW).

2.1 Theoretical fundamentals

2.1.1 Plane waves

The basics of electrodynamics including electromagnetic waves is described with Maxwell's equations [1]:

$$\nabla \times \vec{E} + \frac{\partial \vec{B}}{\partial t} = 0, \tag{2.1}$$

$$\nabla \times \vec{H} - \frac{\partial \vec{D}}{\partial t} - \vec{J} = 0, \tag{2.2}$$

$$\nabla \cdot \vec{D} = \rho_v, \tag{2.3}$$

$$\nabla \cdot \vec{B} = 0. \tag{2.4}$$

Where $\vec{E}$ and $\vec{H}$ are the electric and magnetic field, respectively. The electric flux density is described by $\vec{D}$. The magnetic flux density is given by $\vec{B}$.

Equation 2.1 is Faraday's law that describes how a changing magnetic flux induces an electric field and vice versa. This electric field induces a current flow in conductors. The induced current produces a secondary magnetic field that counteracts the change in the primary magnetic field.

Ampère-Maxwell's law is given by Equation 2.2. It describes the magnetic field produced by a time varying electric displacement field and the current density $\vec{J}$.

Equation 2.3 is known as Gauss's law. It describes the behavior of the electric field $\vec{E}$ around electric charges. It can be expressed in terms of the electric flux density and the electric charge density ρ_v. If no charges are present $\rho_v = 0$.

Gauss's law for magnetism is defined by Equation 2.4. This law states that the magnetic flux across any closed surface is zero, which means that there are no magnetic monopoles.

The following equations include the properties of the materials:

$$\vec{D} = \epsilon_0 \vec{\vec{\epsilon}}_\mathrm{r} \vec{E}, \tag{2.5}$$

$$\vec{B} = \mu_0 \vec{\vec{\mu}}_\mathrm{r} \vec{H}, \tag{2.6}$$

$$\vec{J} = \vec{\vec{\sigma}}\vec{E}. \tag{2.7}$$

Where ϵ_0 and μ_0 are the dielectric and magnetic constant in free space and ϵ_r and μ_r are the relative permittivity and permeability of the medium, respectively. The conductivity is defined by σ.
Assuming a linear, isotropic and homogeneous medium, Equations 2.5, 2.6 and 2.7 are simplified to

$$\vec{D} = \epsilon_0\epsilon_\mathrm{r}\vec{E}, \tag{2.8}$$

$$\vec{B} = \mu_0\mu_\mathrm{r}\vec{H}, \tag{2.9}$$

$$\vec{J} = \sigma\vec{E}. \tag{2.10}$$

For nonmagnetic materials the permeability is $\mu_\mathrm{r} = 1$. The conductivity σ is negligible for materials where the electrical current cannot flow freely, like insulators.
For plane waves, the electromagnetic field can be described in Cartesian coordinates where the field has a component in the x- and y-direction and the propagation is along the z-direction.
Assuming the previous definition of the plane wave, the electric field and the polarization of the light can be described as follows: The polarization of the wave refers to the orientation of the oscillation of the electromagnetic field. In optical communications, polarization commonly refers to the specific polarization of the electric field. The oscillation of the field can point in a single direction, which is called linear polarization, or rotational, known as circular or elliptical polarization. The electric field is given as

$$\vec{E}(x,y,z,t) = E_\mathrm{x0} \cdot e^{i(wt-kz+\varphi_x)}\hat{x} + E_\mathrm{y0} \cdot e^{i(wt-kz+\varphi_y)}\hat{y}, \tag{2.11}$$

where E_x0 is the x-component and E_y0 is the y-component of the electric field. The wave number is determined by $k = |\vec{k}|$, where $\vec{k}$ is the wave vector, which is perpendicular to the surface of constant phase of the wave. For isotropic media, the direction of the wave vector is the same as the direction in which the wave propagates. The angular frequency is denoted by w and the time by t. The phase difference between the electric field components is defined by $\varphi = \varphi_x - \varphi_y$. For the linear polarization $\varphi = 0$. However, for circular polarization $\varphi = \pi/2$ and $E_{x0} = E_{y0}$, otherwise it is defined as elliptical polarization.

Considering a coordinate system related to the plane of incidence of the optical wave, if the electric field component is perpendicular to this plane, the wave is denominated TE polarized. If the H-field is perpendicular to the incidence plane (E-field parallel to the incident plane), it is called transversal magnetic (TM) polarized wave. Figure 2.1 shows a graphical representation of TE and TM polarizations, where the plane of incidence is parallel to a substrate where an optical waveguide is etched for guiding light along a photonic integrated circuit.

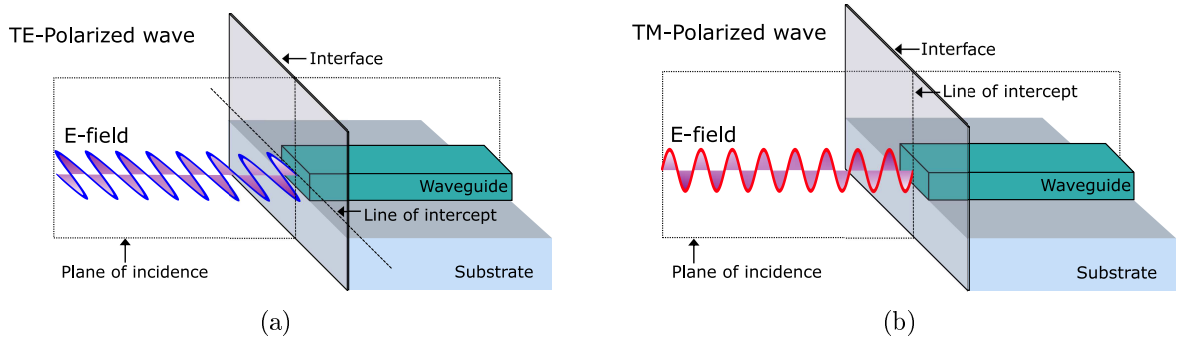

Figure 2.1: (a) TE polarization. (b) TM polarization.

When an optical wave travels along different materials, optical effects that determine the propagation of light must be considered. Basically, these phenomena can be described by reflection, refraction and diffraction.

2.1.2 Reflection and refraction

Reflection occurs when an optical wave traveling through a material with a refractive index n_1 (medium 1), bounces off at the interface of a second material with a different refractive index n_2 (medium 2). The angle of incidence is denoted by α_i. Being $\alpha_\mathrm{i} = 0$ the angle of the incident light perpendicular to the interface between the two materials. The light is reflected at the same angle as the incidence angle: $\alpha_\mathrm{i} = \alpha_\mathrm{r}$ as shown in Figure 2.2. Depending on the material of the medium 2, the light can be completely reflected. For instance, this is the case for metals since they have a high reflectivity, reflecting almost all wavelengths in the visible and infrared range of the spectrum. Other materials allow that the light passes through them. In that case, an additional phenomenon called refraction can be observed. The propagation angle of the incident light is bent away from the normal, when the light passes through a medium 2 with a refractive index lower than the one of medium 1, i.e. $n_1 > n_2$. This effect is described by Snell's law (Equation 2.12).

The change of medium implies a change of the phase velocity v_{ph} of the light defined by Equation 2.13. Being c_0 the speed of light in vacuum and α_{R} the angle of the refracted light with respect to the normal of the interface between the two media.

$$n_1 \cdot \sin \alpha_{\mathrm{i}} = n_2 \cdot \sin \alpha_{\mathrm{R}}, \tag{2.12}$$

$$v_{\mathrm{ph}} = \frac{c_0}{\sqrt{\epsilon_{\mathrm{r}} \mu_{\mathrm{r}}}} = \frac{c_0}{n}. \tag{2.13}$$

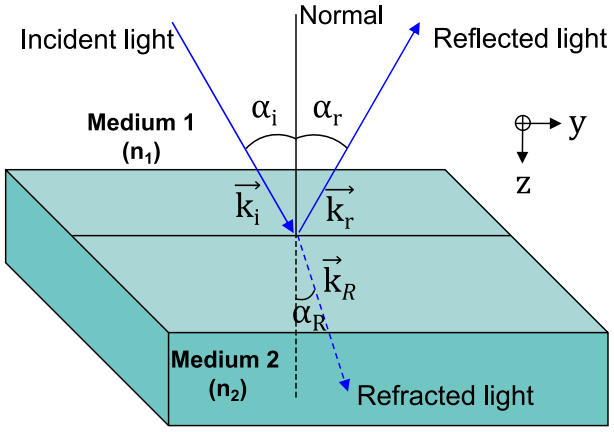

Figure 2.2: Scheme of the reflection and refraction phenomena of light.

The electric field of the incident, reflected and refracted waves can be described by

$$\vec{E_{\mathrm{i}}} = \vec{E_{\mathrm{i0}}} \cdot e^{i(w_{\mathrm{i}} t - \vec{k_{\mathrm{i}}} \vec{r})}, \tag{2.14}$$

$$\vec{E_{\mathrm{r}}} = \vec{E_{\mathrm{r0}}} \cdot e^{i(w_{\mathrm{r}} t - \vec{k_{\mathrm{r}}} \vec{r})}, \tag{2.15}$$

$$\vec{E_{\mathrm{R}}} = \vec{E_{\mathrm{R0}}} \cdot e^{i(w_{\mathrm{R}} t - \vec{k_{\mathrm{R}}} \vec{r})}, \tag{2.16}$$

where $\vec{r} = (x, y, z)$ is the position vector. Based on Figure 2.2 the wave vectors are

$$\vec{k_{\mathrm{i}}} = n_1 k_{\mathrm{i}} \sin(\alpha_{\mathrm{i}}) \hat{y} + n_1 k_{\mathrm{i}} \cos(\alpha_{\mathrm{i}}) \hat{z}, \tag{2.17}$$

$$\vec{k_{\mathrm{r}}} = n_1 k_{\mathrm{r}} \sin(\alpha_{\mathrm{r}}) \hat{y} - n_1 k_{\mathrm{r}} \cos(\alpha_{\mathrm{r}}) \hat{z}, \tag{2.18}$$

$$\vec{k_{\mathrm{R}}} = n_2 k_{\mathrm{R}} \sin(\alpha_{\mathrm{R}}) \hat{y} + n_2 k_{\mathrm{R}} \cos(\alpha_{\mathrm{R}}) \hat{z}. \tag{2.19}$$

At the interface of medium 1 and medium 2, the continuity conditions for the tangential and the normal fields have to be fullfilled [2]:

$$\vec{E}_{1,\tan} = \vec{E}_{2,\tan}, \tag{2.20}$$

$$\vec{H}_{1,\tan} = \vec{H}_{2,\tan}, \tag{2.21}$$

$$\vec{D}_{1,\mathrm{norm}} = \vec{D}_{2,\mathrm{norm}}, \tag{2.22}$$

$$\vec{B}_{1,\mathrm{norm}} = \vec{B}_{2,\mathrm{norm}}. \tag{2.23}$$

These conditions must be fulfilled at the interface for any arbitrary time t, therefore the angular frequency of the incident, refracted and reflected waves is the same $w = w_\mathrm{i} = w_\mathrm{r} = w_\mathrm{R}$. Considering these conditions and the law of conservation of energy, the electric field for a TE wave, i.e. the electric field is perpendicular to the propagation direction, at the interface ($z = 0$) is given by

$$E_{\mathrm{i}0} \cdot e^{-in_1 k_\mathrm{y} \sin\alpha_\mathrm{i}} \hat{x} + E_{\mathrm{r}0} \cdot e^{-in_1 k_\mathrm{y} \sin\alpha_\mathrm{r}} \hat{x} = E_{\mathrm{R}0} \cdot e^{-in_2 k_\mathrm{y} \sin\alpha_\mathrm{R}} \hat{x}. \tag{2.24}$$

The reflected power P_r and refracted (transmitted) power P_R can be calculated using the ratios R and T of the reflected and transmitted power, repectively, to the incident power denoted by P_i. The ratios for the TE wave are:

$$R_\mathrm{TE} = \frac{P_\mathrm{r}}{P_\mathrm{i}} = \frac{{E_\mathrm{r}}^2}{{E_\mathrm{i}}^2} = \left(\frac{n_1 \cos\alpha_\mathrm{i} - n_2 \cos\alpha_\mathrm{R}}{n_1 \cos\alpha_\mathrm{i} + n_2 \cos\alpha_\mathrm{R}} \right)^2, \tag{2.25}$$

$$T_\mathrm{TE} = \frac{P_\mathrm{R}}{P_\mathrm{i}} = \frac{n_2 {E_\mathrm{R}}^2 \cos\alpha_\mathrm{R}}{n_1 {E_\mathrm{i}}^2 \cos\alpha_\mathrm{i}} = \frac{4n_1 \cos\alpha_\mathrm{i} \sqrt{{n_2}^2 - {n_1}^2 \sin^2\alpha_\mathrm{i}}}{(n_1 \cos\alpha_\mathrm{i} + \sqrt{{n_2}^2 - {n_1}^2 \sin^2\alpha_\mathrm{i}})^2}, \tag{2.26}$$

The power ratios for the TM wave are:

$$R_\mathrm{TM} = \left(\frac{n_2 \cos\alpha_\mathrm{i} - n_1 \cos\alpha_\mathrm{R}}{n_2 \cos\alpha_\mathrm{i} + n_1 \cos\alpha_\mathrm{R}} \right)^2, \tag{2.27}$$

$$T_\mathrm{TM} = \frac{4n_1 n_2^2 \cos\alpha_\mathrm{i} \sqrt{{n_2}^2 - {n_1}^2 \sin^2\alpha_\mathrm{i}}}{(n_2^2 \cos\alpha_\mathrm{i} + n_1 \sqrt{{n_2}^2 - {n_1}^2 \sin^2\alpha_\mathrm{i}})^2}. \tag{2.28}$$

2.1.3 Diffraction

An important phenomenon to understand the behavior of grating couplers is diffraction. This effect occurs when the electromagnetic wave encounters an object with dimensions comparable to the wavelength of the optical wave. There are two types of diffraction: Fraunhofer diffraction and Fresnel diffraction.
The Fraunhofer diffraction is observed, when both incident and diffracted waves are plane waves. This is the case, when the source of light and the screen, at which the diffraction pattern is formed, are placed at an infinite distance from the diffraction object. Fresnel diffraction can be observed, when the source and screen are at a finite distance from the diffraction object. The wave fronts leaving the object are spherical. Figure 2.3 shows the regions where the Fresnel and the Fraunhofer diffraction are valid. These two regions are limited by the Fresnel length r_{F}, which is given by

$$r_{\mathrm{F}} = \sqrt{\lambda\rho}, \tag{2.29}$$

where λ is the wavelength and ρ the distance from the field point to the center of the barrier (diffraction object) aperture . The Fresnel region is defined by $r_{\mathrm{F}} \ll x$ (near-field diffraction) and the Fraunhofer region by $r_{\mathrm{F}} \gg x$ (far-field diffraction), where x is the size of the aperture [3].

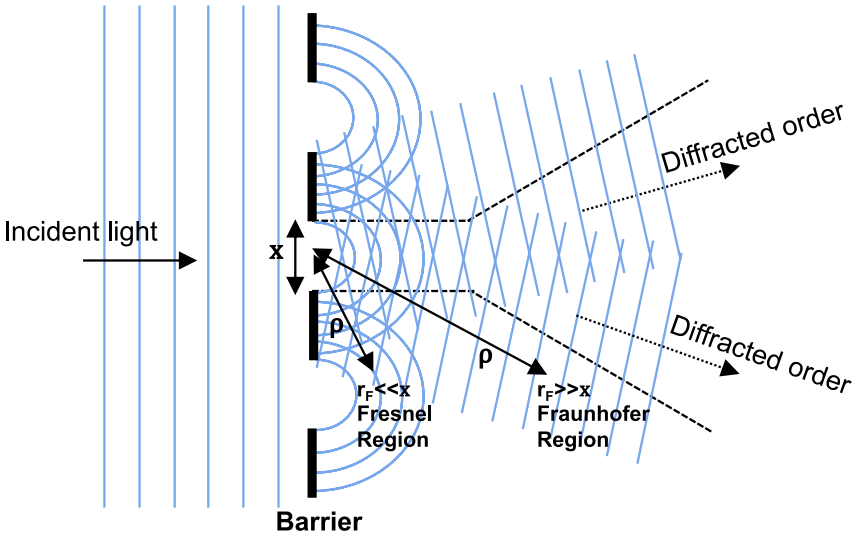

Figure 2.3: Fresnel and Fraunhofer diffraction regions [3].

To understand diffraction, it is important to describe the principle of interference of light. If two or more coherent monochromatic waves overlap, for example after being diffracted from two slits, while keeping a constant phase with respect to each other, constructive

and destructive interference occurs depending on the phase relationship. If the phase difference between the two original waves is an even or odd multiple of π, it is defined as constructive or destructive interference, respectively. The overlapping of the waves, when constructive interference occurs, produces a raise of the intensity distribution $I \propto |\vec{E}|^2$ of the original waves. However, the intensity of the resulting wave is lower than the original ones with the destructive interference.

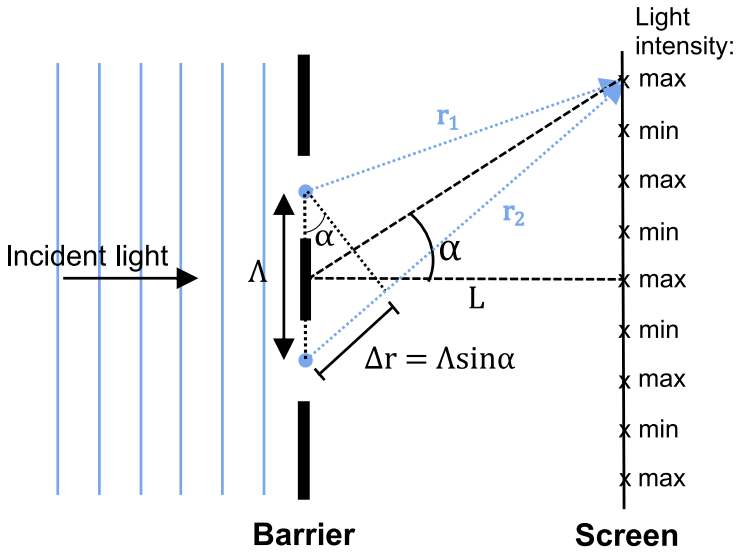

Figure 2.4: Scheme of the Young's double-slit experiment. Setup for the calculation of the optical path length difference Δr between two path lengths, e.g. r_1 and r_2. The barrier slits and the observation screen are separated a distance L (not to scale, $L \gg \Lambda$) [4].

As an example, Figure 2.4 shows the geometric description of a two slit construction, known as Young's double-slit experiment [4][5]. Here an observation screen is located at a distance L from the diffraction barrier with $L \gg \Lambda$, where Λ is the distance between the slits. Due to this condition, it can be assumed that the path lengths r_1 and r_2 are approximately parallel and the optical path length difference Δr is calculated as

$$\Delta r = r_2 - r_1 = \Lambda \sin \alpha. \tag{2.30}$$

When the light coming from the two slits interferes constructively, a bright band, called fringe, is observed at the screen. A dark fringe is the result of destructive interference. As shown in the diagram, the diffraction of the light due to the slits produces an interference pattern at the screen with maxima and minima of the light intensity.

The conditions for constructive interference assuming an initial phase difference $\Delta\varphi_0 = 0$ are:
The interfering waves shall have

- a phase difference of $2m\pi$ where m = 0, 1, 2, 3,...
- a path difference of $\Delta r = r_2 - r_1 = \Lambda \sin\alpha = m\lambda$, where m = 0, 1, 2, 3,...

The conditions for destructive interference assuming an initial phase difference of $\Delta\varphi_0 = 0$:
The interfering waves shall have

- a phase difference of $(2m+1)\pi$ where m = 0, 1, 2, 3,...
- a path difference of $\Delta r = \Lambda \sin\alpha = (2m+1)\frac{\lambda}{2}$, where m = 0, 1, 2, 3,...

The paths of the two waves emerging from the slits are represented in Figure 2.4 as r_1 and r_2, respectively. These two waves can be defined as

$$E_1 = E_0 \sin(wt), \tag{2.31}$$

and

$$E_2 = E_0 \sin(wt + \varphi). \tag{2.32}$$

The intensity of the resulting wave at any point in the Fraunhofer region can be expressed as

$$I \propto \left|\vec{E}\right|^2 = \left|\vec{E_1} + \vec{E_2}\right|^2, \tag{2.33}$$

$$I = I_1 + I_2 + 2\sqrt{I_1 I_2}\cos\varphi. \tag{2.34}$$

Where I_1 and I_2 are the intensity of the two original waves. It is assumed that the electric fields have the same initial phase $\Delta\varphi_0 = 0$, amplitude E_0, wavelength λ and angular frequency w. Due to the differences of the traveled path of the two waves, a phase difference of φ occurs between them at the screen. The resulting electric field of the two waves can be expressed as

$$E_{1+2} = 2E_0 \sin\Big(wt + \frac{\varphi}{2}\Big)\cos\Big(\frac{\varphi}{2}\Big), \tag{2.35}$$

and therefore the time average intensity of the overlapping waves is simplified to

$$I = I_0 \cos^2\Big(\frac{\varphi}{2}\Big) = I_0 \cos^2\Big(\frac{\pi \Lambda \sin\alpha}{\lambda}\Big). \tag{2.36}$$

Where I_0 is the maximum intensity of the overlapped waves. In addition, it is considered that the relation between the path difference and λ is the same as the one between the phase difference φ and 2π. This means,

$$\frac{\Delta r}{\lambda} = \frac{\varphi}{2\pi}. \tag{2.37}$$

Therefore, the phase difference can be expressed as

$$\varphi = \frac{2\pi}{\lambda} \Lambda \sin\alpha. \tag{2.38}$$

2.1.3.1 Diffraction gratings

A relevant application of diffraction is when an optical wave encounters a periodic array of diffracting elements resulting in a variation of the amplitude or phase of the transmitted wave's fields. This object is called diffraction grating. The two main categories of diffraction gratings are amplitude and phase gratings. Amplitude gratings have multiple slits as shown in Figure 2.3. Only the amplitude of the electromagnetic field of the transmitted wave is modulated by constructive and destructive interference. Phase gratings modulate only the phase of the transmitted wave. They have periodic ribs with a different refractive index than the surrounding medium. Some of the most common types of phase gratings are for example the binary, blazed or sinusoidal gratings [6].

The diffraction behavior of a GC can be described using the Bragg condition in Equation 2.39 [7][8].

$$k_{\mathrm{m,z}} = k_{\mathrm{in,z}} + m\frac{2\pi}{\Lambda}. \tag{2.39}$$

It describes the relation between the wave vector of the incident wave $\vec{k}_{\mathrm{in}}$ and the one of the diffracted waves $\vec{k}_{\mathrm{m}}$. Where $k_{\mathrm{in,z}}$ and $k_{\mathrm{m,z}}$ are the z-component of the incident and diffracted wave vector, respectively. The period of the one-dimensional (1D) grating along the z-direction is defined by Λ. The grating is formed by two media with different refractive indexes n_1 and n_2, where $n_2 > n_1$. The k-space diagram is shown in Figure 2.5(a).

To describe the propagation of the coupled light beam in a waveguide, the propagation

constant is introduced:

$$\beta_{\mathrm{m}} = k_0 n_{\mathrm{eff}} = \frac{2\pi n_{\mathrm{eff}}}{\lambda_0}, \tag{2.40}$$

where n_{eff} is the effective refractive index of the wave mode m and k_0 the wave number in free space. Equation 2.39 can be modified replacing the diffracted wave by the waveguide propagation constant β_{m}. Thereby, the dimensions of the grating can be adapted to be able to match the wave mode of the incident light to the propagating waveguide mode. A waveguide mode is defined as a transverse field pattern with a constant amplitude and polarization profile along the longitudinal direction of the waveguide. The equation becomes as follows

$$\beta_{\mathrm{m}} = k_{\mathrm{in}} \sin\alpha + m\frac{2\pi}{\Lambda}, \tag{2.41}$$

$$\frac{2\pi n_{\mathrm{eff}}}{\lambda_0} = k_{\mathrm{in}} \sin\alpha + m\frac{2\pi}{\Lambda}, \tag{2.42}$$

where k_{in} can be express as

$$k_{\mathrm{in}} = \frac{2\pi n_1}{\lambda_0}. \tag{2.43}$$

For the design of the grating coupler, the required grating period Λ can be obtained from Equation 2.42 and Equation 2.43 as

$$\Lambda = \frac{\lambda_0}{n_{\mathrm{eff}} - n_1 \sin\alpha}. \tag{2.44}$$

As shown in Figure 2.5(a), α is the angle of the oblique incident light with respect to the normal of the grating coupler. This diagram is a graphical representation of the Bragg condition, showing the wave vectors of the incident light and the different diffraction orders, in this example $m = 0, \pm 1$. It can be observed that for the solution $m = 0$ a part of the light power is reflected upwards and another part is transmitted into the substrate. The portion of the light power coupled into the waveguide corresponds to the diffraction order $m = 1$, whose waveguide propagation constant is $\beta_1 = k_{\mathrm{in}} \sin\alpha + \frac{2\pi}{\Lambda}$. The light coupled into the opposite direction (-z-direction) corresponds to the diffraction order $m = -1$.

A scheme with the power decomposition of a vertical GC is presented in Figure 2.5(b). Here, the principal light power loss of a fiber-to-chip coupling is illustrated. The light power coming from an optical fiber is defined as P_{in}. Part of this light is reflected at the

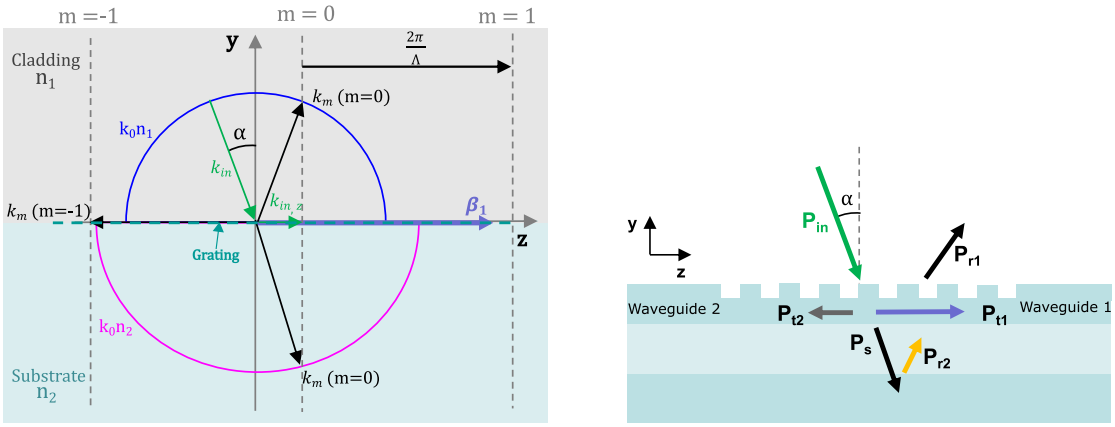

Figure 2.5: (a) Example of a k-space wave vector diagram showing the diffraction of an incident wave and the different possible diffraction order solutions. (b) Cross section of a grating coupler showing the principal components of the light power propagation for a fiber-to-chip coupling [7].

interface of the grating. The power loss due to reflection is corresponding to P_{r1}. The other part of the light is diffracted because of the grating structure. The power coupled into waveguide 1 is represented as P_{t1} and the one transmitted to waveguide 2 is defined as P_{t2}. Depending on the purpose of the optical circuit, P_{t2} can be considered as transmitted light or as undesired power loss: If the goal of the photonic circuit is the transmission into one single waveguide without any extra photonic components, e.g a power combiner between the waveguides 1 and 2, then P_{t2} is part of the light coupling losses. The light transmitted into the substrate P_{s} is also part of the losses, however some light can be reflected at the substrate interface, defined as P_{r2}. Different fabrication techniques can be used to increase the reflection at this interface and therefore improve the coupling efficiency of the grating. The coupling efficiency is defined as the ratio of the coupled optical power into the waveguide to the incident optical power coming from a fiber. An example of these fabrication techniques is the use of bottom mirrors as a distributed Bragg-reflector or a metal layer.

During this work, the impact of the dielectric layer thickness on the coupling efficiency, i.e. the distance between the substrate interface and the silicon grating, and the use of a metal mirror is investigated in chapter 2.4.

For chip-to-fiber coupling similar phenomena can be observed. Light propagates along the optical waveguide and when it reaches the grating structure, a diffraction effect occurs. In this case, second order diffraction leads to a back reflection into the waveguide ($-\beta_z$).

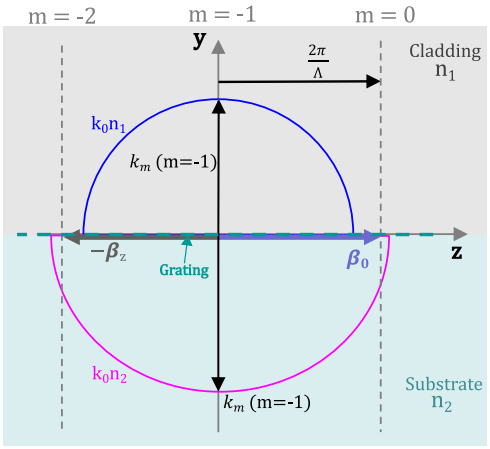

Figure 2.6: K-space wave vector diagram of a second order grating for a chip-to-fiber vertical coupling [7].

The first order diffraction is used for coupling the light into the optical fiber. This allows a perfectly vertical coupling out of the waveguide. However, it has to be taken into account that there is also a component that propagates downwards into the substrate and therefore contributes to the losses of the grating. The k-space diagram for this configuration is shown in Figure 2.6. The perfectly vertical coupling is produced when the propagation constant is $\beta = \frac{2\pi}{\Lambda}$. It can also be expressed as $\lambda_0 = n_{\text{eff}}\Lambda$. If the period of the grating is modified, the second order diffraction can be avoided. In this case, the fiber coupling is tilted, i.e. not exactly vertical, but the back reflections are diminished.

2.2 Numerical methods

Different numerical methods can be used for the design and simulation of grating couplers [9]. The Floquet-Bloch theorem considers the grating structure as an infinite number of repetitions reducing the complexity of the calculations. This is a rigorous method whose results are valid for infinite gratings, but at the edges of the structure, i.e. a finite grating, a mode mismatch between the results of the Bloch mode and the real mode can be observed [10] [11]. One of the most commonly used methods for simulating grating couplers or other optical structures, e.g. sublambda waveguides or tapers, is the eigenmode expansion method [12]. This method is based on the decomposition of the electromagnetic fields into local eigenmodes, which are the solutions of the Maxwell's equations in each local cross section of the simulated device. The structure is divided into sections and analyzed as a two-dimensional (2D) structure. For each section, the guided modes and the radiation modes, i.e. modes which are not confined in the waveguide core,

are calculated. The refractive index does not vary along the propagation direction in these sections. The scattering matrix is calculated at the interfaces of the sections allowing the calculation of the total transmission and reflection of the structure. Some of the simulation tools that apply this method are CAMFR [13] or FIMMPROP [14]. During this work, FIMMPROP has been used to design, simulate and study the waveguide modes.
Most of the optical simulations realized for this work are done using the finite-difference time-domain (FDTD) method. With the FDTD two and also three-dimensional (3D) structures can be simulated with very accurate results. However, this method needs more computation time. The FDTD simulations are realized with the software tool FullWAVE [15] of Synopsys' RSoft. This tool performs a full-vector simulation of the photonic structures, allowing the study of light propagation characteristics and losses along devices with arbitrary geometries, complex material definitions and no uniform grids. The analysis of coupling efficiency and bandwidth of 2D grating couplers or the losses of tapers presented in the following chapters are realized with the help of this tool. Besides, the combination of MATLAB and FullWAVE is used for the simulation of complex designs. For example, the layout of the aperiodic grating coupler is generated by MATLAB and later imported to RSoft to be simulated. This allows the optimization of aperiodic 2D gratings using, e.g. a genetic algorithm, by means of an automatized and faster process. The genetic algorithm [16] is based on the natural selection process of the biological evolution. The algorithm generates a population of individual solutions. At each iteration, individuals of the population are randomly chosen to create the next generation as children of the selected individuals. After successive iterations of the algorithm, the population converges to an optimal solution. The results of this process are shown in chapter 2.4.2.1.

2.3 State of the art

An overview of the most relevant GCs published to date is summarized in Table 2.1. The target of diffraction gratings is to achieve a high coupling efficiency, over a wide optical bandwidth, resulting in a high efficiency-bandwidth product. GCs are realized using different SOI-technologies. The main parameters that describe the dimensions of the published structures are summarized in Table 2.1. These are: the thickness of the top active silicon layer, the radius of the etched holes in the active Si, the grating period and the etching depth of the gratings. In addition, some of the designs include a bottom reflector under the buried oxide (BOX) layer in order to enhance the light coupling efficiency of the structure.

Many GCs are realized based on the one-dimensional grating coupler (1DGC) fabricated by etching periodic [17] or aperiodic [18][19][8][20][21] lines in the top Si layer. Some of these structures achieve coupling efficiencies better than $-1\,\mathrm{dB}$ and are designed to couple only one specific optical polarization, i.e. TE or TM. Other studies are realized based on 1DGC, where both TE and TM polarizations are coupled at the same time and transmitted into different waveguides. These structures are referred to as one-dimensional grating coupler working as polarization splitter (1DGCS) [22]. The polarization dependence of the 1DGC can be solved by the use of a more complex design, the two-dimensional grating coupler (2DGC). These structures are fabricated by etching holes in the top Si layer based on the idea of the superposition of two orthogonal 1D gratings. These structures can be classified as 2D polarization diversity couplers (2DPDC) and 2D grating couplers working as polarization splitters (2DGCS). The 2DPDC couples all input polarizations as TE polarization waves into two integrated Si waveguides. Therefore, their coupling efficiency is defined as the sum of the two outputs [23][24][25][26]. On the other hand, the 2DGCS couples the TE polarization into one waveguide and the TM polarization is inherently rotated and coupled as TE into the other waveguide. Consequently, their coupling efficiency is defined as the output power for each polarization in the corresponding waveguide [27][28][29][30]. Experimentally, a 2DGCS with periodic grating with etched cylindrical holes has been demonstrated in [27]. Other more complex approaches show an enhanced coupling efficiency using different grating designs and techniques as square lattice formed by 5 cylinder-holes per grating cell [28], a two-step etching process to build an apodized squared grating [30] or the use of a benzocyclobutene (BCB) bonding technology and a backside metal mirror [29]. The 2DGCS is the structure designed and optimized in this work. The different designs are presented in two chapters depending on the position and hence the periodicity of the etched holes. These are: the orthogonal grating in chapter 2.4, where the holes are located orthogonal to each other and the focusing grating in chapter 2.5, where the holes are placed in an elliptical fashion.

Table 2.1: State of the art of 1D and 2D grating couplers.

Name	Top Si thickness [nm]	Radius [nm]	Period [nm]	Etching depth [nm]	Coupling efficiency [dB]	Wavelength [nm]	1-dB BW [nm]	Bottom reflector	Reference
1DGC1	250	–	600	70	-1.6^{*2}	1539	48	Yes	[17]
1DGC2	340	–	Aperiod	200	-1.2^{*2}	1533	–	No	[18]
1DGC3	260	–	Aperiod	160	-0.9^{*2}	1565	38	No	[19]
1DGC4	250	–	Aperiod	70	-0.6^{*2}	1531	40	Yes	[8]
1DGC5	220	–	Aperiod	220	-0.9^{*2}	1535	–	Yes	[20]
1DGC6	250	–	Aperiod	250	-0.6^{*2}	1560	–	Yes	[21]
1DGCS1	250	–	660	70	-2.4^{*2}	1152	29	Yes	[22]
1DGCS2	250	–	Aperiod	70	-1.1^{*1}	1550	40	Yes	[22]
2DPDC1	220	195	605	70	-6.8^{*2}	1542	35	No	[23]
2DPDC2	220	185	635	120	-3.2^{*1}	1550	40	No	[24]
2DPDC3	400	167	584	291	-1.9^{*1}	1550	38	Yes	[25]
2DPDC4	160	209	696	80	-1.0^{*1}	1550	42	Yes	[25]
2DPDC5	220	Ellipses	487	70	-2.4^{*2}	1310	29	Yes	[26]
2DGCS1	220	150	580	90	-6.9^{*2}	1550	25	No	[27]
2DGCS2	220	75	650	150	-5.8^{*2}	1540	35	No	[28]
2DGCS4	220	–	Aperiod	$70 + 220$	-2.6^{*2}	1544	–	No	[30]
2DGCS3	220	173	635	–	-1.8^{*2}	1550	32	Yes	[29]

^{*1} Simulated, ^{*2} Measured

2.4 Two-dimensional orthogonal grating couplers

In this chapter, the work is focused on the design of 2DGCSs with the holes forming an orthogonal lattice. Two different approaches regarding the shape of the holes are realized. Firstly, the designs are based on cylindrical holes. Afterwards, the coupling efficiency of the structure with cuboidal holes is presented. Finally, this structure is optimized by means of an automatized simulation mechanism to achieve a higher coupling efficiency using a genetic algorithm. The resulting structure is an aperiodic grating coupler.

2.4.1 Cylindrical holes

The structure is designed to work at a wavelength of $\lambda = 1.55\,\mu m$. A scheme of the structure and the position of the optical fiber is shown in Figure 2.7(a). The first design is realized for a BOX (SiO_2) layer thickness of 1 µm between the Si substrate and a 250 nm thick top silicon layer. The etched depth of the holes in the top Si is 70 nm. The structure is passivated with a 1 µm thick SiO_2 layer on top. The simulations are realized with an optical fiber tilted an angle $\alpha = 10\,^\circ$ with respect to the substrate surface normal. Besides, the fiber is rotated at an angle $\psi = 45\,^\circ$ around the y-axis. The minimum distance from the fiber to the grating is 1 µm.

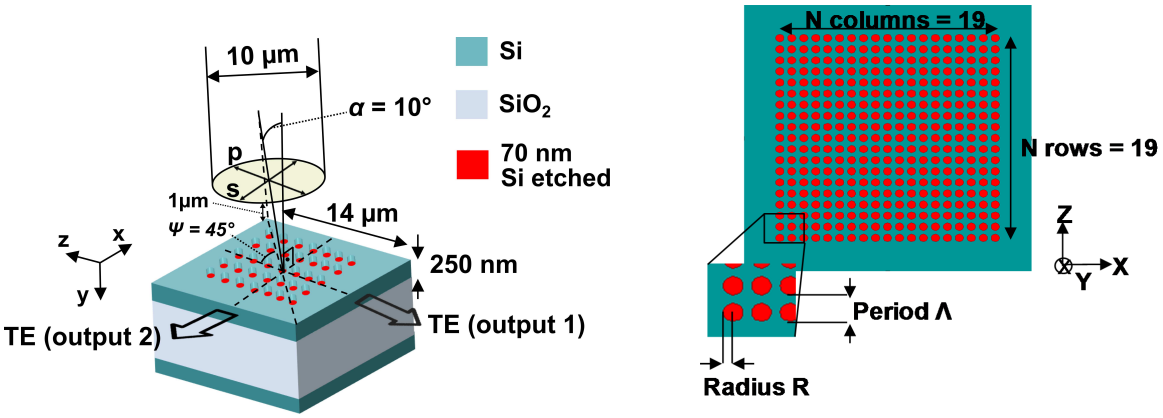

(a) (b)

Figure 2.7: (a) Scheme of the 2D grating coupler. (b) Top view of the grating structure.

In Figure 2.7(b), the top view of the grating is depicted. The number of holes is $N \cdot N$, being $N = 19$ to obtain a grating dimension similar than the optical fiber diameter. Later, the number of holes N is varied adjusting slightly the grating dimension to study its influence on the device performance.

The impact on the coupling efficiency of the grating period Λ and the radius of the etched holes R is investigated. For this purpose the 2DGCS is simulated with the 3D-FDTD method of the RSoft Photonic Device Tool, FullWAVE. The coupling efficiency is analyzed for the TE and TM polarizations, represented in Figure 2.7(a) as the s- and p-polarizations of the fiber, respectively.

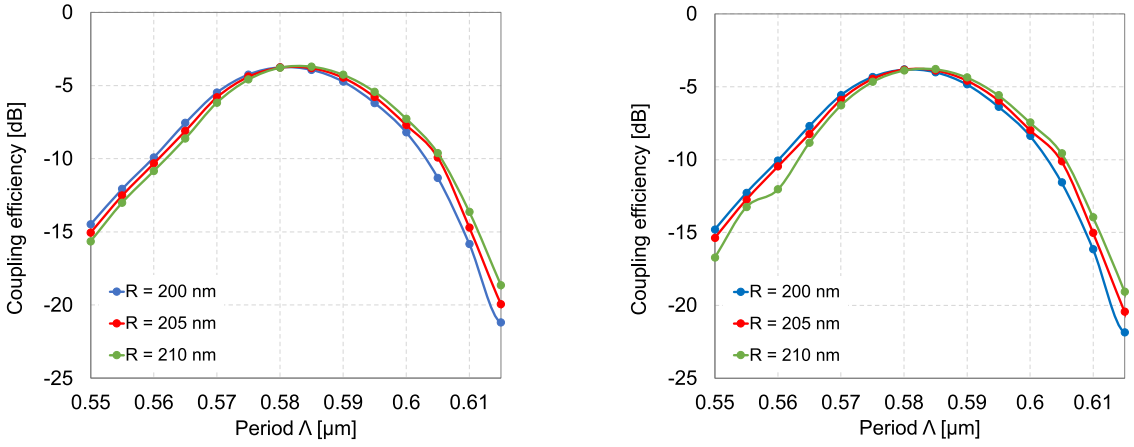

Figure 2.8: Simulation of the coupling efficiency depending on the etched hole radius R and the grating period Λ for (a) TE and (b) TM polarizations.

The coupler is simulated with different grating periods Λ between 550 nm and 615 nm with a 5 nm step for hole radii R between 175 nm and 215 nm with a step of 10 nm. The best results of the coupling efficiency are obtained for the radii $R = 200\,\text{nm}$, $R = 205\,\text{nm}$ and $R = 210\,\text{nm}$. The simulation results of these structures are plotted in Figure 2.8. It can be observed that the transmission is higher for a grating period Λ between 575 nm and 590 nm with similar results for the three plotted radii.

In the following, the basic grating dimensions used are $R = 200\,\text{nm}$ and $\Lambda = 580\,\text{nm}$, since the transmission is maximized for these dimensions. For both polarizations the coupling efficiency is around $-3.8\,\text{dB}$ at $\lambda = 1.55\,\mu\text{m}$. The electric field distribution of this GC for TE and TM is illustrated in Figure 2.9. This shows how the polarizations are split into orthogonal directions. For the TE polarization, the field propagates towards the negative z-axis and for the TM polarization it propagates towards the negative x-axis.

The optical transmitted power of this design is very similar for both polarizations. This almost symmetrical performance of the 2DGCS is a desirable feature for practical applications where the polarization independent operation of the photonic circuit is required. The coupling efficiency is extremely affected by the BOX thickness. The light coming from

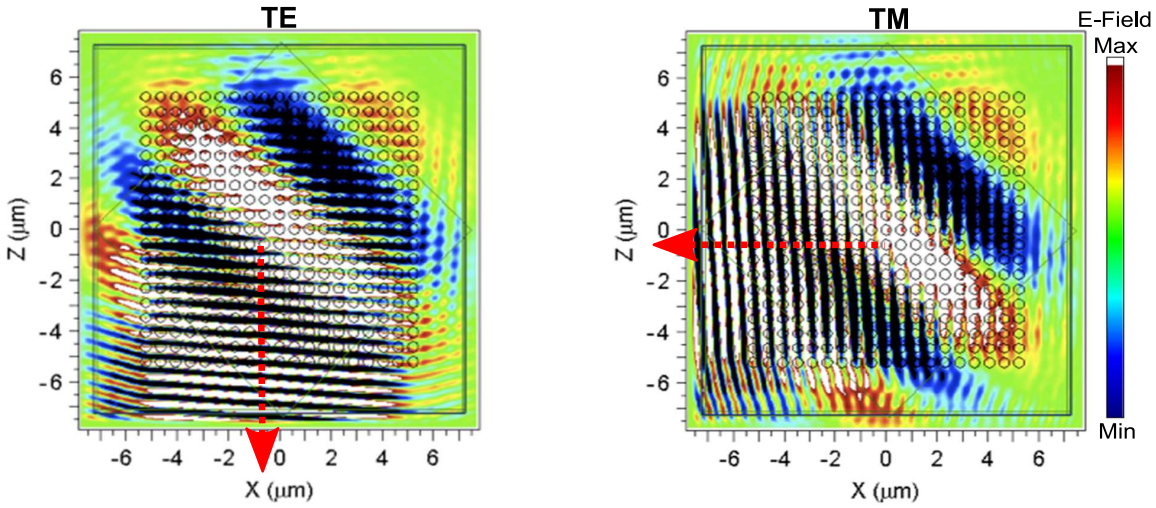

(a) (b)

Figure 2.9: Simulated electric field distribution of the 2DGCS for (a) TE and (b) TM polarizations with $R = 200\,\text{nm}$ and $\Lambda = 580\,\text{nm}$.

the optical fiber is diffracted because of the grating structure, however a high amount of light is lost to the substrate. A part of this light is reflected back to the grating due to the different refractive index of the two materials, SiO_2 (BOX) and Si (substrate). Therefore, the BOX thickness contributes to the coupling efficiency of the structure if the reflected light interferes constructively with the transmitted light. The coupling efficiency of the previously described 2DGCS is simulated for different BOX thicknesses for the two orthogonal polarizations. The simulation results are presented in Figure 2.10. The coupling efficiency is maximal for a BOX thickness of around 3 µm and it has a periodicity of around 0.5 µm. That means that the chosen SOITEC wafer, with 3 µm BOX thickness, is optimal to achieve a high coupling of the light into the waveguide.

Based on the reflection effect described before, a metal layer is added at the bottom of the BOX layer instead of the silicon substrate. The metal layer works as a perfect light reflector (mirror), avoiding light losses into the substrate. As a result of this modification the coupling efficiency at $\lambda = 1.55\,\mu\text{m}$ is enhanced reaching $-1.9\,\text{dB}$ and $-2.0\,\text{dB}$ for the TE and TM polarizations, respectively.

The number of holes $N \cdot N$ is changed in order to maximize the overlap between the electric field profile of the fundamental mode of the fiber and the grating along the lateral and longitudinal directions for both polarizations [8]. It is observed that if the number of holes is increased, the coupling efficiency can be improved, but the bandwidth is slightly reduced. The number of holes of the structure is increased to $N = 23$, since for a longer

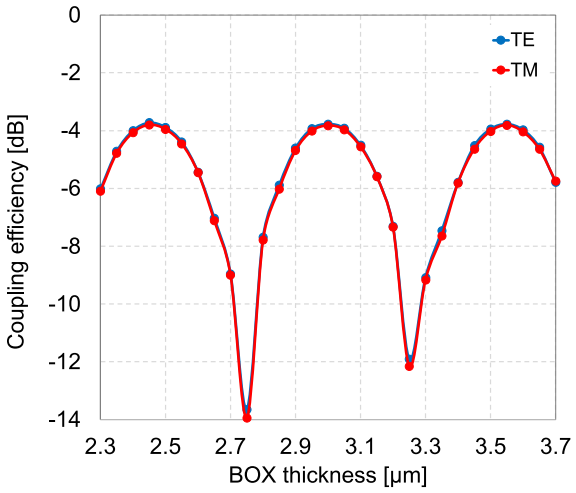

Figure 2.10: Coupling efficiency of the 2DGCS depending on the SiO_2 thickness for TE and TM. Grating dimensions are $R = 200\,\text{nm}$ and $\Lambda = 580\,\text{nm}$.

grating length the coupling efficiency starts to saturate. In addition, it is a good compromise between coupling efficiency and BW. In Figure 2.11, the transmission spectrum of the 2DGCS with $N = 19$ and $N = 23$ is shown. The results are summarized for the target wavelength $\lambda = 1.55\,\mu\text{m}$ in Table 2.2. The 1 dB-bandwidth and the 3 dB-bandwidth is defined as the width of the wavelength range where the optical transmission is reduced by 1 dB or 3 dB, respectively, with respect to the maximum transmission of the grating.

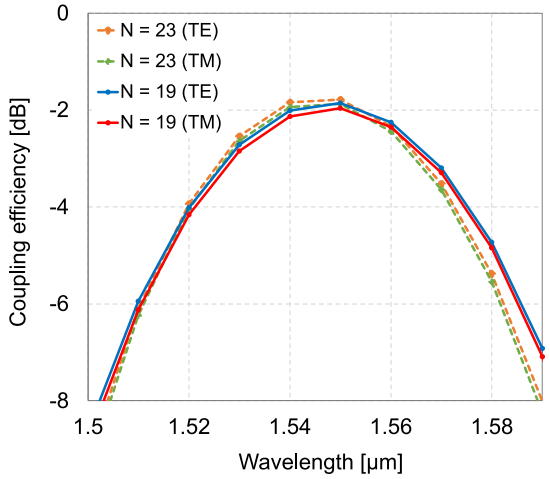

Figure 2.11: Comparison of the transmission spectrum for $N = 19$ and $N = 23$ of the 2DGCS for TE and TM polarizations. $R = 200\,\text{nm}$, $\Lambda = 580\,\text{nm}$ and with bottom metal mirror.

Table 2.2: Coupling efficiency at $\lambda = 1.55\,\mu m$ and BW of the 2DGCS with bottom metal mirror.

	$N = 19$		$N = 23$	
Polarization	TE	TM	TE	TM
Coupling efficiency [dB]	−1.9	−2.0	−1.8	−1.9
1 dB-Bandwidth [nm]	38	38	36	36
3 dB-Bandwidth [nm]	66	65.5	62	61

2.4.2 Cuboidal holes

A new periodic structure is designed with cuboidal holes instead of cylinders. The layout and description of the most important parameters are shown in Figure 2.12. This grating is based on the design described previously in chapter 2.4.1. The grating period is $\Lambda = 580\,nm$ and the holes are etched 70 nm in the Si. The holes have an edge length $a = 400\,nm$ (based on the dimensions of the cylinder radius). The use of cuboids introduce a new parameter, the rotation angle of the cuboids θ. This parameter needs to be optimized in order to achieve the best grating design for a maximum coupling efficiency.

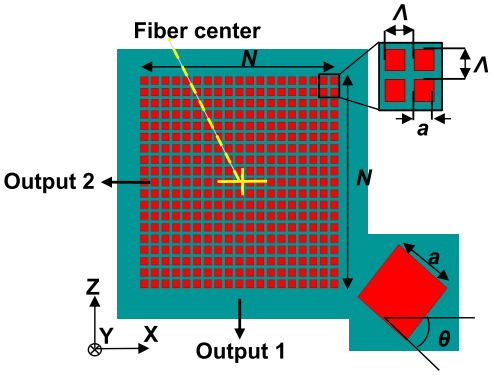

Figure 2.12: Top view of the grating structure with cuboidal holes.

In Figure 2.13, the simulation results of the coupling efficiency depending on the angle θ are plotted for the corresponding outputs 1 and 2. The TE and TM polarization signals coming from the fiber are transmitted to the output 1 and 2, respectively, as TE mode. The light power coupled into the other outputs is neglectable, i.e $< -20\,dB$.
The optical fiber is slightly shifted from the center of the grating to observe the influence of the positioning of the fiber on the coupling efficiency. If the center of the fiber is shifted from the center of the cuboid in the middle of the GC, the performance of the 2DGCS is

not identical for both orthogonal polarizations. Since for the orthogonal polarizations it is not a symmetric structure. Therefore, depending on the rotation angle θ of the cuboids, the coupling efficiency for TE and TM varies. For the angles $\theta = 20\,^\circ$ and $\theta = 30\,^\circ$ similar coupling efficiency for the two polarizations are observed. However, the differences are larger for the other rotation angles.

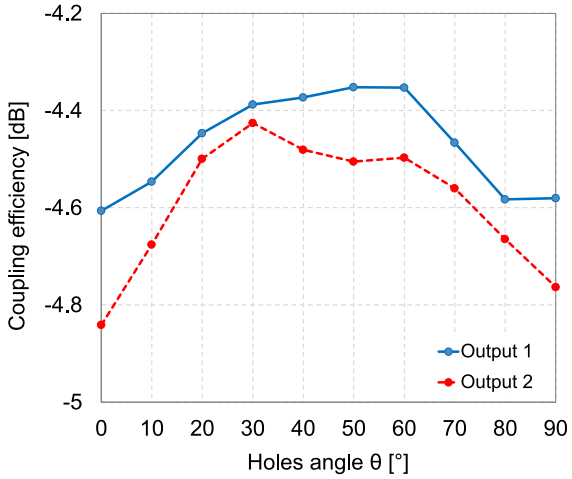

Figure 2.13: Simulated optical transmission of the fiber s-polarization (TE) at output 1 and p-polarization (TM) at output 2 of the coupler for different rotation angles of the cuboidal holes θ.

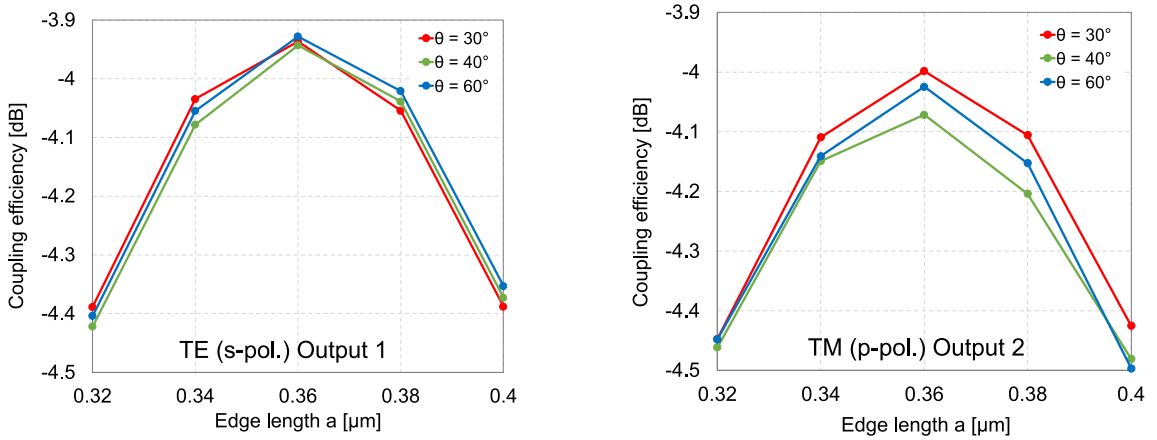

(a) (b)

Figure 2.14: Simulated coupling efficiency versus edge length a for different rotation angles θ. (a) TE and (b) TM. With $\lambda = 1.55\,\mu\text{m}$, $\Lambda = 580\,\text{nm}$, $N = 19$ and without bottom mirror.

The edge length a of the squares is studied for three different rotation angles: $30\,^\circ$, $40\,^\circ$

and 60 °. In Figure 2.14, the results show that the optimal dimensions, taking into account the two polarizations, are $\theta = 30\,^\circ$ with $a = 360\,\text{nm}$. This structure is simulated adding a metal bottom mirror under the BOX for a hole matrix of $N \cdot N = 23 \cdot 23$. The coupling efficiency achieved is $-1.9\,\text{dB}$ for TE (output 1) and $-2.1\,\text{dB}$ for TM (output 2). The 1 dB-bandwidth is 35 nm for both polarizations. The 3 dB-bandwidth is 61 nm for TE and 60 nm for TM.
The grating structure with cuboids shows only a slightly lower coupling efficiency than the one with cylinders, $-0.1\,\text{dB}$ for TE and $-0.2\,\text{dB}$ for TM. As it has been demonstrated in studies with 1DGC [8], the coupling can be enhanced if the periodic grating is modified. The aim is matching the electric field profile of the fundamental mode of the fiber, Gaussian distribution, with the field profile of the grating. This can be done by adjusting the dimensions of the grating grooves and ribs. The same principle can be assumed for the 2D gratings. In order to achieve this field profile, an aperiodic 2D structure is designed. For this purpose, the cuboids allow a simpler way of building aperiodic structures than with cylinders. In the next chapter 2.4.2.1 a study of 2D aperiodic structures is described in detail.

2.4.2.1 Aperiodic 2D grating couplers

The performance of the 2DGCS described previously can be optimized if the grating is reshaped to an aperiodic structure. Parameters as the width w and the length l of the cuboids can be tuned to maximize the coupling efficiency. These parameters can be modified independently for each row and column. Since the 2D grating requires a 3D-FDTD simulation, the simulations are very time-consuming. For this reason, parameters as the rotation angle of the cuboids and the grating period are kept constant to reduce the complexity. This means, $\theta = 0\,^\circ$ and $\Lambda = 580\,\text{nm}$, where Λ is the distance between the centers of two adjacent holes. Figure 2.15(a) shows the layout of the holes. Rectangles with the same color have the same dimensions to keep the symmetry of the structure. The structure is simulated with a bottom metal mirror.
A first simulation shows the influence of a different hole size for the first 5 rows and columns on the field profile of the grating. The simulation results for the TE polarization are shown in Figure 2.15(b), where the electric field profile of the periodic grating coupler (blue line) and the aperiodic grating coupler (red line) are compared. It is observed that the modification of the first hole lines of the structure have a huge impact on the diffracted field. The simulated aperiodic grating shows that the maxima of the E-field are higher and shifted in z-direction to the middle of the grating structure matching better with the

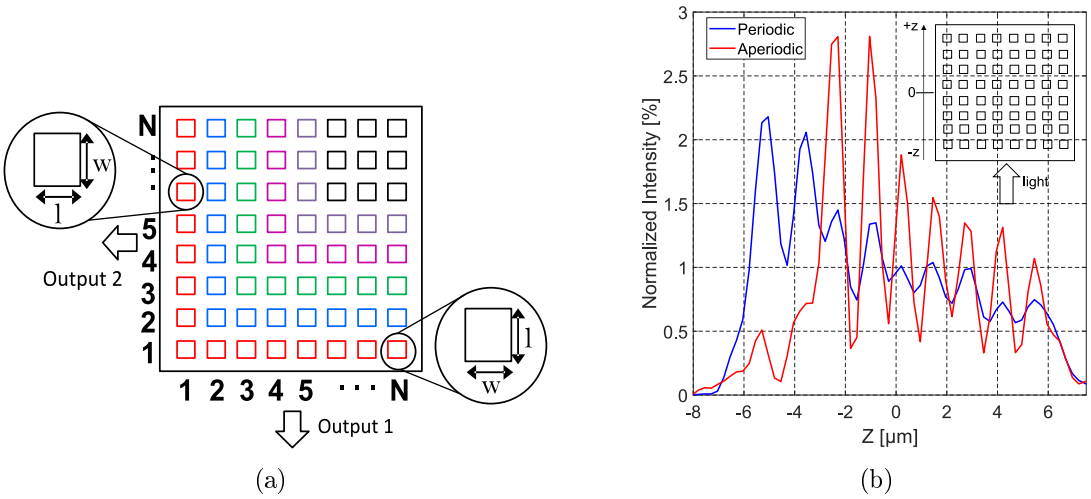

(a) (b)

Figure 2.15: (a) Scheme of the top view of the grating coupler. Holes with the same color have the same dimensions. (b) Comparison of the simulated electric field profile between the periodic and the aperiodic 2DGCS changing the first 5 hole lines.

Gaussian field profile of the optical fiber. Therefore, only the dimensions of the first five columns and rows are adjusted, since this reduces memory and time consumption of the simulations significantly.

A MATLAB script is written to automatize a huge number of simulations using a genetic algorithm [16] to modify several parameters of the grating at the same time. In order to optimize the aperiodic structure the following steps are realized by the algorithm for each iteration [31]:

1. Select independently the width w and length l of the holes for each of the first 5 lines and columns as depicted in Figure 2.15.

2. The values of the width w and the length l are selected following the criteria of the genetic algorithm. This means, 10 variables shall be optimized with the genetic algorithm.

3. 3D-FDTD simulations are realized with the chosen values to calculate the coupling efficiency of each structure.

4. The dimensions and simulation results of each grating are saved and the next iteration is started (back to step 1).

The results of this optimization process are presented in Figure 2.16. This plot shows the best coupling efficiency achieved after a specific number of iterations. It is observed that after 300 iterations, the coupling efficiency of the modified grating is better than the periodic structures presented in chapter 2.4.1 and chapter 2.4.2, which are also optimized with a metal bottom mirror. After 2000 iterations no further significant improvement is observed. The dimensions and layout of the best simulated aperiodic 2DGCS are presented in Figure 2.17(a). The coupling efficiency of this structure is $-1.7\,\mathrm{dB}$ for TE and $-1.9\,\mathrm{dB}$ for TM at $\lambda = 1.55\,\mu\mathrm{m}$. Further optimizations can be investigated if more hole lines are tuned and other parameters like the position of the holes and the rotation angle θ of the rectangular etched holes are also modified.
The transmission spectrum of the optimized grating is plotted in Figure 2.17(b). It shows a very similar coupling efficiency for the complete simulated spectrum for both polarizations. The TE polarization has a slightly better coupling efficiency and BW than the TM polarization. This small difference could be compensated by tuning the rotation angle θ of the rectangle etched holes. The 1 dB-BW is around 36 nm for TE and 33 nm for TM. The coupler exhibits a 3 dB-BW of around 63 nm for TE and 60 nm for TM.

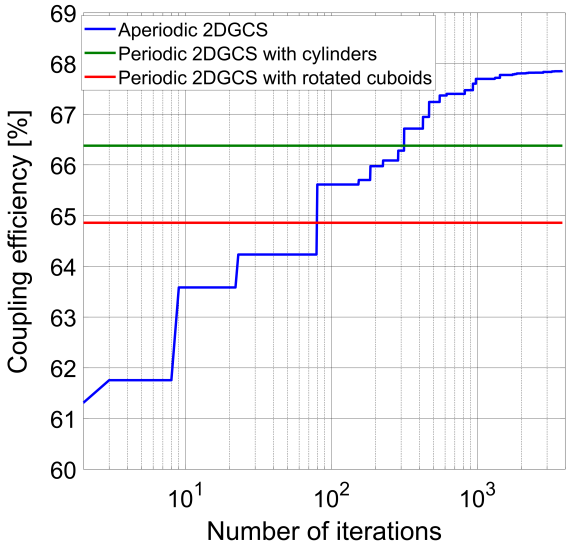

Figure 2.16: Results of the best coupling efficiency achieved vs. the number of simulations, i.e algorithm iterations, realized using a genetic algorithm.

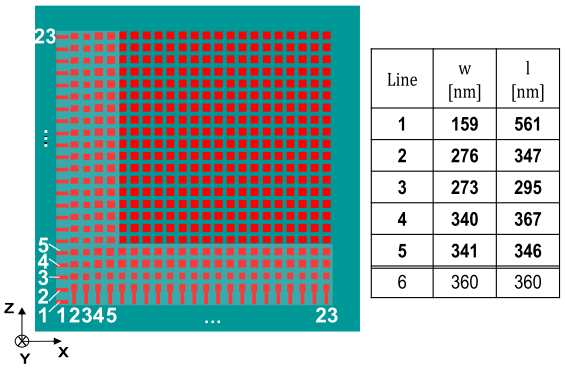

Line	w [nm]	l [nm]
1	159	561
2	276	347
3	273	295
4	340	367
5	341	346
6	360	360

(a)

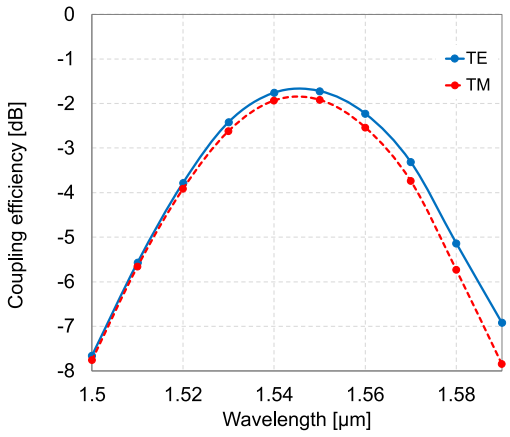

(b)

Figure 2.17: (a) Layout (top view) and dimensions of the optimized aperiodic 2DGCS. (b) Simulated optical transmission spectrum of the optimized aperiodic design.

2.5 Two-dimensional focusing grating couplers

The couplers described in chapter 2.4 have a width of around 14 µm. By means of these structures the light coming from the optical fiber is coupled into the top silicon layer with a thickness of 250 nm. If the light has to be guided through a monomode waveguide, which has a width of around 400 nm, the use of a tapered waveguide is a simple and effective solution to solve this problem. Different types of tapers working adiabatically can be used for this purpose, some examples can be found in [32]. Adiabatic tapers are realized decreasing or increasing the cross section size of a waveguide very slowly to convert the propagating first order mode of the wide waveguide to the first order mode of the narrow waveguide or vice versa. This shall be done with low loss and diminishing the mode conversion of the first order mode to radiation or higher order modes. Linear adiabatic tapers with a length of around 400 µm are fabricated and measured during this work showing a transmission loss of around 0.4 dB. However, one target of GCs is to reduce the size of the optical circuits as much as possible. Therefore, the development of grating structures with high coupling efficiency and also small size is in focus here. For this purpose, focusing grating couplers are investigated and fabricated during the thesis. The 2D focusing grating coupler (2DFGC) is basically a similar structure as the 2DGCS described in chapter 2.4, but with the additional feature of focusing the light into the waveguide at the same time. This allows that the length of the taper used to guide the light from the coupler to the waveguide can be drastically reduced. In Figure 2.18, a

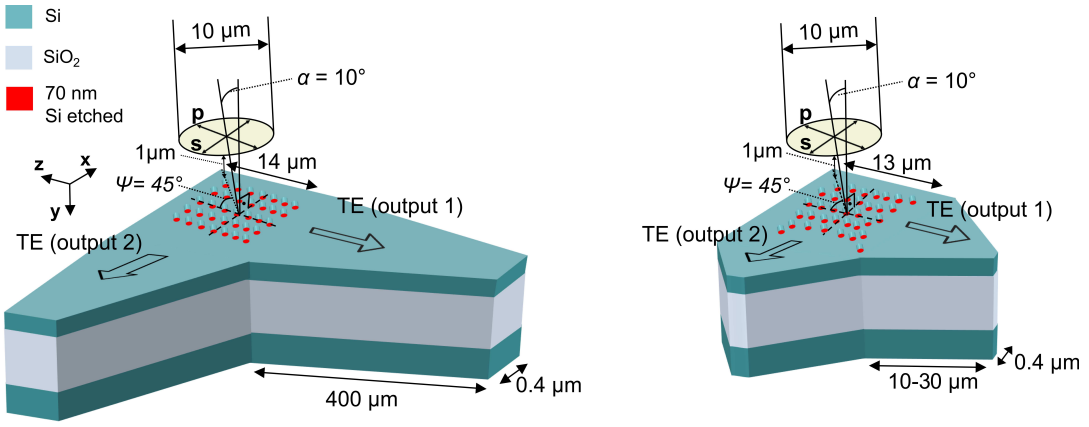

Figure 2.18: Comparison of a 2DGCS with orthogonal hole lattice (left) and a 2D focusing grating coupler (right).

comparison between the dimension of a 2DGCS with adiabatic taper and a 2DFGC with a customized taper is shown.

The holes etched in the top Si layer of the 2DFGC form a grid of $N \cdot N$. These holes are placed forming elliptical curves instead of straight lines. Nevertheless, the number of curves for each x- and z-direction is still defined as N. The exact position where the holes are etched can be described as the intersection of the orthogonal overlay of two 1D focusing grating couplers.

For the design of the focusing grating, the Bragg condition equation (Equation 2.39) has to be fulfilled.

Focusing grating lines can be defined in the xz-plane to fulfill the condition of constructive interference as

$$q\lambda_0 = zn_1 \sin\alpha - n_{\text{eff}}\sqrt{x^2 + z^2}, \tag{2.45}$$

$$\frac{\left(z + \frac{q\lambda_0 n_1 \sin\alpha}{n_{\text{eff}}^2 - n_1^2 \sin^2\alpha}\right)^2}{\left(\frac{q\lambda_0 n_{\text{eff}}}{n_{\text{eff}}^2 - n_1^2 \sin^2\alpha}\right)^2} + \frac{x^2}{\left(\frac{q\lambda_0}{\sqrt{n_{\text{eff}}^2 - n_1^2 \sin^2\alpha}}\right)^2} = 1. \tag{2.46}$$

The Equation 2.45 is a second order equation in the xz-plane. If the terms are reordered, the equation of an ellipse is obtained (Equation 2.46). Therefore, the curves representing the position of the holes are ellipses with a common focal point [33]. In Figure 2.19(a), these curves are plotted. The parameter which defines the different cofocal ellipses is the number of the grating line q. If q is changed, the size and position of the ellipses are modified. The area of the 2DFGC is represented in Figure 2.19(a) as a green square

centered in the coordinates $(0, 0)$. The offset in the x- and z-direction determines the position of the center of the coupler. The curves inside of this area are the only ones considered in the design. The final 2DFGC is built as the superposition of the same curves but rotated at an angle of 90 °. At the intersection of these curves holes are etched. An example of one of the structures designed is shown in Figure 2.19(b).

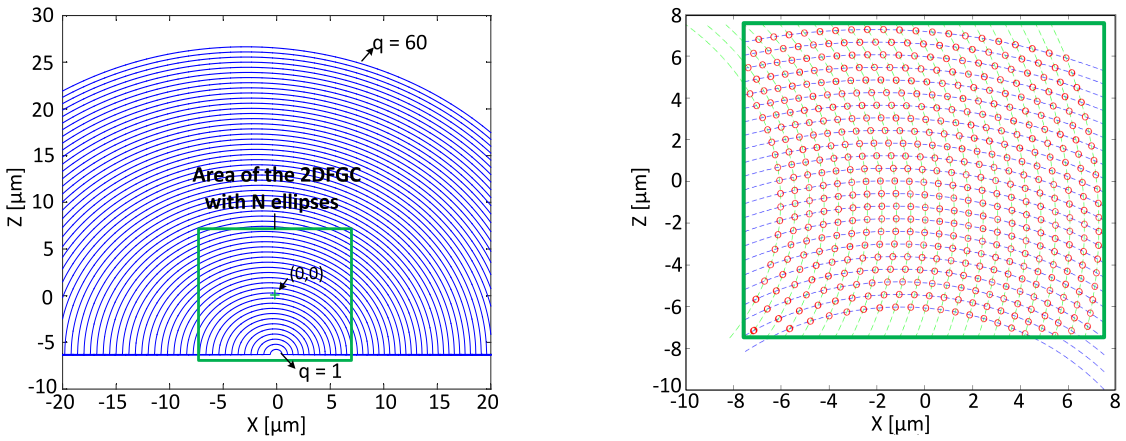

(a) (b)

Figure 2.19: (a) Ellipses with different values of q and a common focal point according to Equation 2.46. (b) Result of the orthogonal overlap of the ellipses calculated for the 2DFGC. The holes of the grating are etched at the intersections.

In order to optimize the 2DFGC a MATLAB script is written to calculate the position of the holes depending on the parameter q and the offset. The offset is defined as the (x,z) coordinates where the center of the square, that represents the coupler area, is placed. After the hole positions are calculated, the design is exported to FullWAVE and the 3D-FDTD simulation of the structure is executed. This algorithm is automatized to adjust the main parameters in order to maximize the coupling efficiency of the coupler. As realized with the 2DGCS in chapter 2.4, the designs are made with cylindrical and also cuboidal holes in the top Si layer.

For the design of the 2DFGC with cylindrical holes, the dependence of the coupling efficiency versus q and the radius of the holes R is investigated. The parameter q_{min} represents the minimum value of q of all the ellipses included in the coupler, i.e. inside of the green square in Figure 2.19. The number of ellipses are limited to $N \cdot N = 23 \cdot 23$. The simulations are realized for a range of R between 150 nm to 300 nm with a step of

15 nm for different $q_{\min} = 10; 20; 30; 34; 36; 50$. The optimum radius calculated for all the simulated $q_{\min}$ is $R = 255\,\text{nm}$, except for $q_{\min} = 10$, whose optimum radius is $R = 210\,\text{nm}$. Nevertheless, the coupling efficiency in this last case is much lower than for the other simulated $q_{\min}$ with $R = 255\,\text{nm}$. In Table 2.3 the best results obtained are summarized. It can be observed that the coupling efficiency for TE and TM polarizations is higher for a higher value of $q_{\min}$. It has to be taken into account that for higher values of q the light is less focused. Therefore, the taper used after the grating coupler to focus the light to the desired waveguide width has to be longer. Hence, this is a tradeoff between coupling efficiency and the size of the complete optical coupling structure.

Table 2.3: Characteristics and coupling efficiency results at $\lambda = 1.55\,\mu\text{m}$ for the simulated 2DFGCs with cylindrical holes.

Radius R [nm]	Period Λ [nm]	$q_{\min}$	N	Offset (x,z) [µm]	TE Coupling efficiency [dB]	TM Coupling efficiency [dB]
210	600	10	23	$(0, -3.5)$	-6.3	-6.7
255	610	20	23	$(0, -9.5)$	-5.6	-5.7
255	610	30	23	$(0, -15.0)$	-5.0	-5.2
255	610	34	19	$(0, -17.5)$	-5.0	-5.1
255	610	36	23	$(0, -18.5)$	-4.8	-5.0
255	610	50	23	$(0, -26.2)$	-4.5	-4.7

The 2DFGC is also designed with cuboids as holes. For this case, the dimension of the holes and the rotation angle θ are also optimized. The side of the cuboidal holes a is varied from 300 nm to 500 nm with a step of 20 nm. The results of the simulations show that the best coupling efficiency is achieved for $a = 440\,\text{nm}$. For this dimension, the rotation angle that presents a similar coupling efficiency for the two orthogonal polarizations is $\theta = 36\,^\circ$. The coupling efficiency and the design parameters of the structures with $\theta = 0\,^\circ$ and $\theta = 36\,^\circ$ are shown in Table 2.4. For $\theta = 36\,^\circ$, the coupling efficiency compared to the coupler with cylinders with the same offset, $q_{\min}$, N and Λ is 0.4 dB and 0.3 dB lower for TE and TM, respectively.

Figure 2.20 illustrates the layout of the most significant 2DFGC designs with the corresponding dimensions. In order to optimize the coupling efficiency of these designs, the simulations are repeated adding a metal mirror under the BOX layer. The results of the coupling efficiency and the 1 dB-BW of these designs are summarized and compared with

Table 2.4: Characteristics and coupling efficiency results at $\lambda = 1.55\,\mu m$ for the simulated 2DFGCs with cuboidal holes.

Hole side a [nm]	θ [°]	Period Λ [nm]	q_{min}	N	Offset (x,z) [µm]	TE Coupling efficiency [dB]	TM Coupling efficiency [dB]
440	0	610	34	19	$(0, -17.5)$	-5.5	-5.6
440	36	610	34	19	$(0, -17.5)$	-5.4	-5.4

other publications in Table 2.5.

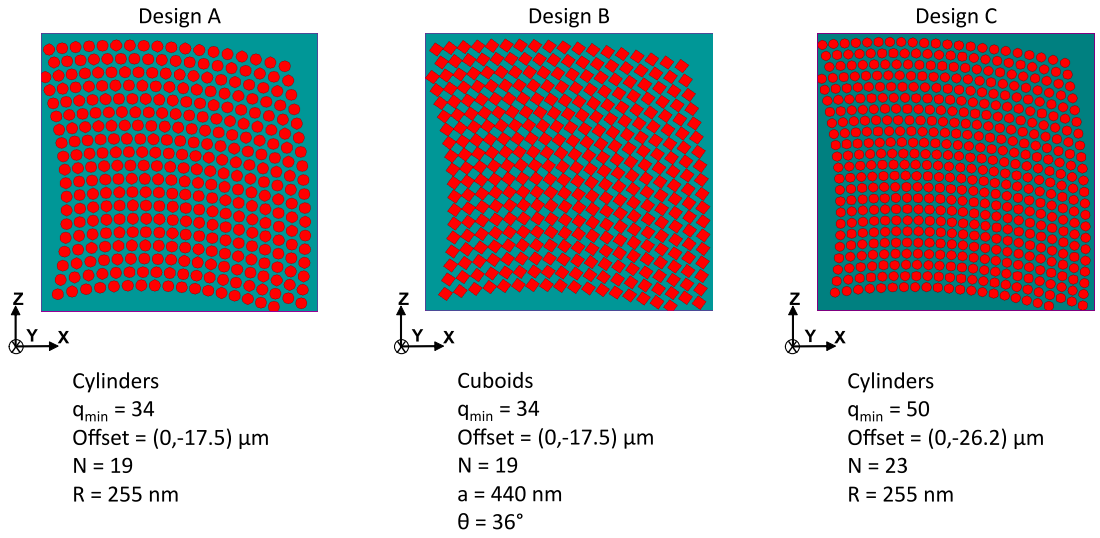

Figure 2.20: Layout of the optimized 2DFGC designs (Design A, B and C) with cuboidal and cylindrical holes and their most important parameters.

Looking into the results of the optimized 2DFGCs with metal mirror presented in Table 2.5, it can be observed that the coupling efficiency for the Design C is around 0.7 dB higher than for the Design B and 0.3 dB higher than for the Design A. However, the 1 dB-BW is higher for the design with cuboids than the designs with cylinders. The 1 dB-BW for the design with cuboids is 46 nm. The 1 dB-BW for the cylindrical hole designs are 45 nm and 40 nm for the Design A and Design C, respectively. In addition, the parameter q_{min} is higher for the Design C ($q_{min} = 50$) and as it was mentioned before, this fact has a direct influence on the focusing performance of the structure. For the designs with $q_{min} = 34$, the light is focused more acutely and the length of the taper after the grating structure can be reduced considerably. For the design with $q_{min} = 50$, the focal length is larger and therefore a longer taper is needed. Comparing the results with other

Table 2.5: Comparison of the best 2DFGC designs with the state of the art.

Hole Shape	Mirror	TE Coupling efficiency [dB]	TM Coupling efficiency [dB]	1 dB-BW [nm]	Reference
Cylinder	No	-5.7 @ $\lambda = 1520\,\text{nm}$	-5.7 @ $\lambda = 1520\,\text{nm}$	–	[34]
Customized	Yes	-2.0 @ $\lambda = 1480\,\text{nm}$	-2.0 @ $\lambda = 1480\,\text{nm}$	27	[35]
Cylinder	No	-4.4 @ $\lambda = 1548\,\text{nm}$	-4.8 @ $\lambda = 1560\,\text{nm}$	32	[36]
Cylinder	No	-5.0^*	-5.1^*	43	This work Design A
	Yes	-2.7^*	-2.9^*	45	
Cuboid	No	-5.4^*	-5.4^*	45	This work Design B
	Yes	-3.1^*	-3.2^*	46	
Cylinder	No	-4.5^*	-4.7^*	–	This work Design C
	Yes	-2.4^*	-2.5^*	40	

* at $\lambda = 1.55\,\mu\text{m}$

publications, the structures of this work show a promising performance. The results are similar compared to the best structures of other technologies at different wavelengths. The simulated coupling efficiency of the couplers of this work is given for the target telecommunication wavelength of 1.55 µm. The results show a high enhancement of the coupling efficiency by using the metal mirror without the use of complex customized hole shapes [35]. The designs presented exhibit wider 1 dB-BW than the reference publications of Table 2.5.

2.5.1 Customized tapers

The taper structures are analyzed in more detail. Simulations are realized to study the behavior of light after the output of the grating structure. The electric field profile of Design A (Figure 2.20) is presented in Figure 2.21(a) for the TE polarization. This 2DFGC has a width of 12.6 µm. In order to simulate the effect of the focusing grating, a Si waveguide with the same width as the 2DFGC is added at the outputs of the grating. The results show how the light is focused after around 17.5 µm from a width of around 12 µm

to a width of 3 µm. In addition, it can be observed that the light focus is shifted to the left side of the waveguide around 3.5 µm from the middle of the waveguide. Therefore, this is an important parameter for the accurate design of the taper and the precise positioning of a waveguide to avoid high losses of the optical circuit. The light propagation is compared with one of the 2DGCS presented in chapter 2.4. It can be observed in Figure 2.21(b) that the light in this case is not focused and the transmission is only slightly shifted, around 1.5 µm from the middle of the waveguide.

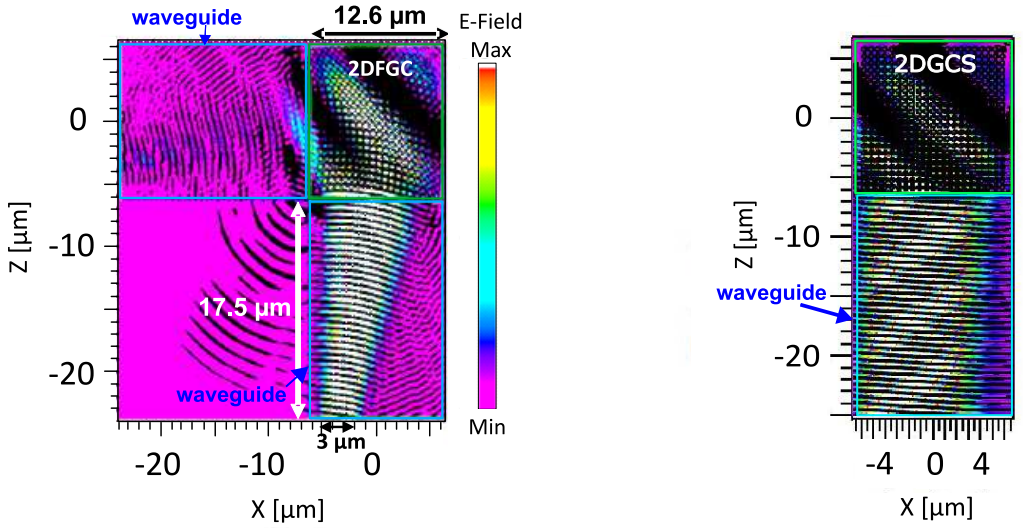

(a) (b)

Figure 2.21: Electric field profile of the (a) 2DFGC and (b) 2DGCS, both with a strip Si waveguide with the same width as the coupler.

The most significant parameters for the design of these customized tapers to couple the light efficiently and with a small footprint are described in Figure 2.22. The length of the taper b is defined as the focal length of the 2DFGC. This is the point where the light is maximally focused. The 2DFGC designs presented before are simulated again, but adding a taper at the output. The taper is used to couple the light into a monomode waveguide of 400 nm width. Therefore, the width at the end of the simulated tapers is set to this value. The taper is optimized varying the center point X of the taper output depending on the different q_{min} and the corresponding focal length, i.e. taper length b. The results are shown in Figure 2.22(right). The maximum total coupling efficiency is achieved for the design with $q_{\text{min}} = 50$, i.e. Design C in Figure 2.20. This structure shows the largest shift of the center position of the taper, $X = -4.8\,\mu\text{m}$. This is due to the

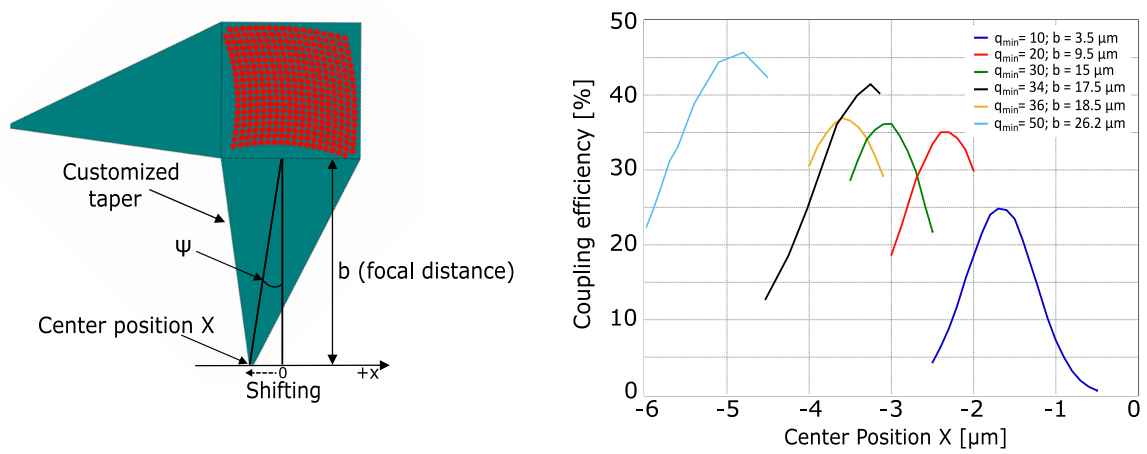

Figure 2.22: Scheme of the taper with the most significant parameters (left). Simulation results of the coupling efficiency vs. the center position X of the taper output varying the parameter $q_{\min}$ of the 2DFGC designs and the taper length b (right).

light angle ψ at the output of the grating being higher for higher parameter $q_{\min}$ of the grating. Thus, the deviation of the center position of the taper increases if $q_{\min}$ rises. For this structure, the taper length is $b = 26.2\,\mu\text{m}$. This results in a taper loss of 0.7 dB, but allows a 93% reduction of the taper length if it is compared with the regular 400 µm length linear adiabatic taper. The total coupling efficiency, including the 2DFGC and the taper, is -3.1 dB. The results for the total TE coupling efficiency of all the optimized structures are summarized in Table 2.6.

It can be observed in Figure 2.22(right) that the curve corresponding to Design A with $q_{\min} = 34$ shows a higher coupling efficiency than the ones with $_{\min} = 30$ and $q_{\min} = 36$. It has to be taken into account that Design A has a lower value of N than the rest of the designs, i.e. $N = 19$ instead of $N = 23$. Therefore, the performance of the 2DFGC is a bit different. A deeper study of the influence of the N parameter together with the taper structure, e.g. varying the width at the end of the taper, could be realized in further investigations to continue the optimization and development of the taper structures.

A first approach to reduce the customized taper losses is depicted in Figure 2.23. The new design, named Structure III, is based on the idea of utilizing the focusing performance of the 2DFGC by adding a strip waveguide with the same width as the grating and the same length as the distance where the light focusing is maximized, i.e. b. From this point is where a linear adiabatic taper is added to reduce the width of the guided light from 3 µm to 400 nm. This allows a reduction of the taper length avoiding high losses. A comparison

between the 2DGCS with adiabatic taper and the 2DFGC (Design C) with the different taper designs is presented in Figure 2.23. The results show the total coupling efficiency, i.e. the coupling efficiency of the coupler including the losses of the taper. The grating used for the structure named Structure I is the one optimized in chapter 2.4.

Table 2.6: Simulation results of the total TE coupling efficiency at $\lambda = 1.55\,\mu\text{m}$ for the 2DFGC designs with metal mirror and customized taper.

Hole Shape	R [nm]	Λ [µm]	N	$q_{\min}$	b [µm]	X [µm]	TE Coupling efficiency [dB]	Taper Loss [dB]
Cylinder	210	600	23	10	3.5	−1.7	−5.7	−10.0
Cylinder	255	610	23	20	9.5	−2.4	−4.2	−11.1
Cylinder	255	610	23	30	15.0	−3.1	−4.1	−9.0
Cylinder	255	610	19	34	17.5	−3.2	−3.6	−10.2
Cylinder	255	610	23	36	18.5	−3.6	−4.0	−8.6
Cylinder	255	610	23	50	26.2	−4.8	−3.1	−11.0

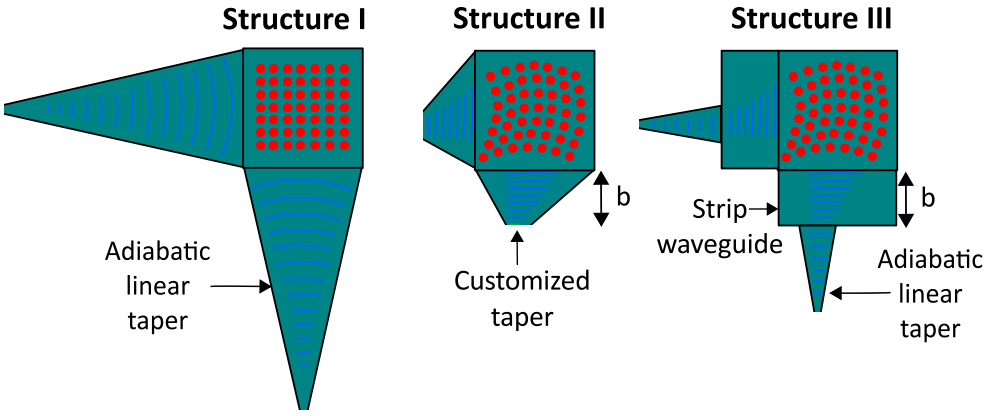

Structure	Type of grating	Type of taper	Hole shape	Taper length	TE Coupling efficiency [dB]	TM Coupling efficiency [dB]	1dB-BW [nm]
I	2DGCS	Adiabatic	Cylinders	400 µm	-1.8 (Periodic) -1.7 (Aperiodic)	-1.9	36
II	2DFGC (Design C)	Customized	Cylinders	26.2 µm	-3.1	-3.2	40
III	2DFGC (Design C)	Adiabatic	Cylinders	100 µm	-2.4	-2.5	40

Figure 2.23: Comparison of the total coupling efficiency including the taper loss, 1 dB-BW and taper length of the optimized couplers with different taper designs. The simulations are realized with a bottom metal mirror and $\lambda = 1.55\,\mu\text{m}$.

2.5.2 Measurement and optimization

Different passive Si integrated structures are fabricated using a SOI wafer at the *Institut für Mikroelektronik Stuttgart* (IMS CHIPS). The integrated optical circuit consists of a 2DFGC with a customized taper at each of the outputs of the 2D grating. Each of the ends of these tapers is connected to a monomode waveguide with 400 nm width and 30 µm length. Each monomode waveguide is followed by a standard linear adiabatic taper with a length of 400 µm. At the end of each taper an optimized aperiodic 1DGC with high coupling efficiency allows the coupling of the light from the chip into the fiber. The etched holes of the 2DFGC are cylinders with a depth of 70 nm in the top Si layer, whose thickness is 250 nm. On top, a SiO_2 passivation layer with a 1 µm thickness is deposited after etching. The radius of the holes is $R = 250\,\text{nm}$ with a period of $\Lambda = 610\,\text{nm}$ and $q_{\min} = 34$. The number of hole lines is $N \cdot N = 19 \cdot 19$. The taper of the 2DFGC has a length of $b = 19.6\,\mu\text{m}$ with a center position of $X = 3.3\,\mu\text{m}$. The layout of the fabricated 2DFGC and the customized taper is presented in Figure 2.24(a). A micrograph of the

integrated optical circuit with the 2DFGC, on the left side, connected to two 1DGC couplers, on the right side, is shown in Figure 2.24(b).

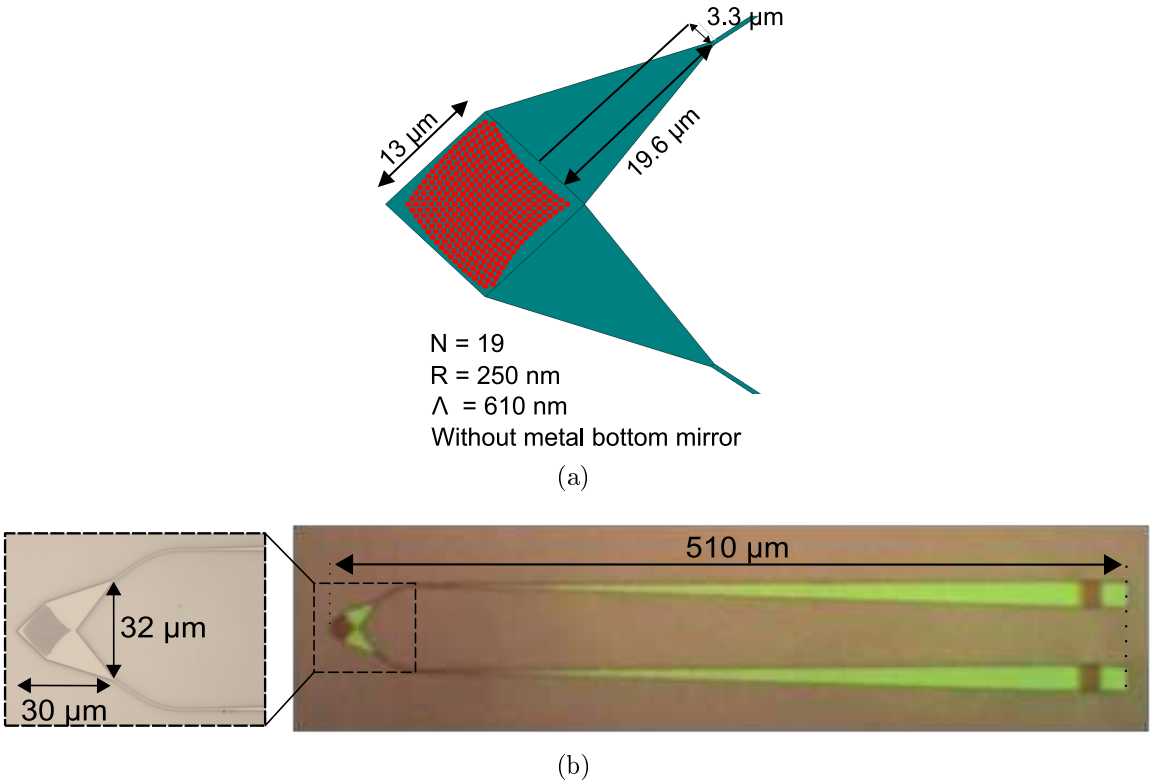

Figure 2.24: (a) Layout and (b) micrograph of the fabricated 2DFGC.

The measurement setup used for the coupling efficiency measurements of the fabricated structures is depicted in Figure 2.25. The setup consists of a tunable laser in the wavelength range between 1500 nm and 1580 nm, followed by a polarization controller. The use of a polarization controller allows the measurement of the device under test (DUT) for different polarization of the light. At the output of the polarization controller a tilted optical fiber transmits the light to the 2DFGC. The light propagates through the optical integrated waveguide and is coupled out from the chip into another tilted fiber by means of a 1DGC. Then, the light is transmitted via the optical fiber to an optical power meter, where the output light power is measured. The data of the light power provided by the tunable laser depending on the wavelength and the measured power given by the power meter at the same wavelength are collected by the computer (PC). This allows an automatized measurement of the coupling efficiency of the DUT depending on the wavelength. The coupling efficiency is a highly sensitive parameter in regard to the optical fiber position. Therefore, piezoelectric actuators are mounted in the setup to precisely adjust the

position of the fibers along the three perpendicular directions.

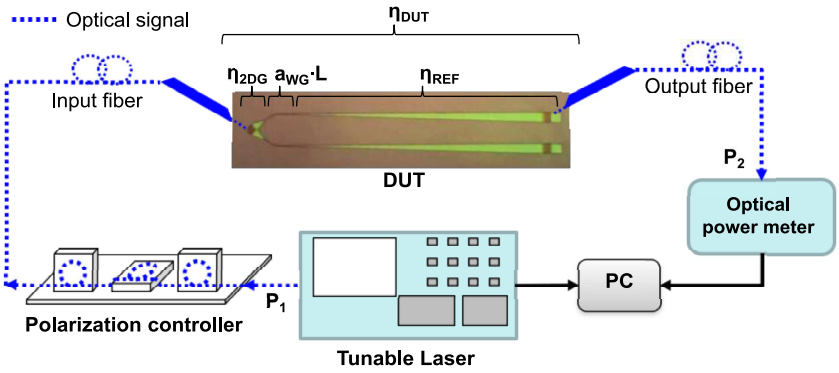

Figure 2.25: Scheme of the measurement setup used for the optical characterization of the waveguides and the GCs.

In order to determine the coupling efficiency of the fabricated coupler, the setup has to be calibrated. To determine the losses due to the polarization controller and fibers, the input fiber coming from the polarization controller is connected directly to the output fiber. The losses measured for this setup are defined as a_{setup}. The losses due to the coupling and the optical circuit on chip are calibrated by means of embedded calibration structures. For this purpose, different test structures are designed and fabricated on the same die as the 2DFGC designs. One of these test structures includes two aperiodic 1DGCs connected by a waveguide with the same width than the 1DGC. This structure allows to identify the coupling efficiency of the aperiodic 1DGC. If the calibration includes the losses due to the adiabatic taper and the monomode waveguides, the test structure used is composed by two aperiodic 1DGCs, each of them with a linear adiabatic taper. This coupler with the adiabatic taper is defined as reference coupler. The two reference couplers are connected directly or by means of a monomode waveguide with a width of 400 nm and length L. Several test structures with the same design, but only with a variation of the length L of the monomode waveguide, are measured. Thereby, the loss of the waveguide a_{WG} (in dB/µm) can be calculated. The coupling efficiency of the reference coupler η_{REF} can be expressed as follows

$$\eta_{\text{REF}} = -\frac{P_1[\text{dBm}] - P_2[\text{dBm}] - a_{\text{setup}}[\text{dB}] - a_{\text{WG}} \cdot L[\text{dB}]}{2}, \tag{2.47}$$

where P_1 and P_2 are the light power provided by the tunable laser and measured by the optical power meter, respectively. Both powers are given in dBm. The coupling efficiency of the fabricated 2DFGC circuit (DUT) defined as η_{DUT} consists of the coupling efficiency

of the 2DFGC including the customized taper η_{2DG}, the coupling efficiency of the reference coupler η_{REF} and the loss due to the waveguide $a_{WG} \cdot L$ as shown in Figure 2.25, which yields

$$\eta_{\mathrm{DUT}} = \eta_{\mathrm{2DG}}[\mathrm{dB}] + \eta_{\mathrm{REF}}[\mathrm{dB}] - a_{\mathrm{WG}} \cdot L[\mathrm{dB}]. \tag{2.48}$$

In addition, the measured η_{DUT} can also be expressed as

$$\eta_{\mathrm{DUT}} = -(P_1[\mathrm{dBm}] - P_2[\mathrm{dBm}] - a_{\mathrm{setup}}[\mathrm{dB}]). \tag{2.49}$$

Therefore, the performance of the 2DFGC with the customized taper can be isolated and characterized. The coupling efficiency is given by

$$\eta_{\mathrm{2DG}} = -(P_1[\mathrm{dBm}] - P_2[\mathrm{dBm}] - a_{\mathrm{setup}}[\mathrm{dB}] - a_{\mathrm{WG}} \cdot L[\mathrm{dB}] + \eta_{\mathrm{REF}}[\mathrm{dB}]) \tag{2.50}$$

Applying this calibration, the measurement results of the coupling efficiency of the 2DFGC with customized taper are shown in Figure 2.26. The measurements are realized with the fibers tilted at an angle of 13 ° with respect to the normal of the coupler. The results show a maximum coupling efficiency of $\eta_{\mathrm{2DG}} = -7.02\,\mathrm{dB}$ at $\lambda = 1560\,\mathrm{nm}$ for the TM polarization and $\eta_{\mathrm{2DG}} = -7.63\,\mathrm{dB}$ for TE at the same wavelength. The maximum for the TE polarization is measured at $\lambda = 1571\,\mathrm{nm}$ with a coupling efficiency of $-7.61\,\mathrm{dB}$. For both polarizations the measured curves are similar showing a 1 dB-BW of around 30 nm. Precisely, for the case of the TM polarization, the 1 dB-BW is a bit higher than 30 nm, but the coupling efficiency at larger wavelengths is not measured since the setup allows reliable measurements only up to 1580 nm.

The measurements are compared with the simulation results of the same grating design with and without customized tapers for both orthogonal polarizations. The shape of the curves are analogous to the measured ones, but an offset in the coupling efficiency can be observed. This may be caused by irregularities in the fabrication, see Appendix A, especially the critical hole dimensions. A deviation from the original design shape and dimension can drastically reduce the coupling efficiency. Another factor to be investigated in the future is the coupling efficiency of the customized taper itself: Test structures with different customized tapers can be fabricated to be able to characterize the performance of the tapers and investigate if the optical mode at the end of the tapers match perfectly with the fundamental mode of the monomode waveguide or maybe extra losses can be derived from this connection. Nevertheless, the measurement results show promising performance of the focused grating coupler with a customized taper. This design with a very small

footprint of 30 µm · 32 µm (Figure 2.24) allows the coupling of light from an optical SMF with 10 µm diameter to an embedded monomode waveguide with a width of 400 nm and a height of 250 nm.

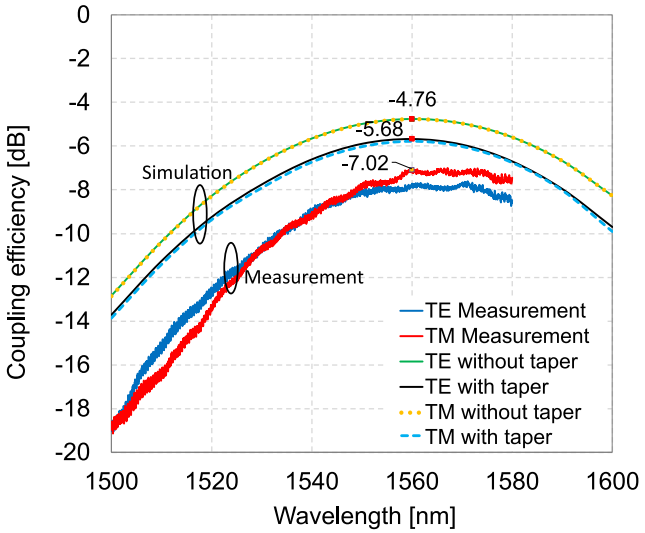

Figure 2.26: Measurement results of the fabricated 2DFGC with customized taper and comparison with the simulated structure with and without customized taper.

This structure can be optimized using a bottom metal mirror at the substrate interface with the BOX in order to avoid light losses into the substrate. In addition, the coupling efficiency can be further enhanced adjusting slightly the design parameter as the optimized Design C (Figure 2.20). The coupling efficiency depending on the wavelength is simulated for the fabricated and the optimized 2DFGC. The results are plotted in Figure 2.27. The two curves on top are the results of the optimized 2DFGC with a metal mirror. This shows the improvement of the coupling efficiency of the optimized 2DFGC with respect to the fabricated 2DFGC without metal mirror (two bottom curves). The maximum coupling efficiency of only the grating coupler, without taking into account the losses of the customized taper, is $-2.22\,\mathrm{dB}$ at $\lambda = 1560\,\mathrm{nm}$. Considering the influence of the customized taper, the efficiency is $\eta_{\mathrm{2DG}} = -2.96\,\mathrm{dB}$. The coupling performance of the fabricated 2DFGC including the customized taper could be optimized around 2.7 dB if the Design C (Structure II Figure 2.23) with a metal bottom mirror is fabricated.

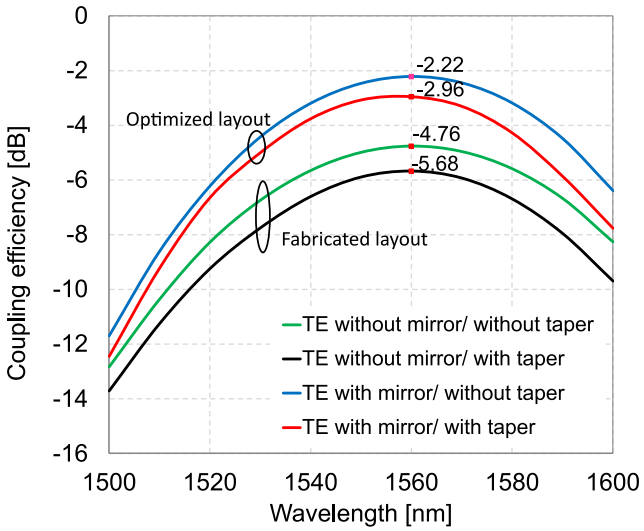

Figure 2.27: Comparison of the simulated coupling efficiency of the optimized 2DFGC with a bottom metal mirror (Design C) and the fabricated 2DFGC design without bottom mirror. Both structures are simulated with and without the customized taper.

3 Silicon optical modulator

Nowadays, the rapid increase of the communication data rates requires the use of infrastructure that maximizes the system capacity and minimizes the signal degradation. Therefore, the demand for fiber optical communication systems is drastically increasing. The optical modulator is a key element in such systems. High modulation efficiency, small size, low bias voltage, high extinction ratio, low optical loss and wide bandwidth are the figures of merit of the modulators to be optimized. Low cost is decisive for commercial systems, therefore silicon optical modulators are in focus.

3.1 Fundamentals of optical transmission systems

This chapter presents a short insight into the field of the optical transmission systems with special focus on optical modulators. The theoretical basics of the main devices, parameters and numerical methods used during the design phase of the optical modulator are described.

An optical transmission system consists of an optical transmitter, a link and a receiver. The optical transmitter and receiver transform the electrical signal into an optical signal (transmitter) or vice versa (receiver). The aim is the transmission of the information by means of an optical fiber or an integrated waveguide, i.e. an embedded optical circuit on a die.

For the design of an optical system, first it is important to know the type of the signal and the bit rate that shall be sent. For example, analog or digital, codification, optical source used, etc. These factors have a direct influence on the complexity of the transmitter and the receiver and the modulation format used. The optimal solution of the target system can diverge extremely of each other in order to fulfill the requirements of the network.

A brief overview of the components of an optical system is outlined in the following chapters. In addition, a theoretical background of the modulation formats and design concepts of the optical modulators is described with more details.

3.1.1 Optical transmitter

An optical transmitter is mainly composed of an optical source and a modulation mechanism that can be integrated in the optical source. For systems with higher modulation order, a separate optical modulator is preferred.

3.1.1.1 Optical source

Typically, light emitting diodes (LED) or laser diodes serve as optical sources in optical fiber communication systems. Depending on the target system and the requirements, the most important characteristics of the light sources shall be evaluated to select the optimal one. Some of the fundamental parameters to be considered are: power level, coherent or incoherent light, wavelength and date rate.
The distances of optical transmission span the range from millimeters to many kilometers. Hence, the power of the source has a significant importance.
Considering the type of light, it can be classified as coherent or incoherent light. Coherent light consists of one frequency with narrow bandwidth, while incoherent light contains several frequencies.
The wavelength emitted by the light source is essential for the design of the optical system. Since the materials used in the fabrication of the devices are directly related to the operating wavelength of the system. For example, at the same wavelength some materials are transparent and other materials absorb. The common wavelengths used in telecommunications are around 1310 nm and 1550 nm. The minimum of attenuation for optical fibers is reached at 1550 nm. This band is known as the third optical transmission window.
The data rate at which the transmitter can be modulated shall be also considered. Since an external optical modulator could be required in order to increase the data rate of the system.
The LED and the laser diode are used for different scenarios depending on the target. The main characteristics of these two light sources are briefly described.
The LED is a light source with spontaneous and incoherent light emission, whose structure is a forward biased semiconductor pn-junction. The emitted light spectrum is in the wavelength range between 30 nm and 60 nm, which is relatively wide. Chromatic dispersion and low directionality lead to low efficiencies and limit the use of LEDs for optical fiber communications. However, LEDs are cheap and widely available for consumers.
The laser diode is a light source with stimulated and coherent emission. The most impor-

tant elements that form a laser structure are: the active material excited by a pumping electrical source and the resonator cavity. The working principle of the laser consists of exciting the carriers of the active material applying an electrical source. Then, thanks to the stimulated emission process, the photons traveling in the resonance cavity generate more photons with the same frequency, energy and propagation direction. Therefore, the output power of the laser is generally higher than the LED. In addition, the laser diodes have a higher directionality than LEDs. This allows for a higher coupling efficiency with optical fibers and accordingly a higher efficiency of the optical system. Furthermore, the transmission of the light emitted by a laser can be realized with a single mode fiber with a single wavelength. This reduces modal dispersion.
Disadvantages of the laser in comparison to the LED include cost and sensitivity to temperature. Nevertheless, the laser is the optical source most commonly used in optical communications systems due to the compact size, high emission power and efficiency and a narrow spectrum of emission.

3.1.1.2 Optical modulator

The transmission of information in an optical system is realized modulating one or more parameters of the light commonly with an electrical signal. Some of the parameters that can be manipulated for the optical modulation are: intensity, phase, frequency and polarization.
The modulation can be realized directly in the optical source or by an external modulator. Direct modulation is done by adding the modulated electrical signal on the driving current of the optical source. This modulation is an on-off keying (OOK) or intensity modulation. However, although it is a simple and cheap method, some disadvantages shall be considered as chirp, clipping or nonlinear response.
The use of external modulators allows for simpler optical sources with constant output power. This means, the driving current of the source is constant and therefore the lifetime of the device is increased. In addition, higher modulation speed can be achieved and undesired effects as chirp are reduced. The most commonly used external optical modulators are described below.

3.1.1.2.1 Phase modulator A phase modulator can be realized with a single optical waveguide where, by means of an external electrical source, the refractive index of the waveguide material is changed. Thereby, the propagation of the light is modified. This results in a modulation of the phase of the optical signal. A scheme of a phase modulator

is depicted in Figure 3.1.

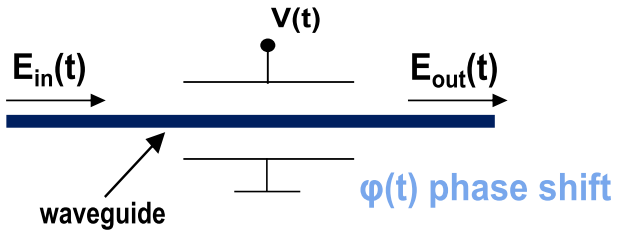

Figure 3.1: Scheme of an optical phase modulator.

The input light propagates through the waveguide and an electrical signal $V(t)$ is applied by the electrodes of the structure. This produces a phase shift of the optical signal defined as $\varphi(t)$. The transfer function of the modulator is described by the electric field as follows

$$E_{\text{out}}(t) = E_{\text{in}}(t)e^{j\varphi(t)} = E_{\text{in}}(t)e^{\frac{j\pi V(t)}{V_\pi}}, \tag{3.1}$$

where V_π is the voltage needed to achieve a phase shift of the optical wave of π.
A key parameter to describe the light propagation depending on the material is the refractive index $\underline{n}$:

$$\underline{n} = n - j\kappa = \sqrt{\underline{\epsilon}}, \tag{3.2}$$

where κ is the extinction coefficient that describes the absorption of the medium and n is the real part of the refractive index. The refractive index can be also expressed as the square root of the complex dielectric constant $\underline{\epsilon}$.
Assuming that the light is a plane electromagnetic wave traveling in z-direction, the wave number for lossy materials is defined as

$$\underline{k_z} = \beta - j\frac{\alpha}{2}, \tag{3.3}$$

where β is the phase coefficient and α is the intensity absorption coefficient. The electric field is given by [2]

$$\underline{E}(x,y,z,t) = \underline{E}_{\text{x}}e^{j(wt-\underline{k_z}z)} = \underline{E}_{\text{x}}e^{-j\beta z}e^{-\frac{\alpha}{2}z}e^{jwt}. \tag{3.4}$$

The phase coefficient of the wave is then

$$\beta = \frac{2\pi n}{\lambda} \tag{3.5}$$

and the absorption coefficient is

$$\alpha = \frac{4\pi\kappa}{\lambda}, \tag{3.6}$$

where λ is the light wavelength.

Optical modulators use the change of the absorption coefficient for intensity modulation or the change of the refractive index for phase modulation. Frequency or polarization modulation are techniques much more complex that require for both, transmitter and receiver, more challenging designs.

Different techniques can be used to change the refractive index. The Pockels effect and the Kerr effect vary the dielectric constant ϵ of the material when an electric field is applied. In the case of the Pockels effect, the variation is linear to the electric field ($\Delta\epsilon \propto E$) and in the case of the Kerr effect, the variation is proportional to the quadratic of the electric field ($\Delta\epsilon \propto E^2$). However, these two electro-optic effects are very weak in silicon.

With the Franz-Keldysh effect and the Stark effect a change in the optical absorption of the semiconductor material is caused by means of the electric field applied [37]. These effects are often used for intensity modulation. For example, germanium is a semiconductor material which can absorb the light at the telecommunication wavelength 1.55 µm.

The thermo-optic effect and the acousto-optic effect also modify the refractive index. However, they are not optimal for silicon optical modulators, since the response is weak and slow for high frequencies.

Special focus is given for the plasma dispersion effect. This method, used to change the refractive index of the semiconductor, has a suitable relevance in silicon optical modulators. It has a strong and fast response in Si, so high frequency modulation can be achieved.

The change of the refractive index, both the real and the imaginary part, by the variation of the carrier concentration is described with the Soref and Bennett formulas for Si at $\lambda = 1.55\,\mu\text{m}$ [38]. These are given by

$$\Delta n = -[8.8 \cdot 10^{-22} \cdot \Delta N_\text{d} + 8.5 \cdot 10^{-18} \cdot (\Delta N_\text{a})^{0.8}], \tag{3.7}$$

$$\Delta\alpha = 8.5 \cdot 10^{-18} \cdot \Delta N_\text{d} + 6 \cdot 10^{-18} \cdot \Delta N_\text{a}, \tag{3.8}$$

where Δn is the change of the refractive index (real part) and $\Delta\alpha$ is the change of the absorption coefficient (imaginary part of the refractive index). The change of the electron (donor) and hole (acceptor) carrier concentration are ΔN_d and ΔN_a, respectively.

The plasma dispersion effect can be realized with different techniques. Depending on

the bias voltage, carrier movement and doping profile, i.e. architecture of the doped waveguide, three different concepts can be implemented in silicon: carrier injection, carrier accumulation and carrier depletion.

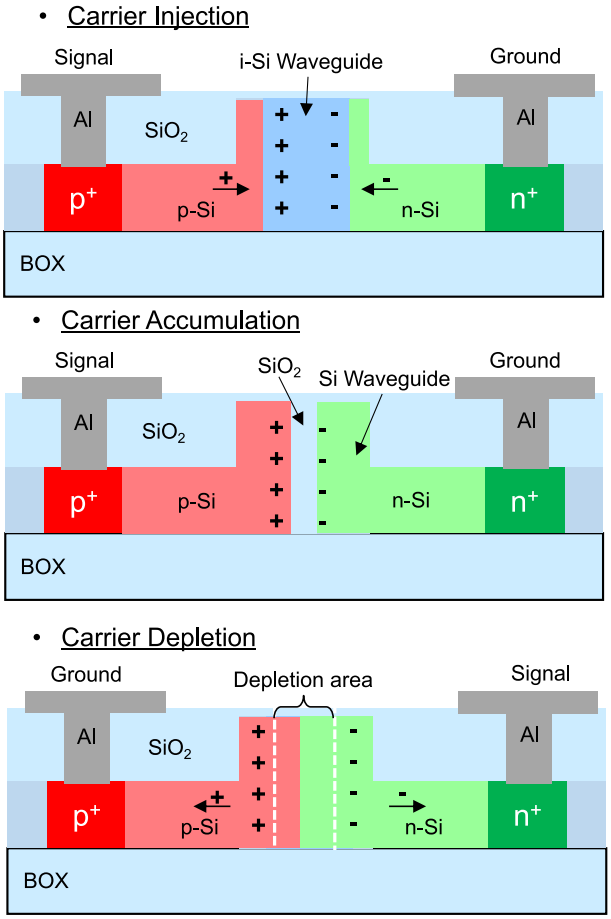

Figure 3.2: Scheme of the plasma dispersion effects on a Si waveguide. From top to bottom: Carrier injection, carrier accumulation and carrier depletion.

The cross section of a rib doped silicon waveguide is shown in Figure 3.2. The waveguide is voltage biased by an external electrical signal by means of metal contacts connected to the highly doped silicon regions, i.e. p^+- and n^+-regions, of the waveguide.
The first diagram describes the carrier injection technique. The core of the waveguide is undoped. This is depicted as intrinsic Silicon (i-Si). At both sides of the i-Si, the silicon is doped with positive and negative carriers, i.e. p- and n-regions. The waveguide is forward biased and when a positive voltage is applied to the structure, the carriers move from the doped silicon regions to the middle of the waveguide. Hence, the carrier density is changed in this region and the properties of the medium are modified. As a result, a variation on the refractive effective index n_{eff} is obtained and the phase of the optical wave

can be modulated. When the carriers move to the i-Si region, the carrier recombination takes place. This has an impact on the radio frequency (RF) response of the device, since it depends on the carrier lifetime.

The second diagram represents the carrier accumulation method. The core of the waveguide is isolated in the middle with a thin region of SiO_2 forming a slot waveguide. The waveguide is forward biased. The carriers move to the edge of the doped waveguide that is in contact with the isolated region. The positive and negative carriers cannot recombine, due to the isolated region. Therefore, the carriers are accumulated at the edges and the carrier concentration increases. Thus, the phase modulation of the optical wave traveling through the waveguide is carried out. This method requires more effort in the fabrication process, since the isolation region has to be very thin to avoid extra losses of the fundamental mode of the optical wave. Because, the E-field distribution of the fundamental mode presents the maximum in the middle of the monomode rib waveguide. In addition, the carrier accumulation causes higher attenuation of the optical wave due to undesired absorption. The slot doped waveguide can be considered as a capacitance which increases with reduced slot width. This is one of the main factors that limits the RF response of this device, since the modulation bandwidth of the modulator is mainly determined by its RC-time constant τ_{RC} as $f_{3\mathrm{dB}} = 1/(2\pi\tau_{\mathrm{RC}})$. The value of τ_{RC} for a modulator of a given resistance increases with the capacitance, thereby the bandwidth of the device decreases.

The third diagram shows the carrier-depletion effect. The silicon waveguide is completely doped and it is driven with reverse bias voltage. When the reverse voltage is applied to the electrodes, the carriers move to the contact zones and thereby a depletion area is generated in the pn-junction region. The width of the depletion area depends on the relative dielectric constant ϵ_{r} of the material, the carrier concentrations N_{a} and N_{d}, and the difference of the applied voltage $(V_{\mathrm{bi}} - V_{\mathrm{bias}})$ where V_{bi} is the built-in potential voltage and V_{bias} is the applied bias voltage [39]. The depletion width is defined as

$$w_{\mathrm{dep}} = \sqrt{\frac{2\epsilon_0\epsilon_{\mathrm{r}}(N_{\mathrm{a}} + N_{\mathrm{d}})(V_{\mathrm{bi}} - V_{\mathrm{bias}})}{qN_{\mathrm{a}}N_{\mathrm{d}}}}. \tag{3.9}$$

The high frequency performance of the diode is based on the carrier dynamic and the RC-time constant of the diode.

3.1.1.2.2 Mach-Zehnder modulator (MZM) Mach-Zehnder modulators are based on the same interference principle as the Mach-Zehnder interferometer (MZI). The light transmitted trough a waveguide is split in two waveguide branches. Either one or two

branches can work as a phase modulator. An electrical modulated signal changes the refractive index and thus the phase at the end of the branch. Afterwards, the two waveguide branches are combined again into one waveguide. Therefore, if the MZM is symmetrical and no electrical signal is applied, a constructive interference is produced. Thus, the output signal is the original one at the input of the interferometer assuming no losses. If a phase modulation is realized in one of the branches with a phase shift of $\varphi = \pi$, a destructive interference of the two optical waveguides occurs at the output and the optical power is lost into the substrate. Thereby, an intensity modulation is obtained by means of the phase modulation of one of the branches of the interferometer. In fact, the example with phase shifting of $\varphi = \pi$ produces an OOK modulation. This structure can be improved if the phase modulation is realized in both of the branches. The phase shift can be done efficiently, so the length of the branches can be reduced and therefore the size of the MZM and the chirp [40] can be reduced. A scheme of an MZM with a phase modulator in one of the branches is illustrated in Figure 3.3(a) and with phase modulators in both branches in Figure 3.3(b).

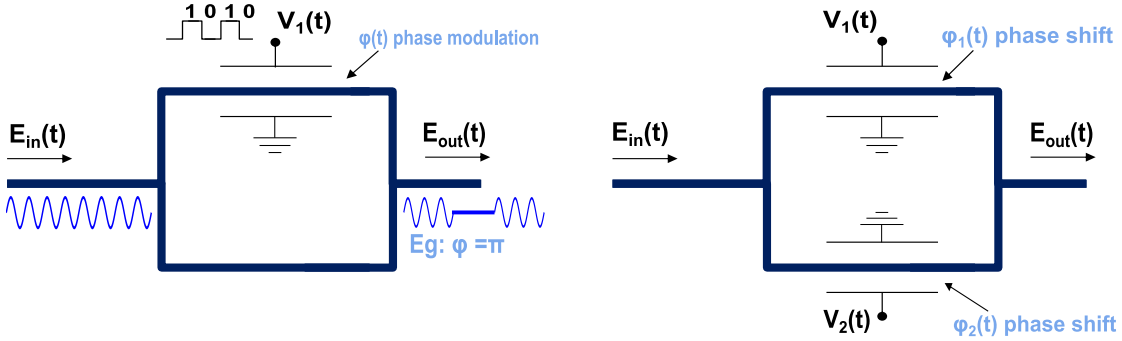

Figure 3.3: (a) Asymmetric MZM. A phase modulation of $\varphi = \pi$ is shown for an OOK modulation at the output of the MZM. (b) Symmetric MZM with arbitrary driving voltages.

Considering that the optical field is not symmetrically split between the two arms of the MZM and in addition the electrodes of both arms are driven by different voltages, the electric field at the output can be described as

$$E_{\text{out}}(t) = \frac{E_{\text{in}}(t)}{2}\left[(1+k)e^{\frac{j\pi V_1(t)}{V_\pi}} + (1-k)e^{\frac{j\pi V_2(t)}{V_\pi}}\right], \tag{3.10}$$

where k is the imbalance factor of the optical field split in the two arms. The extinction ratio (ER), i.e. the ratio between the maximum and minimum optical transmission

of the device, is inversely proportional to the k factor. Symmetrical MZMs, where the electrodes can be driven with same voltages, allow the optimization of the ER. These devices are called push-push MZMs, which produce pure phase modulation. If the electrodes are driven with opposite voltages, it is called push-pull MZM, which yields intensity modulation.

The Equation 3.10 can be simplified assuming a symmetric structure and opposite driving voltages $V_2(t) = -V_1(t) = V(t)/2$ of both branches of the MZM, i.e push-pull operation. Hence, the output electric field of the device is given by

$$E_{\text{out}} = \frac{E_{\text{in}}(t)}{2}\left(e^{\frac{j\pi V_1(t)}{V_\pi}} + e^{\frac{-j\pi V_1(t)}{V_\pi}}\right) = E_{\text{in}}(t)\cos\left(\frac{\pi V(t)}{2V_\pi}\right). \tag{3.11}$$

The transfer function that describes the intensity modulation driven by a time dependent voltage $V(t)$ is

$$I_{\text{out}}(t) = T\frac{I_{\text{in}}(t)}{2}\left[1 + \cos\left(\frac{\pi V(t)}{V_\pi} - \varphi_0\right)\right], \tag{3.12}$$

where $I_{\text{in}}(t)$ and $I_{\text{out}}(t)$ are the input and the output optical intensity, respectively. The optical transmission of the modulator is defined as T. The initial phase difference is zero if both arms of the modulator have the same optical paths. If there is a difference between them, this is defined as φ_0 and shall be considered in the calculations.

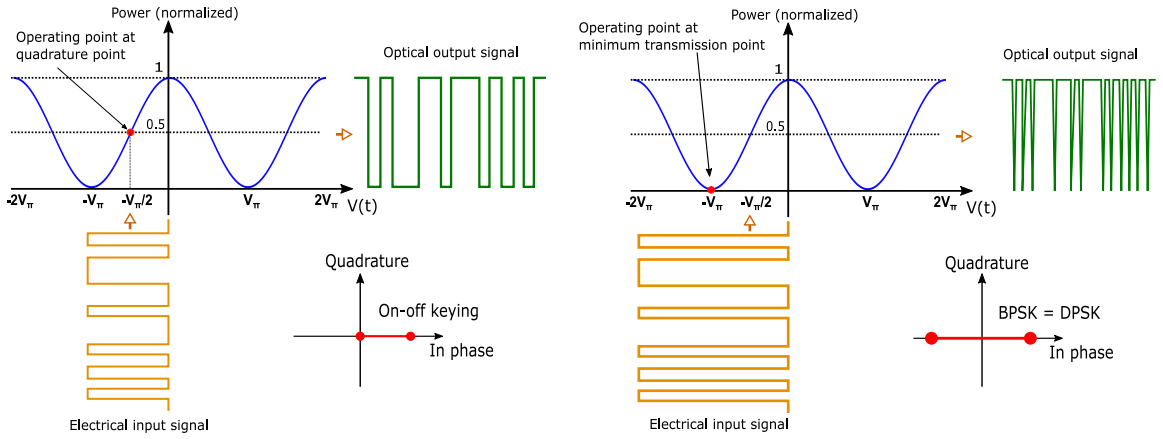

Figure 3.4: Transfer curve of an MZM for NRZ modulation format (left) and for DPSK modulation format (right) [41].

Depending on the desired modulation format, the MZM shall be driven with a bias voltage V_{bias} (DC-voltage) to achieve the optimal operating point for the target transmission of the modulator. As example, it is represented in Figure 3.4 the output signal of an MZM for two different bias voltages. In Figure 3.4 (left), the bias voltage is $V_{\text{bias}} = -V_\pi/2$. This

matches the quadrature point of the device. Applying a modulated electrical signal $V(t)$, whose peak-peak voltage is $V_{\mathrm{pp}} = V_\pi$, a nonreturn-to-zero (NRZ) modulation format is obtained. However, the bias voltage can be shifted as shown in Figure 3.4 (right), changing the modulation format. The operating point is in this example $V_{\mathrm{bias}} = -V_\pi$. The electrical signal has a peak-peak voltage of $V_{\mathrm{pp}} = 2V_\pi$. In addition to the amplitude modulation, a π phase skip occurs when $V(t)$ crosses $-V_\pi$. The result is a differential phase-shift keying (DPSK) modulation of the optical output signal.
Additionally, the bias voltage can be also adjusted to compensate for a possible imbalance of the MZM arms due to thermal changes, fabrication imperfections or material irregularities. This mitigates performance degradation due to undesired asymmetries or unstable thermal conditions. Hence, distortions of the output signal can be avoided if the operating point of the modulator is accordingly adjusted. An example of distortions on the output signal if the operating point is shifted is shown in Figure 3.5.

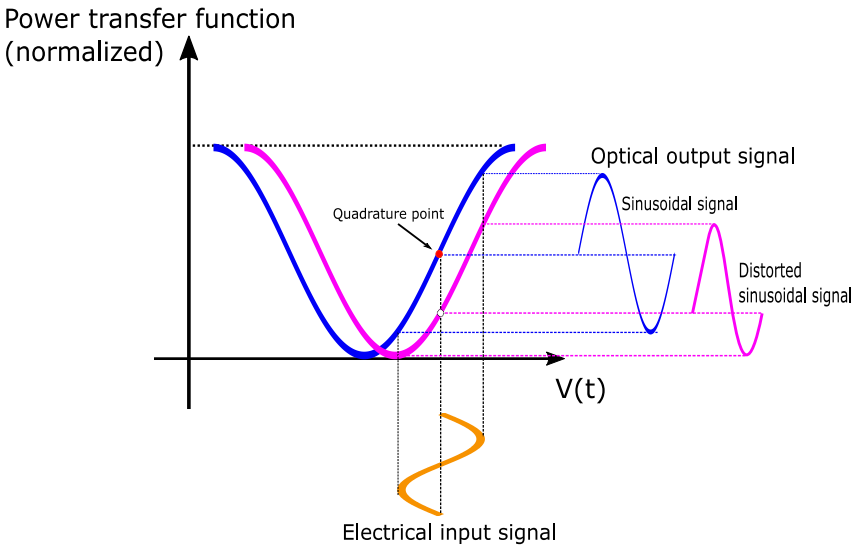

Figure 3.5: Impact on the optical output signal of the MZM for a drift of the operating point [42].

3.1.1.2.3 IQ-modulator The IQ-modulator is a complex device formed by an MZI with an MZM in each of the arms. One of the arms includes a phase shifter. A scheme of the device is shown in Figure 3.6. The light is split into two waveguides: the I-phase arm and the quadrature Q-phase arm. Each of the optical paths is modulated with a push-pull MZM. The phase shifter of one of the arms modifies the phase of the optical wave, generally the phase is shifted $\pi/2$. Accordingly, a complex modulation in the IQ-plane can be obtained by means of the recombination of the two optical signals from each

interferometer arm at the output of the IQ-Modulator.

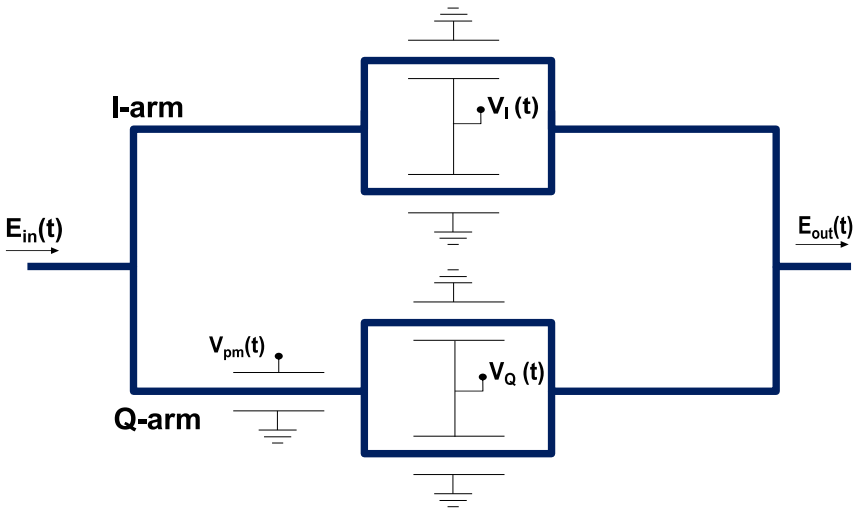

Figure 3.6: Optical IQ-modulator.

The phase shift of each MZM, i.e. each arm of the IQ-modulator, is defined as

$$\varphi_{\mathrm{I}}(t) = \frac{\pi V_{\mathrm{I}}(t)}{2V_{\pi}} \tag{3.13}$$

for the I-arm and for the Q-arm is defined as

$$\varphi_{\mathrm{Q}}(t) = \frac{\pi V_{\mathrm{Q}}(t)}{2V_{\pi}}. \tag{3.14}$$

Therefore, the output electric field of the IQ-Modulator yields

$$E_{\mathrm{out}}(t) = \frac{E_{\mathrm{in}}(t)}{2}\cos(\varphi_{\mathrm{I}}(t)) + j\frac{E_{\mathrm{in}}(t)}{2}\cos(\varphi_{\mathrm{Q}}(t)). \tag{3.15}$$

An example where this construction is used is the quadrature phase-shift keying (QPSK) modulator. This is formed by two identical MZMs, each working with a push-pull configuration whose optical output signal is binary phase-shift keying (BPSK) modulated. This means, a phase modulation with two phases, $\varphi = 0$ and $\varphi = \pi$. One of the arms, the Q-arm, is phase shifted $\pi/2$ and recombined with the I-arm, resulting in a QPSK modulation as shown in Figure 3.7(a).

Depending on the desired modulation format, there are different possibilities for designing an IQ modulator. This can be realized by changing the modulation of the MZMs that forms the IQ-Modulator and the phase shifter. For instance, if on each MZM an electrical four amplitude level modulation signal is applied, the result is a 16-quadrature amplitude

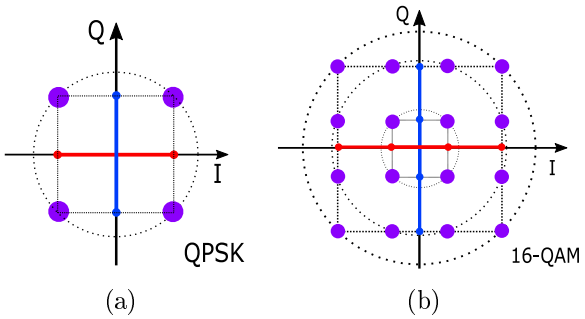

Figure 3.7: Signal constellation mapping for (a) QPSK and (b) 16-QAM.

modulation (16-QAM) format as shown in Figure 3.7(b). Thereby, the complexity of the optical system increases, but high data rates can be achieved.
Based on the QPSK modulator, an enhanced design can be realized adding a further variable, the light polarization. This kind of device is called DP-QPSK modulator, as mentioned in chapter 1.1. A detailed scheme of a DP-QPSK modulator is depicted in Figure 3.8.

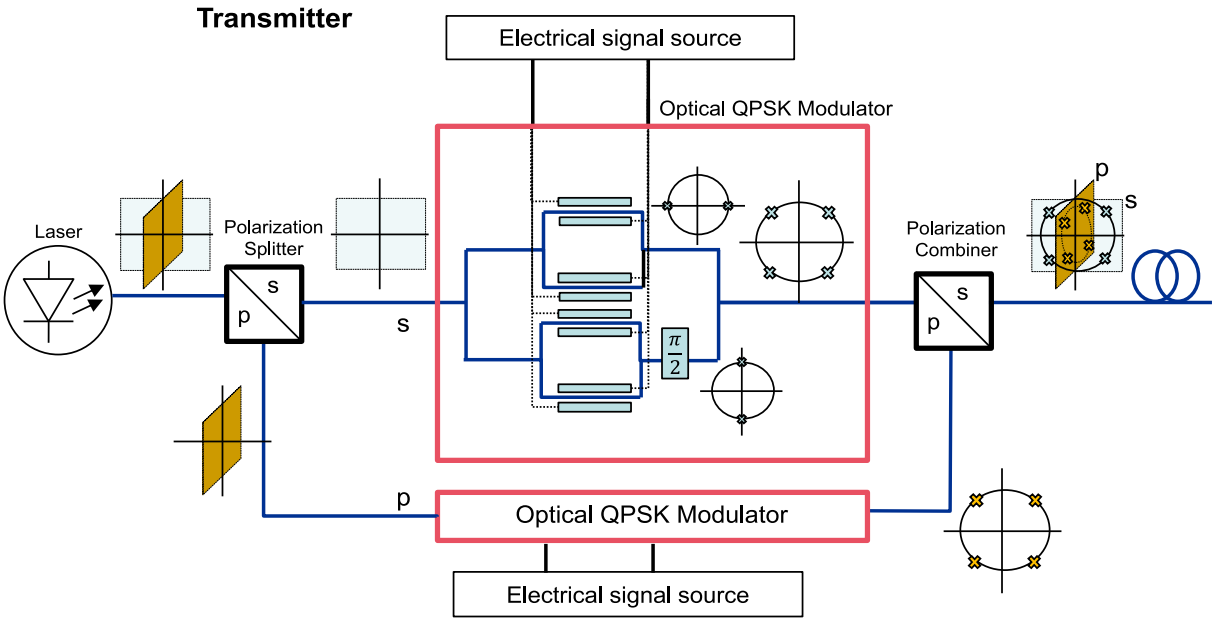

Figure 3.8: Block diagram of a DP-QPSK optical transmitter.

The light is split into two orthogonal polarizations by means of a polarization splitter. This allows the increase of the data rate: Each polarization is fed by a separate QPSK modulator. If the polarization splitter is a one-dimensional grating coupler, the transmitted light at the outputs of the splitter are in TE and in TM polarization. This means,

that the design points differ for each polarization.
However, if a two-dimensional grating coupler is used as polarization splitter (as presented in chapter 2), the two orthogonal polarizations are split, but at each of the outputs the transmitted light through the waveguides is TE polarized. This simplifies the design and fabrication of the device. Since it allows the use of the same QPSK modulator for both optical paths (s- and p-polarization paths) and the effort is focused on the optimization of only one QPSK modulator instead of two, one for each polarization.
After the modulation of the two optical paths, s and p, the light signals are again recombined by means of a polarization combiner, e.g. a 2DGC. Finally, at the output of the DP-QPSK optical transmitter 8 symbols can be obtained. Four of them in the s-polarization plane and the other four symbols in the orthogonal p-polarization plane.

3.1.2 Optical link

The basic element of an optical link has the same aim as in other communication systems: the transmission of information from one point to another. For this purpose, optical fibers or integrated optical waveguides can be used. These structures are formed by a core and a cladding surrounding the core. The refractive index of the core is higher than the refractive index of the cladding. Hence, by the condition of total internal reflection (TIR) at the core-cladding interface, the light is confined at the core and guided along the waveguide. The optical fibers are used mostly for long distances. There are two main types of optical fibers: SMFs and multimode fibers. SMFs have a thin enough core that only one mode can propagate through the fiber.
From the geometry and fabrication method point of view, it can be found fibers with one or multiple cores and even with a periodical arrangement of holes forming a photonic crystal fiber (PCF) [43] [44]. For special applications, optical fibers are fabricated, which preserve the polarization along the propagation of the light through the fiber. This is the case for the polarization-maintaining fiber (PMF)[45].
Similar types of configurations exist for integrated optical waveguides. They are used for short distances, i.e. on chip. There are two main types of waveguides: the planar and the nonplanar waveguides. The core of the planar waveguide, also called film, is between two cladding layers. The upper one is called cover and the lower one is the substrate. These waveguides confine the light in one transverse direction. For the case of the nonplanar waveguide, the core is surrounded by the cladding in all transverse directions, allowing a two-dimensional transverse confinement of the light. Different structures can be fabricated depending on the goal and the material. Some examples of nonplanar optical waveguides

are shown in Figure 3.9.

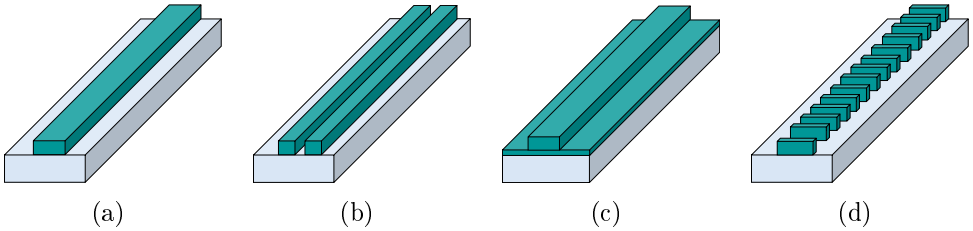

Figure 3.9: Different nonplanar integrated waveguides:(a) strip waveguide, (b) slot waveguide, (c) rib waveguide and (d) subwavelength waveguide.

For the design of the optical modulators in this work, strip and rib waveguides are used where the core and the slabs are made of silicon and the surrounded cladding is silicon dioxide. The SOI technology uses a high refractive index contrast between the core and the cladding of the structure. This allows for a higher density of components in optical circuits, reduces the parasitic capacitance and increases the bandwidth [46].
As mentioned before, the propagation of the light is due to the TIR of the light. The incident electromagnetic wave is totally reflected at the interface between core and cladding. Nevertheless, the light penetrates slightly the cladding to fulfill the boundary conditions at the interface, i.e. continuity condition of the electric field. The electric field decays exponentially when it passes through the interfaces. In order to achieve TIR, the refractive index of the core n_f (film layer) has to be higher than the one of the cladding $n_\mathrm{c,s}$ (cover and substrate). The angle of incidence of the light must be larger than the critical angle θ_c given by

$$\theta_\mathrm{c} = \arcsin\left(\frac{n_\mathrm{c,s}}{n_\mathrm{f}}\right). \tag{3.16}$$

In Figure 3.10 the TIR effect is depicted. It shows the propagation of the electromagnetic wave through the waveguide and the penetration of the wave into the cladding to accomplish the boundary conditions of the electric field.
The plane wave traveling along the waveguide can be described as the superposition of two plane waves. One along the propagation direction defined by

$$k_\mathrm{z} = \beta = k_0 \cdot n_\mathrm{f} \cdot \sin\theta \tag{3.17}$$

and the other one transverse to the propagation direction given by

$$k_\mathrm{y} = k_0 \cdot n_\mathrm{f} \cdot \cos\theta, \tag{3.18}$$

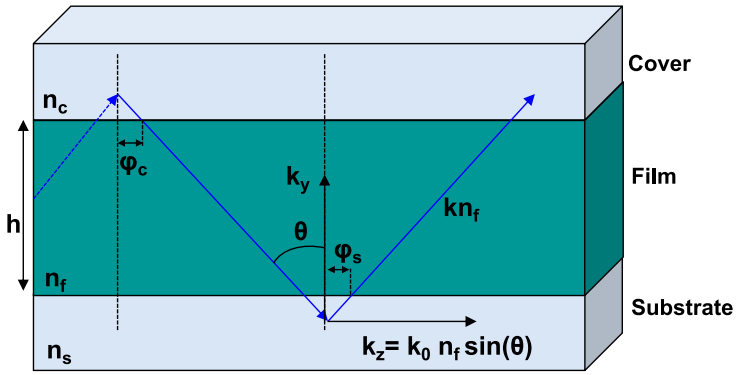

Figure 3.10: Scheme of total internal reflection of the light in an optical waveguide.

where β is the propagation constant, k_0 is the free space wave number, θ is the incidence angle and n_f is the refractive index of the film layer.
The plane wave transversal to the propagation direction k_y travels up and down through the film with the thickness h. In order to obtain constructive interference, the total phase shift for one cycle must be a multiple of 2π. In addition, the phase shift associated with the reflections at the boundaries of the core, called Goos-Hänchen shift [47] shall be considered. The phase shift of the upper and lower interface is denoted by φ_c and φ_s, respectively. The electromagnetic wave shall fulfill the characteristic equation given by

$$2 \cdot h \cdot n_\mathrm{f} \cdot k_0 \cdot \cos\theta + \varphi_\mathrm{c} + \varphi_\mathrm{s} = 2m\pi, \tag{3.19}$$

where the mode number m is an integer $(0, 1, 2, ...)$ and only certain discrete values of θ fulfill the Equation 3.19. Besides, depending on the waveguide geometry, more than one mode can satisfy the characteristic Equation 3.19.
Different modes have different propagation constants. The propagation of multiple modes causes dispersion of the signal. Therefore, commonly monomode waveguides are used to avoid undesired dispersion effects. These waveguides are designed for a limited range of frequencies where only one mode can propagate.
The propagation constant of the wave depending on the frequency and wave mode m is defined as

$$\beta_\mathrm{m} = \frac{w}{v_\mathrm{ph,m}} = \frac{2\pi f}{v_\mathrm{ph,m}} = k_0 \cdot n_\mathrm{f} \cdot \sin\theta_\mathrm{m} = k_0 \cdot n_\mathrm{eff,m}, \tag{3.20}$$

where w is the angular frequency, f is the frequency and $v_\mathrm{ph,m}$ refers to the phase velocity of each electromagnetic wave mode m. The incident angle θ_m and the effective refractive index $n_\mathrm{eff,m}$ are different for each wave mode m.

3.1.3 Optical receiver

The optical receiver is a device that converts an optical signal into an electrical signal. From a microscopic point of view, the optical detector converts photons into electrons. The aim of the receiver is to extract the information of the optical signal and transmit it to an electrical circuit as an analog or digital signal as a sequence of pulses. Therefore, the principal properties of the detector to allow a high quality of the electrical signal are:

- High responsivity at the transmitted wavelength of the optical signal.
- High bandwidth, i.e. fast response of the photodetector.
- Low noise.

The simplest photodetector is formed by a pn-junction or pin-junction if an additional undoped region is added between the positive charged region (p) and the negative one (n). These structures are based on diodes, therefore they are also known as photodiodes. The material chosen for the fabrication of the photodiode absorbs the light over a specific wavelength range. When light within this wavelength range reaches the depletion region of the device, the photons generate electron-hole pairs. A reverse voltage is applied to the photodiode, which provides the energy to build the depletion region and drift the generated charges to the electrical contacts of the device originating the photocurrent.
Different types of photodiodes can be fabricated modifying the photodetector structure, e.g. Schottky-photodiode [48], or the bias voltage.
This is the case of the avalanche photodiode, where the reverse bias voltage is increased significantly. A photon generates an electron-hole pair, the charge carriers are accelerated by the strong electrical field and collide with the atoms of the crystal in the avalanche region, the impact generates new carriers. Thereby, the photocurrent is increased by a avalanche multiplication factor M [48]. These photodiodes can be used for direct amplitude modulation detection [49][50]. However, if the modulation realized is in phase and the polarization of the light is used to transmit different data signals, a more complex receiver is required. This is the case of the coherent detector where the optical signal can be split and phase detected.
The components of the diagram relative to the coherent receiver presented in Figure 1.1 are extracted and shown in Figure 3.11.
A coherent detector can be used for the demodulation of a DP-QPSK modulated signal. The polarization is split and afterwards two coherent detectors, one per polarization, are

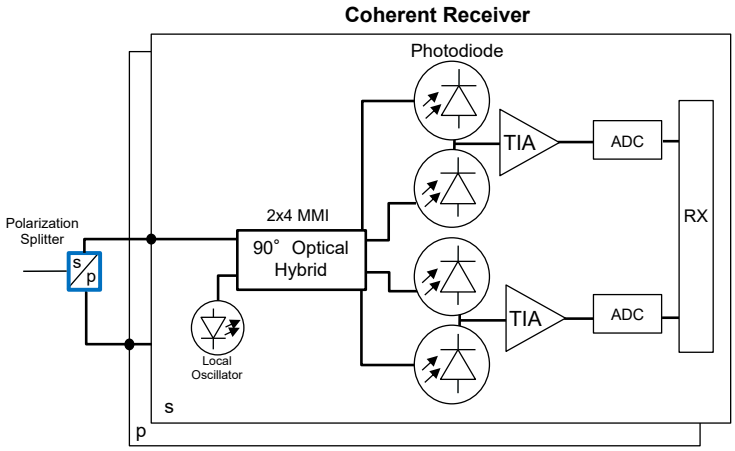

Figure 3.11: Block diagram of a DP-QPSK optical coherent receiver.

used. The coherent detector has a local oscillator (LO) to detect the phase of the signal. This is done using a multimode interference coupler (MMI) to mix the LO signal with the data signal. The MMI has four outputs with an equally spaced phase shift of 90°. Therefore, the optical signal is now split into 4 different optical paths depending on the phase of the light. The optical signal detection can be done with balanced photodetectors, also known as differential detection. The balanced photodetectors are two identical anti-parallel connected photodiodes. They receive the signal coming from two of the outputs of the MMI. The output of the balance photodectors is given by the difference of the photocurrents. The common mode component of the signal is suppressed allowing the detection of the signal carrying the meaningful phase information. Moreover, this method enhance the signal-to-noise ratio of the receiver, since common fluctuations of the input signals, e.g. intensity noise of the source, are canceled out. The balanced photodetectors are followed by a TIA, which converts and amplifies the photocurrent into voltage. Thereby, the optical signal is converted to an electrical signal and it can be further transmitted by analog electrical circuits or digital electrical circuits if an ADC is implemented.

3.2 Numerical methods

During this work different software tools are used for the simulation of the optical modulator. The optical structure of the modulator is designed and simulated with the Multi-Physics Utility tool [51] of Synopsys' RSoft. This tool allows to simulate and analyze the electro-optical (EO) effect. The materials can be doped and the carrier concentration

can be modified. The effect of an external voltage on the carrier distribution and on the effective refractive index of the propagating wave are analyzed for the design of the modulator. The Multi-Physics Utility tool calculates the doping concentration by means of the Equation 3.7 and Equation 3.8. The exact values for the refractive indexes of the silicon and the silicon dioxide at $\lambda = 1550\,\text{nm}$ are $n_{\text{Si}} = 3.47571$ and $n_{\text{SiO}_2} = 1.44402$, respectively [52]. The imaginary component of the refractive index is $< 10^{-8}$, therefore the losses due to the absorption of the intrinsic Si at $\lambda = 1550\,\text{nm}$ can be neglected.
As mentioned in chapter 2.2, the optical modes of the waveguides are calculated using the software FIMMPROP of PhotonDesign. The results of the optical modes obtained with FIMMPROP are imported to RSoft. In RSoft the structure is simulated with the finite element method (FEM) using the tool FemSIM [53]. The FEM method basically splits the computational structure into individual small areas finding local solutions that fulfill the differential equations within the boundaries of the area. The appropriate meshing size of the simulation window is decisive for the veracity of the results. If the grid cell side does not match the waveguide edge, two different materials and therefore two refractive indexes would be defined inside of the same cell. This fact results in a wrong calculation of the electric field and mode profile of the waveguide. The model used in the calculations is a 2D model of the cross section of the doped waveguide.
For the design of the electrical transmission line (TL), the simulation tool Momentum of Advanced Design System (ADS) [54] is used. This tool solves embedded passive planar structures in a multilayer-substrate with a numerical discretization technique called the method of moments (MoM) using precomputed Green's functions. The simulations realized during this work are solved with the simulation mode Momentum microwave. This mode uses the full-wave Green's functions, that characterize the substrate without simplifying the Maxwell equations. With Momentum complex electromagnetic effects, including the skin effect, a substrate with multiple dielectric layers and thick metals, can be simulated.

3.3 Design in 250 nm SOI platform

A 250 nm SOI platform fabricated at IMS CHIPS is the technology used for the design of the modulator. High performance photonic devices CMOS compatible as 1DGCs [8], polarization splitters [22] or MMIs [55] are designed and fabricated with this technology showing excellent results. These structures can be used as part of the components of a Si modulator, since they offer an important benefit to reduce the total loss of the device.

Therefore, a first design of a silicon optical modulator based on this technology is realized in this work serving as a preliminary step for the fabrication of a low loss and highly efficient modulator in a CMOS compatible technology.
Using a new technology requires a complete new design of the modulator to achieve optimal results. During this work, the influence on the modulator performance of the most important design parameters is investigated. First, the geometry of the waveguide is calculated for single mode propagation and low loss. Afterwards, different doping concentrations and profiles are simulated to analyze the impact on the modulation efficiency of the device. A die with test structures and different modulator designs is fabricated. The measurement results are presented as a validation of the technology and an equivalent circuit model is developed based on the results. In addition, further simulations are realized to improve the doping profile to achieve higher modulation efficiency and reduce the optical loss of the modulator. Finally, other MZM designs are fabricated with a different technology and the results are compared with the work of other research groups.

3.3.1 Description of the device

The SOI wafer used is the same as the one described for the 2DGC designs in chapter 2. This has a Si substrate with a thickness of 625 µm and a 3 µm thick SiO_2 BOX layer. On top it is the active silicon layer in which the photonic structures are etched. This Si layer has a thickness of 250 nm. The structures are passivated with a 1 µm SiO_2 layer. For the fabrication of the electrical metal lines of the modulator an extra layer is added over the passivation. This aluminum (Al) metal layer (precisely AlSiCu alloy) has a thickness of 500 nm. The 250 nm active Si is connected to the top metal through vias. A scheme of the resulting platform after adding the top metal layer is presented in Figure 3.12.

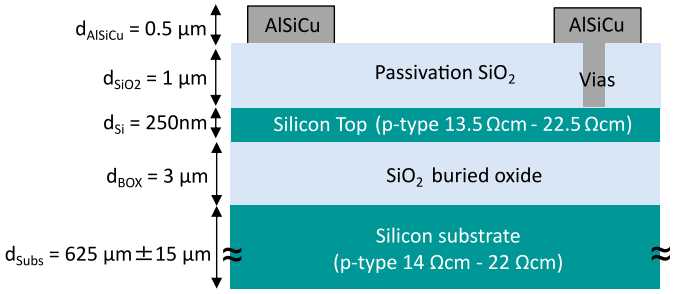

Figure 3.12: Scheme of the platform used for the fabrication of the modulator.

A scheme of the designed MZM is illustrated in Figure 3.13. The optical signal coming from an optical fiber is coupled into the optical modulator by means of a 1DGC followed

by a linear adiabatic taper. The light is transmitted by means of a monomode waveguide to a 1x2 MMI. The MMI splits the light uniformly to the two branches of the MZM. Each branch has a doped Si waveguide in order to reduce asymmetries of the two branches and therefore improve the ER of the modulator. One of the doped waveguide branches is connected to an RF coplanar transmission line through vias. Thereby, the electrical signal is applied to the optical structure to perform the phase shift. The modulator is single drive, i.e. only one branch works as phase shifter, for an easier characterization and comparison with the simulations results. An optical delay line is integrated in one branch to increase the optical path difference between the arms in order to reduce the free spectral range of the optical transmission spectrum. Therefore, the analysis of the measurement results of the phase shift produced by the modulator can be easily done. Since only a small wavelength range can be measured to observe the phase shift. The optical signal of the two branches is again combined with a 2x1 MMI. Then, the light propagates through a monomode waveguide and a linear adiabatic taper. Finally, the light is coupled out of the embedded modulator to an optical fiber by means of another 1DGC.

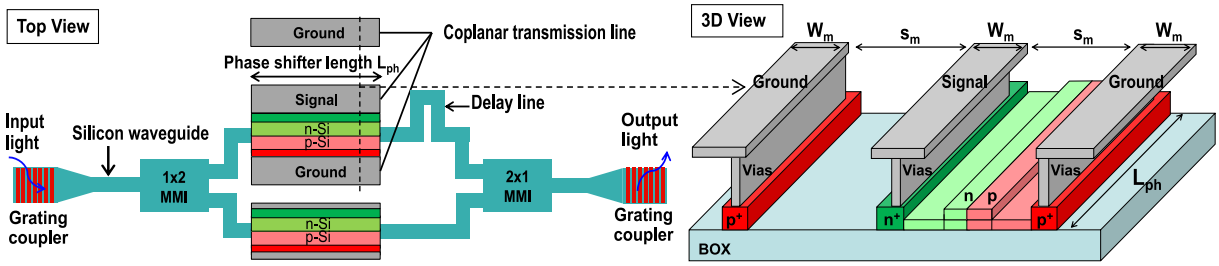

Figure 3.13: Scheme of the designed Mach-Zehnder modulator.

The modulation relies on the free carrier plasma dispersion effect. A reverse bias voltage is applied to the modulator generating a depletion region in the pn-junction of the rib waveguide. A change in the density of free carriers leads to a change in the refractive index Δn and therefore the phase of the optical signal is modified. This results in an amplitude modulation of the optical signal at the output of the MZM. It shall be also considered that the existence of the free carries implies attenuation of the optical signal. The change of the refractive index and the absorption coefficient for a wavelength of 1550 nm is described by the Equation 3.7 and Equation 3.8.

3.3.2 Optical simulations

3.3.2.1 Rib waveguide dimensions

A research on the rib waveguide dimensions of the phase shifter is realized for the transmission of a single mode TE wave at the telecommunication wavelength of 1550 nm. In Figure 3.14(a), a cross section of the rib waveguide with the most important geometric parameters is shown. The height $h = 250\,\text{nm}$ of the core and the contact regions is determined by the thickness of the active Si layer of the SOI platform. In order to choose the optimal dimension for the transmission of a single mode signal, the mode profile of the optical wave is simulated for different widths w. The results show that for a core width of $w \geq 420\,\text{nm}$, the second order TE mode can propagate. However, for narrow waveguides the fundamental TE mode is not well confined in the Si core. In this case, the absorption and therefore the attenuation α increase if the slabs of the rib waveguide are highly doped. For this reason, the waveguide core should be designed as wide as possible. Thus, the waveguide width is set to $w = 400\,\text{nm}$ keeping a fabrication tolerance range of 20 nm to avoid multimode propagation.

The RF coplanar metal lines of the modulator are connected by means of the metal vias to a 250 nm thick highly doped Si region to reduce the ohmic contact. The slab width s is defined as the distance between the metal contact region and the waveguide core. This parameter shall be optimized to avoid high losses of the optical signal, due to the absorption caused by the highly doped Si region with a carrier density of about $1 \cdot 10^{20}\,\text{cm}^{-3}$ and the metal vias. The metal has a complex refractive index $n = n + i\kappa$, causing a strong attenuation of the optical modes. The distance s should be chosen to be as large as possible. However, a greater distance s means that the electrical resistance increases and therefore the electrical performance of the modulator is affected. The dependency of these parameters are shown in Figure 3.14(b), where the calculated results of the total resistance R are plotted. This resistance is given in Ωcm, since it is normalized with the phase shifter length L_{ph} of 1 cm. In order to obtain the total resistance of the slabs in Ω, the results shown in Figure 3.14(b) have to be divided by L_{ph}.

The calculations of R are realized for different slab thicknesses h_{sl} and for two doping densities. The parameter N_{a} refers to the doping concentration of the acceptors, i.e. holes and N_{d} refers to the doping concentration of the donors, i.e. electrons. In Figure 3.14(b), the blue lines correspond to a doping concentration of the p- and n-doped regions of $N_{\text{a}} = N_{\text{d}} = 1 \cdot 10^{17}\,\text{cm}^{-3}$. The red lines are the results for a doping concentration of the p- and n-doped regions of $N_{\text{a}} = 1 \cdot 10^{17}\,\text{cm}^{-3}$ and $N_{\text{d}} = 1 \cdot 10^{18}\,\text{cm}^{-3}$, respectively.

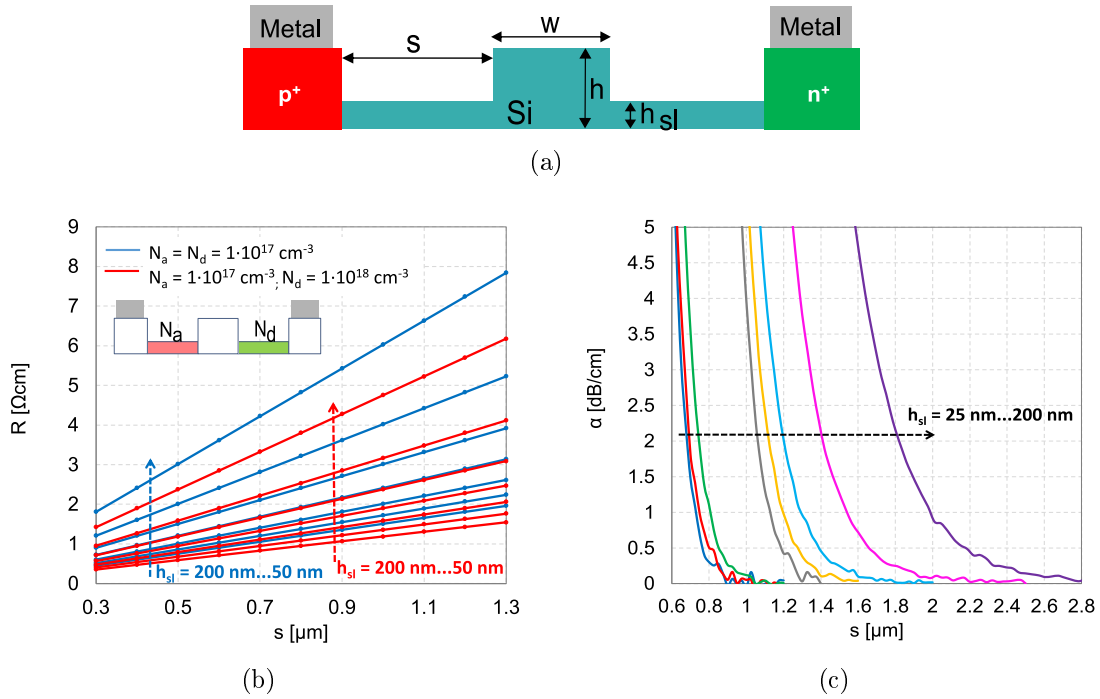

Figure 3.14: (a) Scheme of the Si rib waveguide. (b) Calculation results of the total resistance $R = R_\mathrm{n} + R_\mathrm{p}$ of the waveguide slabs depending on the thickness h_sl and the slab width s for two doping concentrations. (c) Simulation results of the loss α depending on s for different slab thicknesses h_sl. The core dimensions are $h = 250\,\mathrm{nm}$ and $w = 400\,\mathrm{nm}$.

The total resistance in Ωcm is calculated as

$$R = R_\mathrm{n} + R_\mathrm{p} = \frac{s \cdot \rho_\mathrm{n}}{h_\mathrm{sl}} + \frac{s \cdot \rho_\mathrm{p}}{h_\mathrm{sl}}, \tag{3.21}$$

where R_n and R_p are the resistances in Ωcm (normalized with the phase shifter length of 1 cm) of the n- and p-doped slabs. The parameters ρ_n and ρ_p represent the resistivity of the n- and p-doped silicon, respectively.

The attenuation α depending on the distance s is simulated for different slab thicknesses h_sl. The simulated rib waveguide is shown in Figure 3.14(a). The core and the slabs of the structure consist of intrinsic Si. However, the silicon of the contact regions is highly doped. The results are plotted in Figure 3.14(c). It is observed that at the same distance s the attenuation is higher if the slab thickness increases. This is caused by the fact that for higher values of h_sl a higher portion of the electric field of the propagated optical wave is outside of the core region. Therefore, the loss increases because of the presence of the highly doped region and the metal contact in the proximity of the wave. The ratio

h_{sl}/h should be chosen as small as possible to keep the optical mode confined within the waveguide core.
In the following, the slab thickness chosen for the modulator design is $h_{sl} = 50\,\text{nm}$ in order to keep the optical mode confined in the core of the waveguide. The distance to the contact region is set to $s = 1.25\,\mu\text{m}$ to minimize the optical loss.

3.3.2.2 Doping profile

The next step in the design of the modulator is the determination of the doping profile to obtain a high modulation efficiency and low loss. For this reason, the change of the effective index Δn_{eff} and the absorption coefficient α is simulated with the Multi-Physics Utility tool of the Synopsys' RSoft software for different doping profiles.
For the choice of the optimal doping concentration, a compromise has to be sought. A high doping concentration leads to a large change in the effective refractive index. However, the optical loss also increases with the free carrier density. In this chapter, the effect of different doping profiles is investigated.

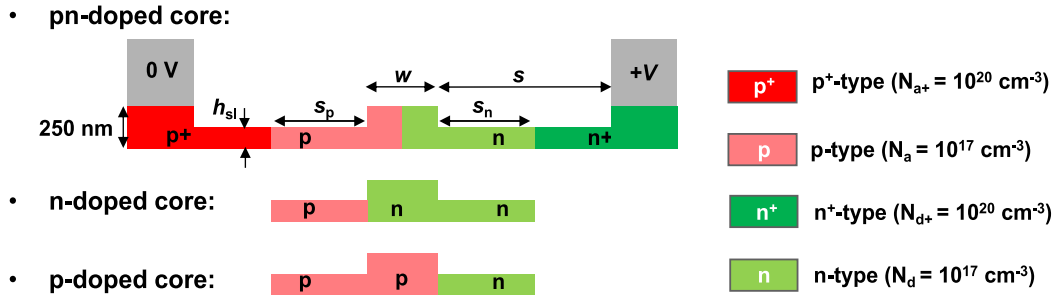

Figure 3.15: Three simulated doping profiles: pn-, n- and p-doped core. The rib waveguide dimensions are $h = 250\,\text{nm}$, $h_{sl} = 50\,\text{nm}$, $w = 400\,\text{nm}$ and $s = 1.25\,\mu\text{m}$.

In Figure 3.15, three doping profiles of the rib waveguide core are presented. The doping concentration of the highly doped regions is $N_{a+,d+} = 1 \cdot 10^{20}\,\text{cm}^{-3}$. The doping concentration of the lowly doped regions is $N_{a,d} = 1 \cdot 10^{17}\,\text{cm}^{-3}$. The distance from the p^+- and from the n^+-doped regions to the waveguide core is defined as s_p and s_n, respectively. In a first step, these distances are kept the same as the slab width, i.e. $s = s_p = s_n = 1.25\,\mu\text{m}$. Thereby, the calculated loss is derived only from the carrier absorption of the lowly doped Si.

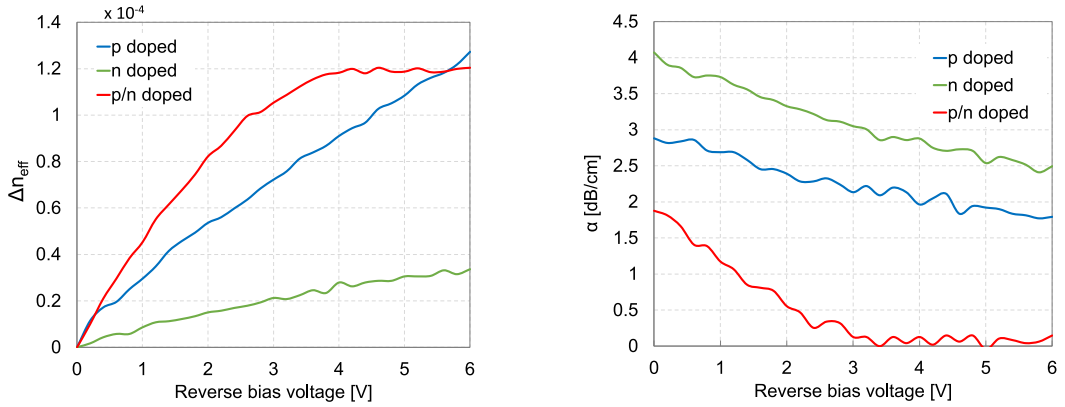

(a) (b)

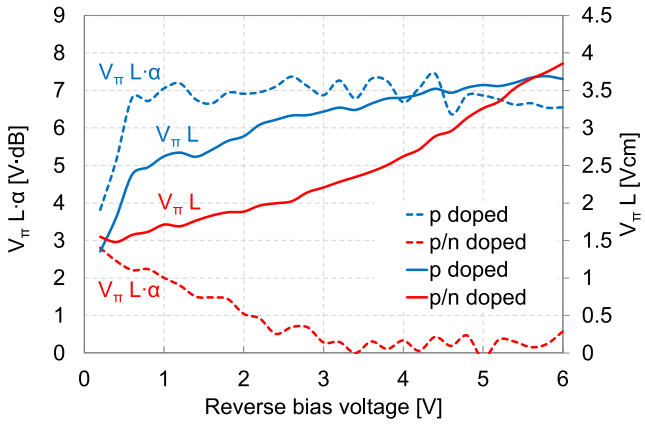

(c)

Figure 3.16: Simulation results of (a) the change of the effective refractive index Δn_{eff}, (b) the attenuation α, (c) the modulation efficiency $V_\pi L$ and the figure of merit $V_\pi L \cdot \alpha$ depending on the reverse bias voltage for different doping profiles of the waveguide core. $N_\text{a} = N_\text{d} = 1 \cdot 10^{17}\,\text{cm}^{-3}$, $s_\text{p} = s_\text{n} = s = 1.25\,\mu\text{m}$ and $h_\text{sl} = 50\,\text{nm}$.

The change of the effective index of the fundamental mode for the three doping profiles is simulated. The results are compared in Figure 3.16(a). For the waveguide with a p-doped core, the Δn_{eff} is more than three times higher than for the waveguide with the n-doped core for the same bias voltage. Besides, the attenuation α is lower for the p-type doping than for the n-type doping. This can be observed in Figure 3.16(b). The results at 0 V bias show the maximum attenuation of the carrier-depletion modulator for that doping configuration. For higher reverse bias voltages the free carrier density in the core is lower, since the depletion region is wider.

For the pn-doped core, Δn_{eff} increases with the reverse voltage faster than for the p-doped core. However, it flattens at reverse voltages higher than 4 V. In addition, the attenuation is lower than for the p- and n-doped core for all the simulated reverse bias voltages, showing very low attenuation values for bias voltages higher than 3 V. This is due to the carrier-depletion effect that is greater for a pn-doped core than for a purely p- or n-doped core. The maximum of the E-field of the optical wave is located in the middle of the core and the change of the carrier density is maximized in this region for the pn-doped core profile.

Figure 3.16(c) shows a comparison of the modulation efficiency $V_\pi L$ vs. the bias voltage of the modulators with a p- and pn-doped core waveguide. The modulation efficiency is defined as the product of the applied voltage needed to achieve a phase shift of π with a phase shifter length of L_{ph}. A smaller $V_\pi L$ denotes a higher modulation efficiency. Modulators with a lower $V_\pi L$ require less die area or lower bias voltage. A lower $V_\pi L$ efficiency is considered better. The modulation efficiency is calculated as

$$V_\pi L = \frac{\lambda \cdot V_{\text{bias}}}{2 \cdot \Delta n_{\text{eff}}} = \frac{\lambda \cdot V_{\text{bias}}}{2(n_{\text{eff},\text{V}_{\text{bias}}} - n_{\text{eff},\text{V}_{\text{bias}}=0\,\text{V}})}, \tag{3.22}$$

where V_{bias} is the applied reverse bias voltage and $n_{\text{eff},\text{V}_{\text{bias}}}$ is the effective index at the applied voltage V_{bias}. The parameter $n_{\text{eff},\text{V}_{\text{bias}}=0\,\text{V}}$ is defined as the effective index at the bias voltage $V_{\text{bias}} = 0\,\text{V}$ and λ refers to the wavelength.

The figures of merit $V_\pi L \cdot \alpha$ of both devices are also compared. The figure of merit is a combination of the modulation efficiency of the modulator with the respective optical loss due to the free carrier absorption.

Observing the simulation results presented in Figure 3.16(c), the pn-doped core exhibits a lower $V_\pi L$ than the p-doped core up to 5.5 V. For higher bias voltages, the free carriers effect is reduced because most of the free carriers are already outside the waveguide core. The $V_\pi L \cdot \alpha$ is significantly lower for the pn-doped core due to the low number of free carriers in the core. The low number of free carriers reduces loss.

For the pn-doped core, the simulations show a $V_\pi L = 1.9\,\text{Vcm}$ and $V_\pi L \cdot \alpha = 1\,\text{V} \cdot \text{dB}$ for a reverse bias voltage of 2 V. For the case of a p-doped core the modulation efficiency is $V_\pi L = 2.9\,\text{Vcm}$ and around $V_\pi L \cdot \alpha = 7\,\text{V} \cdot \text{dB}$ at the same bias voltage. For higher reverse voltages, for example at $V_{\text{bias}} = 6\,\text{V}$, the $V_\pi L$ parameter increases. The results for the pn-doped core are in this case $V_\pi L = 3.9\,\text{Vcm}$ and $V_\pi L \cdot \alpha = 0.6\,\text{V} \cdot \text{dB}$. For the p-doped core the values obtained at 6 V are $V_\pi L = 3.7\,\text{Vcm}$ and $V_\pi L \cdot \alpha = 6.5\,\text{V} \cdot \text{dB}$.

The free carrier distribution of the p-doped and pn-doped core waveguide is simulated for three reverse bias voltages, 0 V, 3 V and 6 V. The results are illustrated in Figure 3.17.

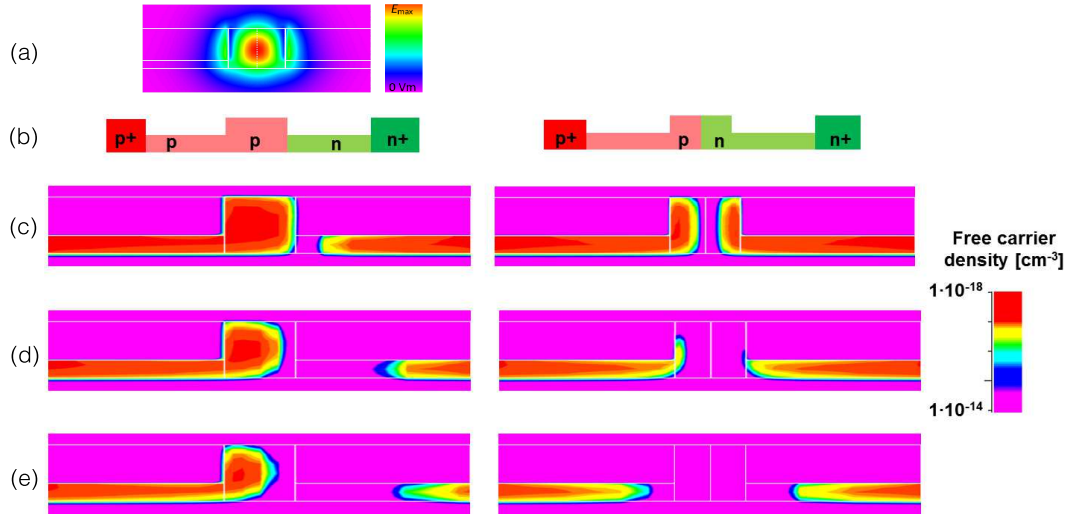

Figure 3.17: (a)E-field profile of the fundamental mode in the rib waveguide. (b) Cross section of the doping profile of a p-doped (left) and pn-doped (right) waveguide with $N_a = N_d = 1 \cdot 10^{17}\,\mathrm{cm}^{-3}$. (c) Simulation results of the free carrier density applying a reverse bias voltage of 0 V, (d) 3 V and (e) 6 V.

This shows the working principle of the carrier-depletion modulator and explains the simulation results of Figure 3.16. For both structures, the free carriers migrate towards the contact regions when the voltage rises. Figure 3.17(a) shows the E-field profile of the fundamental mode for both rib waveguide structures. The two simulated doping configurations of the waveguides are depicted in Figure 3.17(b). The left column of the figure shows the p-doped core waveguide. The depletion region is formed at the edge of the core. However, the maximum of the optical E-field lies in the center of the core and only a small portion overlaps with the carrier-depletion region. For the case of the pn-doped core, i.e right column, the depletion region is in the center of the core, where the maximum of the E-field of the propagating wave is located. Therefore, the attenuation is smaller than in the p-doped case, since the number of free carriers is lower. For a reverse bias voltage between 0 V and 3 V, Figure 3.17(c) and Figure 3.17(d), a strong change of the free carrier concentration occurs in the waveguide core where the optical field is confined. This explains a higher Δn_{eff} and lower $V_\pi L$ than for the p-doped core configuration. However, for reverse voltage larger than 4 V, the depletion region is wider than the waveguide core as shown in Figure 3.17(e). Hence, Δn_{eff} starts to flatten as shown in Figure 3.16(a), since almost all the free carriers are removed.

3.3.3 Electrical simulations

For the design of a high speed optical modulator the electrical performance of the device shall be investigated. Several factors have an impact on the bandwidth of the device. For example, the bandwidth and loss of the traveling wave electrode (TWE), i.e. TL connected to the optical doped waveguide, where the RF electrical signal propagates that modulates the light. In addition, a matching between the characteristic impedance of the TWE and the modulator driver and the termination impedance to avoid reflections. For modulators with a long phase shifter, the velocity of the optical and electrical wave shall be similar to achieve high speed modulation and a good quality of the modulated signal. Furthermore, an important factor of the optical modulators is the intrinsic RC-limit caused by electrical properties of the depletion region in the doped waveguide. A scheme of the phase shifter section of the modulator is shown in Figure 3.18.

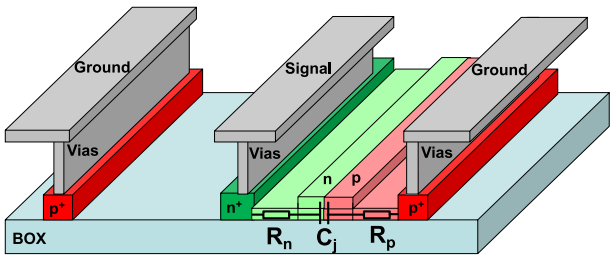

Figure 3.18: 3D view of the phase shifter with the intrinsic RC-circuit of the depletion region in the doped waveguide.

An analysis of the total resistance R of the slabs of the waveguide is realized in Chapter 3.3.2.1, where the resistance for different slab dimensions and doping concentrations is calculated with Equation 3.21 (Figure 3.14(b)). A further research is realized varying the width of the lowly doped Si slabs. The resistance R is calculated depending on the parameter $s_{\mathrm{n,p}} = s_{\mathrm{n}} = s_{\mathrm{p}}$ and the doping concentration. The results are plotted in Figure 3.19(a). As expected, the resistance increases for wider dimensions of the lowly doped slabs and decreases for higher doping concentrations. Due to the properties of silicon, the contribution of the p-doped region in the total resistance is higher than that of the n-doped. The resistivity of the p-doped Si is around twice as high as the n-doped Si for the same doping concentration.

The junction capacitance of the modulator C_{J} is calculated with the help of Equation 3.9,

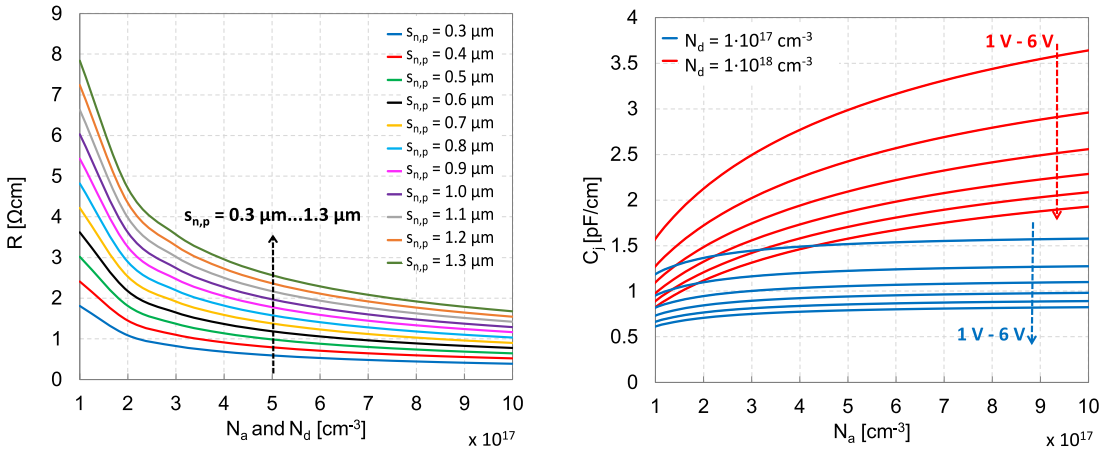

(a) (b)

Figure 3.19: (a) Total resistance R in Ωcm, normalized by the phase shifter length, of the symmetrically p- and n-doped slabs with $h_{\mathrm{sl}} = 50\,\mathrm{nm}$ depending on different doping concentrations and slab widths. (b) Junction capacitance per unit length, C_{j} in pF/cm, of the pn-doped region of the phase shifter.

which yields

$$C_{\mathrm{J}} = \epsilon_0 \epsilon_{\mathrm{r,Si}} \frac{A}{w_{\mathrm{dep}}} = A \cdot \sqrt{\frac{q \epsilon_0 \epsilon_{\mathrm{r,Si}} N_{\mathrm{a}} N_{\mathrm{d}}}{2(N_{\mathrm{a}} + N_{\mathrm{d}})(V_{\mathrm{bi}} - V_{\mathrm{bias}})}}, \tag{3.23}$$

where ϵ_0 is the permittivity of the free space and $\epsilon_{\mathrm{r,Si}}$ is the dielectric constant of silicon, q is the elementary charge, V_{bi} is the built-in potential voltage and V_{bias} is the applied bias voltage. The area $A = h \cdot L_{\mathrm{ph}}$ is defined by the height h of the pn-junction and the length L_{ph} of the phase shifter.

The junction capacitance per unit length $C_{\mathrm{j}} = C_{\mathrm{J}}/L_{\mathrm{ph}}$ is calculated for the reverse bias voltage range between 1 V and 6 V. The results are shown in Figure 3.19(b). The acceptor concentration N_{a} is varied for two donor concentrations N_{d}. The blue curves belong to $N_{\mathrm{d}} = 1 \cdot 10^{17}\,\mathrm{cm}^{-3}$ and the red curves show the results for $N_{\mathrm{d}} = 1 \cdot 10^{18}\,\mathrm{cm}^{-3}$.

The junction intrinsic RC 3 dB-bandwidth, i.e. the cut-off frequency f_{c}, is calculated according to

$$f_{\mathrm{c}} = \frac{1}{2\pi R_{\mathrm{s}} C_{\mathrm{J}}} \tag{3.24}$$

for the same doping concentrations as in Figure 3.19(b). The corresponding value of the C_{j} are obtained from this figure. The series resistance of the diode R_{s} is calculated using

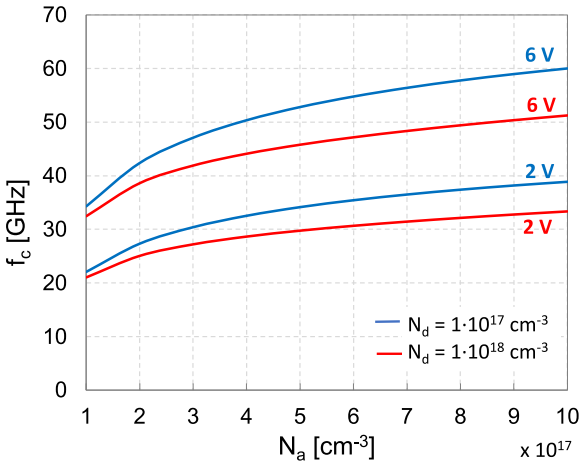

Figure 3.20: Cut-off frequency depending on the doping concentration and reverse bias voltage for a pn-junction in the center of the waveguide core for a length of the phase shifter of $L_{\mathrm{ph}} = 1\,\mathrm{mm}$ and $s_{\mathrm{n,p}} = 1.25\,\mu\mathrm{m}$.

the Equation 3.21 as

$$R_{\mathrm{s}} = \frac{R}{L_{\mathrm{ph}}} = \frac{R_{\mathrm{n}} + R_{\mathrm{p}}}{L_{\mathrm{ph}}}. \tag{3.25}$$

The cut-off frequency is calculated for two reverse bias voltages, 2 V and 6 V. In Figure 3.20, the calculated results for a phase shifter length of $L_{\mathrm{ph}} = 1\,\mathrm{mm}$ and a slab width of $s = s_{\mathrm{n,p}} = 1.25\,\mu\mathrm{m}$ are presented.

For $N_{\mathrm{d}} = 1 \cdot 10^{17}\,\mathrm{cm}^{-3}$ and $N_{\mathrm{a}} = 10 \cdot 10^{17}\,\mathrm{cm}^{-3}$, cut-off frequencies of 60 GHz ($R_{\mathrm{s}} = 32.1\,\Omega$ and $C_{\mathrm{J}} = 0.0826\,\mathrm{pF}$) and 39 GHz ($R_{\mathrm{s}} = 32.1\,\Omega$ and $C_{\mathrm{J}} = 0.128\,\mathrm{pF}$) are achieved at 6 V and 2 V reverse bias voltages, respectively. The resistivity of the doped silicon at these carrier concentrations are: $\rho_{\mathrm{n}} = 0.08653\,\Omega\mathrm{cm}$ for the phosphorous-doped silicon region and $\rho_{\mathrm{p}} = 0.04191\,\Omega\mathrm{cm}$ for the boron-doped silicon region [56]. For a higher donor concentration of $N_{\mathrm{d}} = 1 \cdot 10^{18}\,\mathrm{cm}^{-3}$ the decrease in the resistance does not compensate for the increase in capacitance and therefore lower cut-off frequencies f_{c} are achieved.

For the case of a p-doped core waveguide as presented in Figure 3.17(a) (left), the complexity of the calculation of the junction capacitance increases. This is due to the different heights of the p- and n-doped regions. In order to simplify the calculations, the pn-junction is modified. The height of the p-side is adjusted as depicted in Figure 3.21(a). This change can be realized without a significant change in the results if the doping of

the p-side is transformed by

$$N'_{\mathrm{a}} = N_{\mathrm{a}} \frac{h}{h_{\mathrm{sl}}}. \tag{3.26}$$

The relative width of the depletion region depending on the adjusted doping is calculated as

$$d_{\mathrm{n}} = w_{\mathrm{dep}} \frac{N'_{\mathrm{a}}}{N_{\mathrm{d}} + N'_{\mathrm{a}}}, \tag{3.27}$$

$$d_{\mathrm{p}} = w_{\mathrm{dep}} \frac{N'_{\mathrm{d}}}{N_{\mathrm{d}} + N'_{\mathrm{a}}}, \tag{3.28}$$

where w_{dep} is the depletion width according to Equation 3.9.

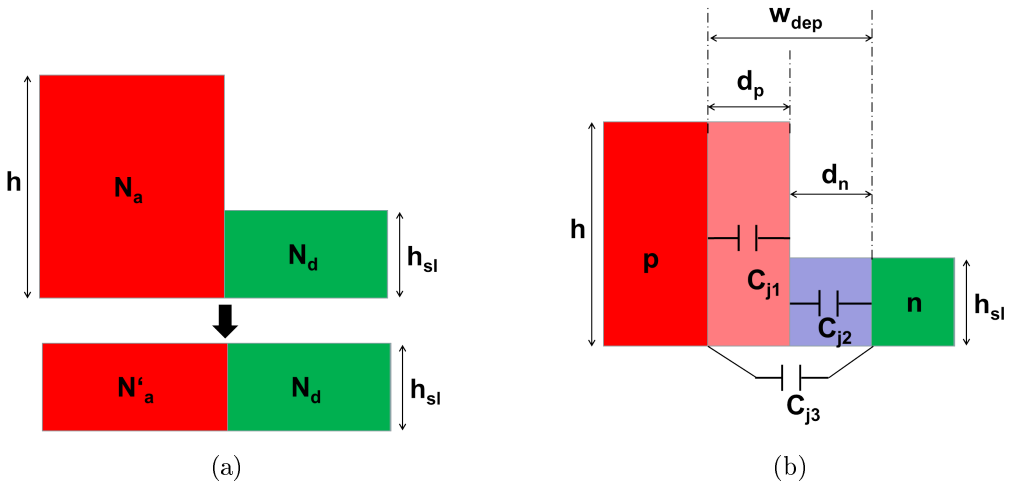

Figure 3.21: (a) Modification of the lateral pn-junction. (b) Relative capacitances for the simplification of the calculation of the total junction capacitance.

Then, the total junction capacitance per unit length is divided into three new capacitances as shown in Figure 3.21(b). This is calculated by

$$C_{\mathrm{j}} = \frac{1}{\frac{1}{C_{\mathrm{j1}}} + \frac{1}{C_{\mathrm{j2}}}} + C_{\mathrm{j3}}. \tag{3.29}$$

The numeric expressions for the relative capacitances C_{j1}, C_{j2} and C_{j3} are calculated as

$$C_{\mathrm{j1}} = \left(C_{\mathrm{ch_1}} - \epsilon_0 \epsilon_{\mathrm{r,Si}} \frac{h}{d_{\mathrm{p}}}\right) \frac{\epsilon_{\mathrm{r,SiO_2}}}{\epsilon_{\mathrm{r,Si}}} + \epsilon_0 \epsilon_{\mathrm{r,Si}} \frac{h}{d_{\mathrm{p}}}, \tag{3.30}$$

$$C_{\mathrm{j2}} = \left(C_{\mathrm{ch_2}} - \epsilon_0 \epsilon_{\mathrm{r,Si}} \frac{h}{d_{\mathrm{n}}}\right) \frac{\epsilon_{\mathrm{r,SiO_2}}}{\epsilon_{\mathrm{r,Si}}} + \epsilon_0 \epsilon_{\mathrm{r,Si}} \frac{h}{d_{\mathrm{n}}} \tag{3.31}$$

and

$$C_{\mathrm{j3}} = \frac{1}{2}\left(C_{\mathrm{ch_3}} - \epsilon_0 \epsilon_{\mathrm{r,SiO_2}} \frac{h_{\mathrm{sl}}}{w_{\mathrm{dep}}/2}\right), \tag{3.32}$$

using the method of conformal mapping as described by [57] including the effect of the electrical field out of the pn-junction defined as an equivalent capacitor C_{ch} and described in [58].
This model is used for the calculation of the junction capacitance and the expected cut-off frequency of the fabricated modulator with a p-doped waveguide core. The total junction capacitance per unit length of the fabricated device described in Figure 3.32 at 0 V bias voltage is

$$C_{\mathrm{j}} = \frac{1}{\frac{1}{9.19\,\mathrm{pF/cm}} + \frac{1}{1.078\,\mathrm{pF/cm}}} + 0.076\,\mathrm{pF/cm} \approx 1.04\,\mathrm{pF/cm}. \tag{3.33}$$

As validation, the same cross section is simulated using a different software tool for the 3D electromagnetic simulation of high frequency devices CST Studio Suite [59] with a result of 1.01 pF/cm for an ideal pn-junction of the structure. This matches well with the analytical model. The series resistance for a slab with $s_{\mathrm{n,p}} = 400\,\mathrm{nm}$, a thickness of $h_{\mathrm{sl}} = 80\,\mathrm{nm}$ and a phase shifter length of $L_{\mathrm{ph}} = 500\,\mu\mathrm{m}$ results in $R_{\mathrm{s}} = 30.3\,\Omega$. Therefore, the theoretical expected cut-off frequency due to the RC-limit of the pn-junction is 100 GHz at 0 V bias voltage.
In addition to the theoretical RC model of the pn-junction of the modulator, the characterization of the modulator including the metal lines can be realized by means of an equivalent circuit model. This is realized in chapter 3.4.4 for the fabricated structure based on the measurement results of the device.

3.4 Fabricated structures and measurement results

Different designs of modulators together with diverse optical and electrical test structures are fabricated at IMS CHIPS using an SOI wafer flow process [60]. A microscopic picture of the fabricated die is presented in Figure 3.22. For the fabrication of the modulator the following 9 masks are used:

- 250 nm Si etching (for the definition of the waveguides).

- 70 nm Si etching (for the GC grooves).
- 200 nm − 170 nm silicon etching (slab definition of the modulator).
- Aluminum layer (definition of the metal lines on top of the SiO_2 passivation, i.e. TLs and TWEs).
- p-doped Si region (for the pn-junction of the modulator).
- n-doped Si region (for the pn-junction of the modulator).
- p^+-doped Si region (for the Si contact with the metal vias).
- n^+-doped Si region (for the Si contact with the metal vias).
- 1 µm SiO_2 passivation etching (for the Al vias contact).

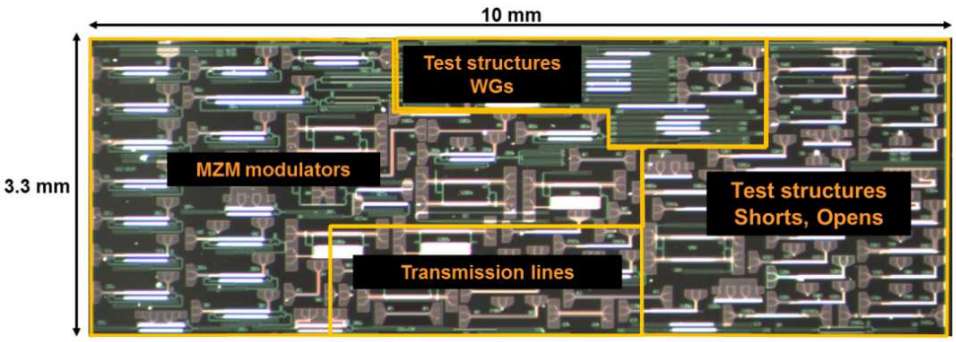

Figure 3.22: Micrograph of the fabricated die with the IMS CHIPS technology

3.4.1 Optical and electrical test structures

3.4.1.1 Optical waveguides

An example of some of the optical test structures is illustrated in Figure 3.23(a-b). In order to calculate the losses of the GCs and intrinsic monomode waveguides, different test structures are fabricated.
First, the transmission of two identical GCs linked by a strip waveguide with the same width as the gratings, i.e. 15 µm width, is measured. The losses due to this wide waveguide are negligible. This structure is used as reference for the measurement of the losses of the other optical test structures. Figure 3.23(c) shows the measurement results of

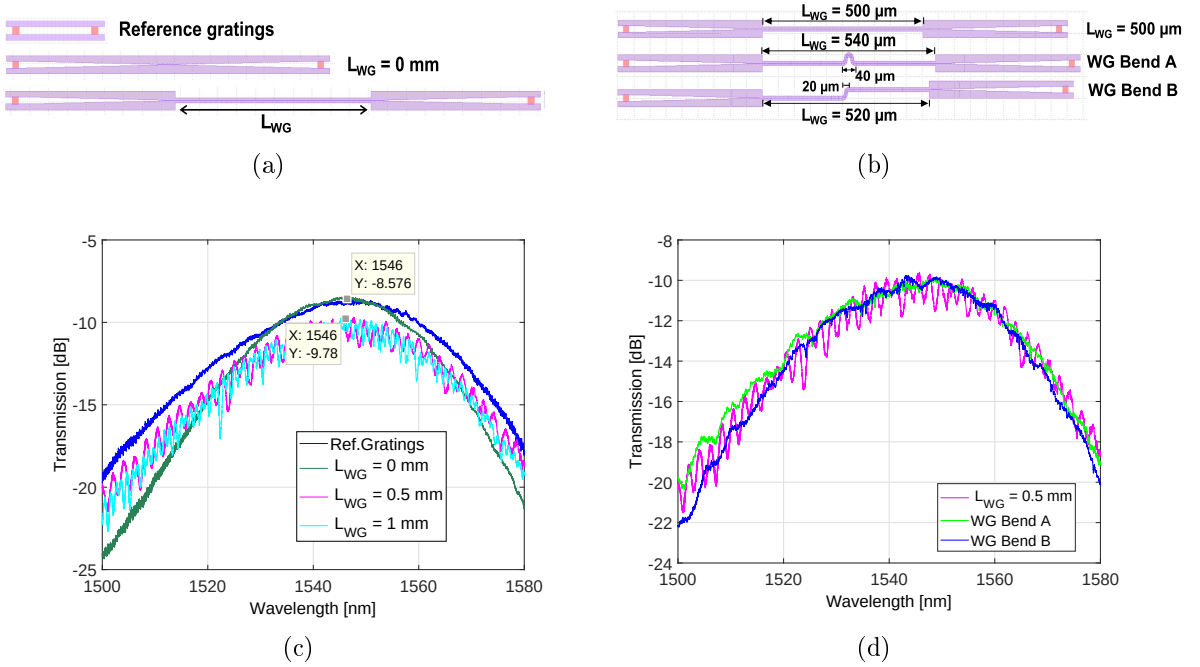

Figure 3.23: (a-b) Layout of some of the optical test structures. (c) Measurement results of the presented waveguides in "(a)" for different waveguide lengths L_{WG}. (d) Measurement results of the waveguides shown in "(b)".

the structures depicted in Figure 3.23(a). The maximum coupling efficiency of the two reference gratings is $-8.58\,\mathrm{dB}$ at the wavelength $\lambda = 1546\,\mathrm{nm}$.

Afterwards, the same measurements are realized for structures where the GCs are followed by adiabatic tapers. These are connected by a monomode strip waveguide with the length L_{WG} and a width of 400 nm. The structure with $L_{\mathrm{WG}} = 0$ is the degenerate case without monomode waveguide. It has a similar maximum transmission as the reference grating, but a lower bandwidth. For the cases with $L_{\mathrm{WG}} > 0$, the bandwidth is comparable to that of the reference gratings, but the maximum transmission is reduced. This is mainly due to the loss at the transition between the taper and the monomode waveguide and to a lesser extend due to the intrinsic waveguide loss. The measurements of these monomode waveguides show periodical ripples. The ripple period of the waveguide with $L_{\mathrm{WG}} = 1\,\mathrm{mm}$ is approximately the half of that of the waveguide with $L_{\mathrm{WG}} = 500\,\mu\mathrm{m}$. This may be caused by imperfections in the fabrication process. The strip waveguide is monomode for a height of 250 nm and a width of 400 nm. For larger waveguides, the second mode can propagate and this can cause interference with the fundamental mode. This explains the reproducible maximums and minimums of the two curves. This effect is further investigated with other test waveguides: a waveguide with a 180 ° bend and a waveguide

with an s-shaped bend as shown in Figure 3.23(b). The measurement results are compared to the straight waveguide transmission with a length $L_{\mathrm{WG}} = 500\,\mu\mathrm{m}$ in Figure 3.23(d). The transmission curves of the bent waveguides are smoother than those of the straight waveguide. This confirms the assumption of the multimode propagation, since the second order mode propagation is extremely weakened by the use of bends with a small radius. The same design of the test waveguides is fabricated in a later tape-out using the same technology. The new measurements of the 400 nm width waveguides show a smooth transmission. Therefore, due to an inaccuracy in the etching process of the fabricated die, wider waveguides as the target design are obtained. Some pictures of the fabricated structures are shown in Figure A.1 of Appendix A, where a width of about 414 nm for the strip waveguide is measured.

The losses due to the doping of the waveguides are investigated analyzing the transmission spectrum of differently doped test structures. These structures are identical to the straight waveguide shown in Figure 3.23(b) with a length of $L_{\mathrm{WG}} = 500\,\mu\mathrm{m}$, but instead of the strip intrinsic monomode waveguide, a rib doped waveguide is added.

Figure 3.24(a) shows the cross section of the doped waveguides. The width of the core is 400 nm and the slabs have a width of $s = 0.55\,\mu\mathrm{m}$ for the test waveguides measured in Figure 3.24(b) and $s = 0.7\,\mu\mathrm{m}$ for the ones measured in Figure 3.24(c). The plots show the optical transmission depending on the wavelength of a waveguide with a pn-, n- and p-doped core. The contact regions are always highly doped, i.e. p^+ or n^+, with a carrier concentration of about $1 \cdot 10^{20}\,\mathrm{cm}^{-3}$, respectively. The p- and n-doping target is $N_{\mathrm{a}} = N_{\mathrm{d}} = 1 \cdot 10^{17}\,\mathrm{cm}^{-3}$. The slabs are completely p- or n-doped, i.e. $s = s_{\mathrm{n,p}}$, except the waveguide measured in Figure 3.24(c) defined as p (slab $= 0.7\,\mu\mathrm{m}$) $\mathrm{p}^+(0.4\,\mu\mathrm{m})$, where $s = 0.7\,\mu\mathrm{m}$ and the lowly doped Si region is $s_{\mathrm{n,p}} = 0.4\,\mu\mathrm{m}$ from the core edge. The measurement results are compared with the intrinsic strip waveguide defined as $L_{\mathrm{WG}} = 0.5\,\mathrm{mm}$.

It is observed that the ripples disappear for all the doped test structures. As mentioned before, in case of fabrication irregularities the second order modes can weakly propagate. However, a significant part of the second order mode propagates where the density of free carriers is high. The free carriers lead to losses and attenuate the second and higher order modes effectively. In addition, the second order modes have a bigger portion of the E-field extended along the slabs where the absorption is higher due to the highly doped regions and the proximity to the metal.

In Figure 3.24(b), the pn-doped curve shows approximately the same transmission as the ripple maximums of the intrinsic waveguide along the measured spectrum. This means

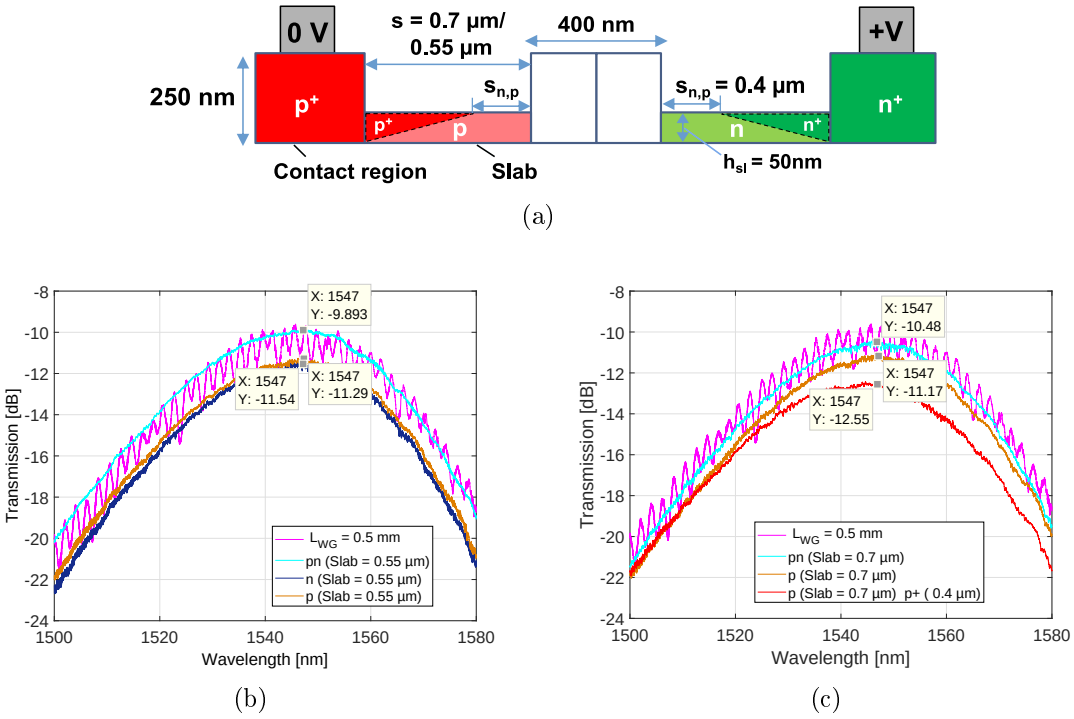

Figure 3.24: (a) Cross section of the doping profile and dimensions of the test doped waveguides. Measurement results of the doped waveguides with different profiles with a slab width of (b) $s = 0.55\,\mu\text{m}$ and (c) $s = 0.7\,\mu\text{m}$.

that the core is probably undoped, since a core width of only 400 nm is very sensitive to possible misalignment of the two doping masks (p and n) during fabrication. Based on these fabricated test structures and the measurement results, the parameters for a future design kit on this technology can be adjusted, limiting the minimum doping mask width to avoid undoped regions. For the case of the p- and n-doped core waveguide with a 0.55 µm slab, the loss compared to the pn-structure, assumed as undoped core, are 3 dB/mm and 3.5 dB/mm, respectively.

In Figure 3.24(c), some absorption is observed for the pn-structure. Measurements show almost 1.2 dB/mm more losses than for the pn-structure of Figure 3.24(b). This means that a higher free carrier concentration is present in the core, where the propagating fundamental mode is confined. The losses for the p-doped core waveguide are higher than those for the pn-doped, since the depletion region of the p-doped core is near the edge of the core instead of in the middle. The optical absorption of the fundamental mode is higher because the optical wave overlaps with a larger area with free carriers in comparison to the pn-structure. This is in good agreement with the simulations. Finally, if the p^+- and n^+-regions are placed at a shorter distance $s_{n,p} = 0.4\,\mu\text{m}$ from the core

edge, the absorption of the light increases by 2.8 dB/mm at the maximum transmission wavelength in comparison to the distance $s_{n,p} = 0.7\,\mu m$.

3.4.1.2 Electrical transimission lines

For the study of the TWE of the modulator, electrical test structures with different dimensions are designed and fabricated. Coplanar transmission lines without a pn-junction underneath are characterized.

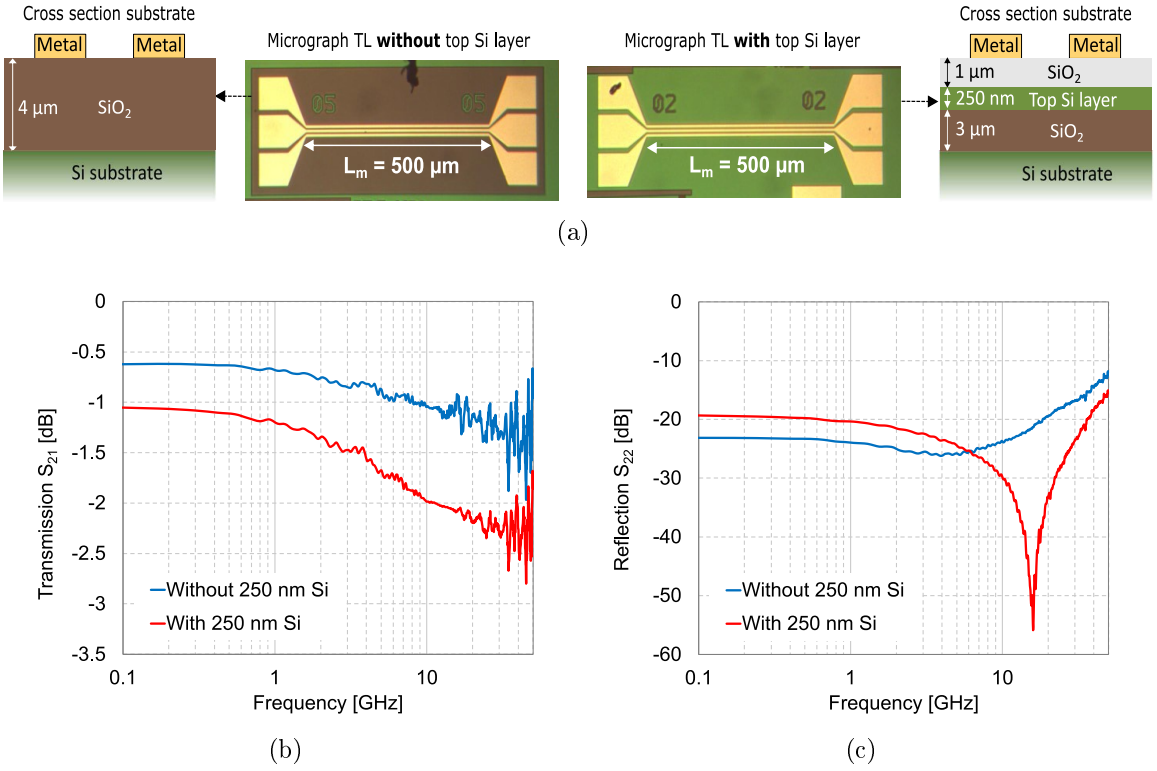

Figure 3.25: (a) Micrograph of the TLs without the top Si (SiO_2 only, brown area) under the metal lines (left) and with the top Si under the lines (green color). (b-c) Measurement results of the transmission and reflection of the TLs shown in "(a)".

The effect of the top silicon layer on the transmission of the electrical RF signal is measured. Two coplanar transmission lines with a length of $L_m = 500\,\mu m$ are designed with and without the 250 nm Si thickness layer of the substrate. The metal pads and tapers are designed to contact commercial ground-signal-ground (GSG) RF probes with a pitch of 100 µm. A microscopic picture of the two TLs and the cross section of the substrate are presented in Figure 3.25(a). The measurement results of the transmission and reflection of both structures are plotted in Figure 3.25(b-c) for the frequency range from 0.1 GHz to

50 GHz. The loss of the TL with the top Si layer is twice as high in dB than that of the TL without Si layer. The performance of the TLs are more efficient at high frequencies if the metal lines are electrically well isolated. The resistivity of the intrinsic Si is specified for the used SOITEC wafer as $\rho_{\mathrm{Si}} \approx 20\,\Omega\mathrm{cm}$ while the resistivity of the SiO_2 layer should be significantly higher. The results of the measurements show an electrical loss lower than 2.4 dB/mm up to 20 GHz without the top Si layer.

To analyze the loss of the TL per unit length, test structures with different lengths are fabricated. The layout of these structures is shown in Figure 3.26(a). The lines have a width of $W_{\mathrm{m}} = 7.9\,\mu\mathrm{m}$ and a space between the lines of $s_{\mathrm{m}} = 2.2\,\mu\mathrm{m}$. The measurement results of the transmission and reflection of the structures shown in Figure 3.26(a) are presented in Figure 3.26(b-c). The reference test structure with only pads and tapers exhibits around 0.6 dB loss at 50 GHz due to the reflections between probes and pads and due to the taper loss. The TL loss per unit length has a frequency-dependent performance. This is approximately 3 dB/mm for frequencies at 30 GHz. For frequencies lower than 3 GHz, the transmission and reflection are very similar for $L_{\mathrm{m}} = 500\,\mu\mathrm{m}$ and $L_{\mathrm{m}} = 1\,\mathrm{mm}$, showing an additional loss of around 0.9 dB to 1.2 dB for both TL lengths with respect to the structure with only pads and tapers.

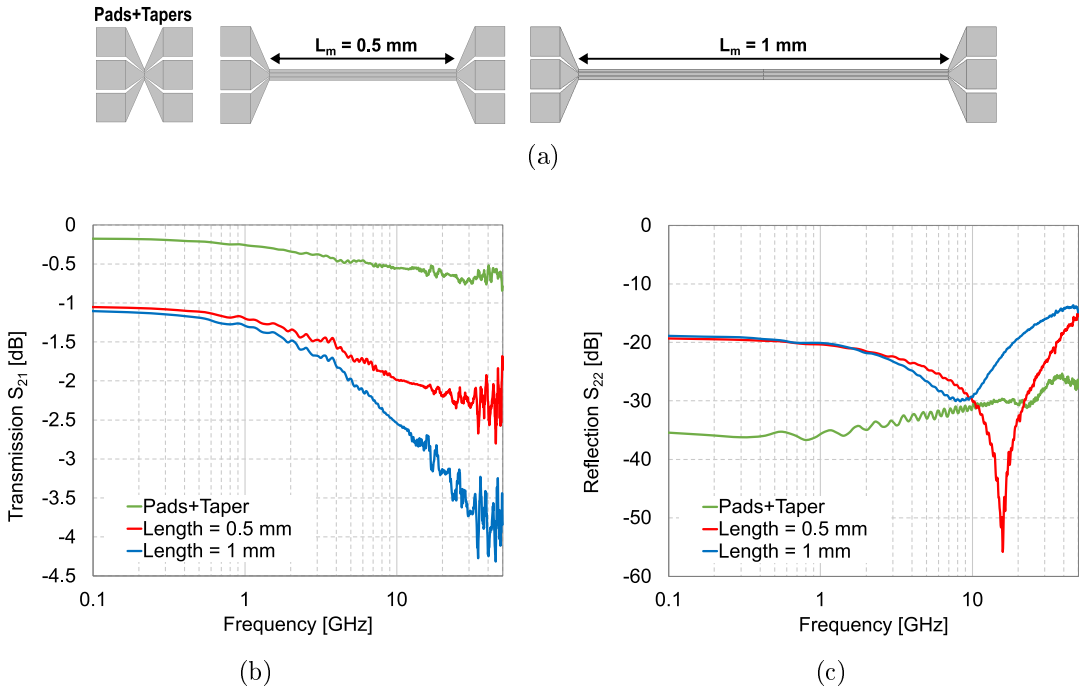

Figure 3.26: (a) Layout and measurement results of the (b) transmission and of the (c) reflection of the TLs with different lengths.

In addition to the straight metal lines, TLs with an L-shape are also analyzed. The main reason for the use of this shape in the designs of this work is to reduce complexity in the measurement setup. For some of the modulator measurements, it is necessary to contact the die on a very small area with two RF probes and with two tilted optical fibers (see chapter 3.4.3). For some designs, the distance between the metal contact pads and the GC is less than 200 µm. Therefore, the L-shape is used in most of the TWE designs of the fabricated die in order to have enough space for the positioning of the RF probes and the fibers.

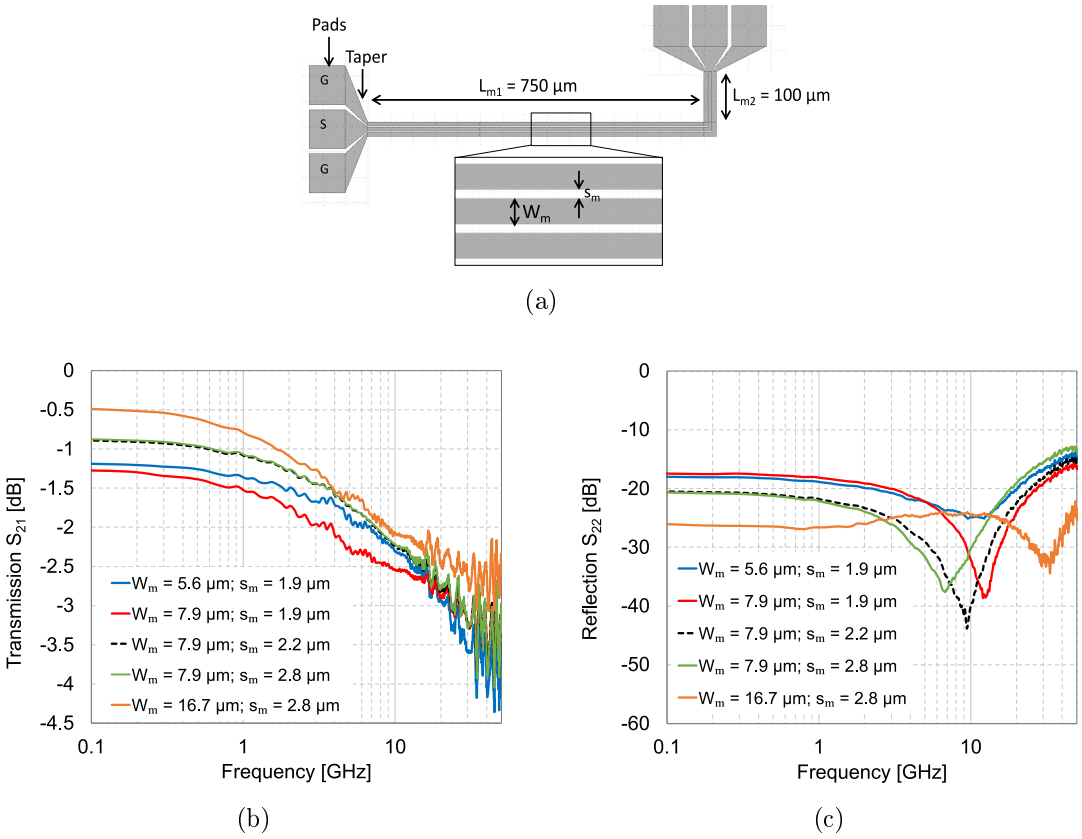

Figure 3.27: (a) Layout of the L-shaped coplanar transmission line. Measurement of the (b) transmission and (c) reflection of the L-shaped TLs with different widths W_m and spaces s_m between the lines.

A description of the dimensions of the L-shaped coplanar lines is presented in Figure 3.27(a). Pads and tapers have the same dimensions as the straight TLs described above. A first calculation of the optimal coplanar TL dimensions is done with the simulation tool LineCalc of ADS. The resulting dimensions of the simulations are taken as a reference for the TL design. Different designs are fabricated varying the parameters of the width W_m of the

metal lines and the space s_m between them. The measurements of the transmission and the reflection of these L-shaped coplanar lines are plotted in Figure 3.27(b-c). The design of the modulator and especially the width of the Si waveguide slab s, that connects the waveguide core with the Si contact region, leads to the need of limiting the space s_m between the metal lines. To maximize the depletion effect and to reduce the electrical resistance, the distance between the metal vias and the contact Si region should be small. However, a short distance also leads to high light loss. A good compromise is keeping the distance s_m lower than 3 µm. With a line width of $W_\mathrm{m} = 16.7\,\mu\mathrm{m}$ and a distance $s_\mathrm{m} = 2.8\,\mu\mathrm{m}$, the electrical loss of the TL at 50 GHz is less than 3.2 dB and around 0.5 dB at low frequencies. For the other RF lines, lower values for W_m and s_m are chosen. The losses of these lines are generally higher. Nevertheless, all of them have a 3 dB-bandwidth greater than 50 GHz. The reflections of all the designed TLs are lower than −12 dB up to 50 GHz. In chapter 3.4.2 a fabricated modulator is presented whose TWE dimensions are $W_\mathrm{m} = 7.9\,\mu\mathrm{m}$ and $s_\mathrm{m} = 2.2\,\mu\mathrm{m}$.

After the fabrication and measurement of the structures, the results are compared with the simulations realized with the tool Momentum of ADS in order to verify and characterize the TLs. First, the resistivity of the materials used in the substrate is analyzed. The simulations and the measurements show a similar performance for the structure shown in Figure 3.25 without the top Si layer when the resistivity of the silicon substrate has the nominal value of $\rho_\mathrm{Si} = 20\,\Omega\mathrm{cm}$. The results of the electrical transmission and reflection are presented in Figure 3.28(top). For the TLs with the top Si layer, the simulations do not match with the measurements if the resistivity of the Si, i.e. top Si layer and substrate, is $\rho_\mathrm{Si} = 20\,\Omega\mathrm{cm}$. The measurement setup does not allow to measure the resistivity directly. Therefore, a simulation sweep is done with resistivity as sweep parameter. For a resistivity of $\rho_\mathrm{Si} = 6\,\Omega\mathrm{cm}$, the simulation matches better with the measurement results (Figure 3.28(bottom)). The simulation uses a mesh with 500 cells/wavelength. This is a good compromise between accuracy and compute time. The reduction of the resistivity with respect to the wafer specifications is probably due to the doping process of the modulators included in the die. This could also affect the properties of the undoped regions.

Furthermore, the L-shaped TLs are also verified with simulations. The results for the structure with $W_\mathrm{m} = 7.9\,\mu\mathrm{m}$ and $s_\mathrm{m} = 2.2\,\mu\mathrm{m}$, defined as TL-A for simplification, are presented in Figure 3.29(top). The results for the TL with $W_\mathrm{m} = 16.7\,\mu\mathrm{m}$ and $s_\mathrm{m} = 2.8\,\mu\mathrm{m}$, defined as TL-B, are shown in Figure 3.29(bottom). These simulations are realized with two parameter sweeps: the resistivity of the top Si layer and the resistivity of the Si sub-

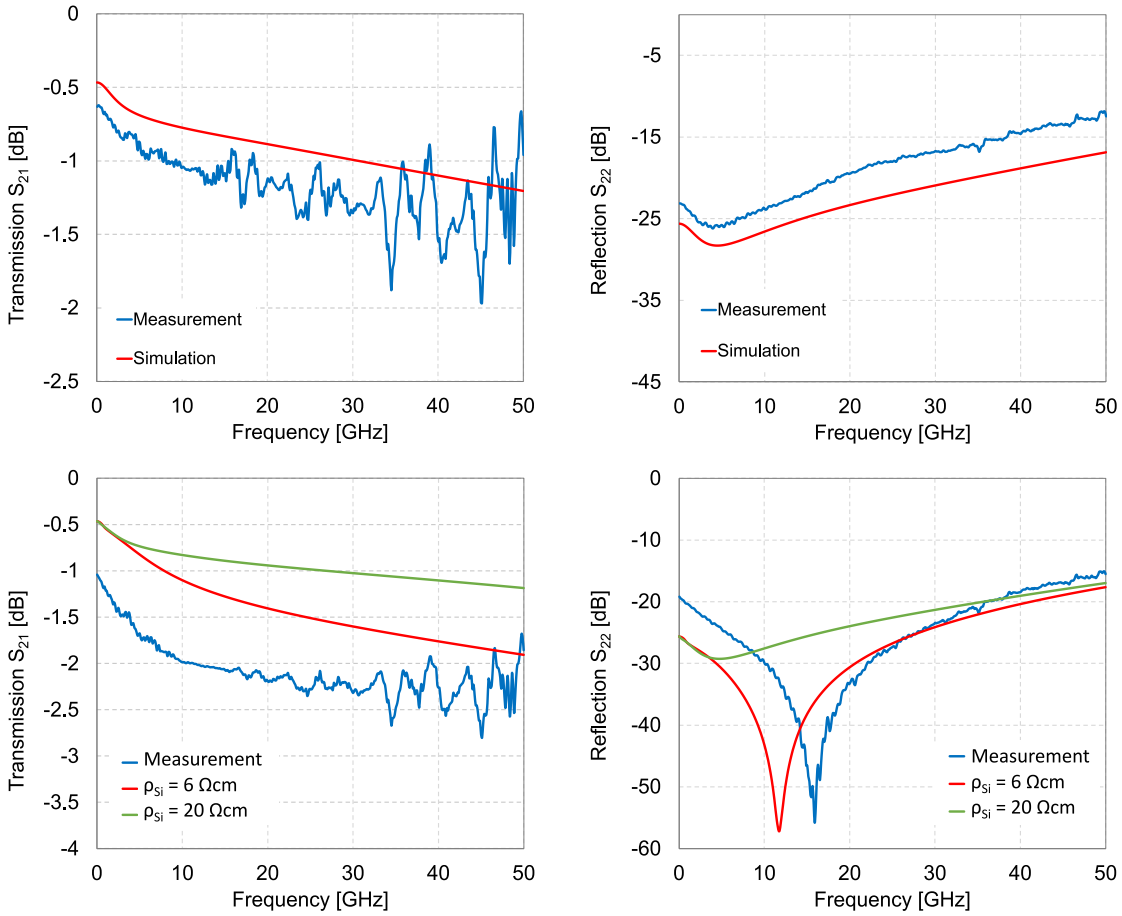

Figure 3.28: Comparison between simulations and measurements of the electrical transmission and reflection of the straight TLs with $W_\mathrm{m} = 7.9\,\mu\mathrm{m}$, $s_\mathrm{m} = 2.2\,\mu\mathrm{m}$ and $L_\mathrm{m} = 500\,\mu\mathrm{m}$. Top: TL without the top Si layer simulated with $\rho_\mathrm{Si} = 20\,\Omega\mathrm{cm}$ for the Si substrate. Bottom: TL with the top Si layer. The TL is simulated with the resistivity of the top Si layer and substrate $\rho_\mathrm{Si} = 20\,\Omega\mathrm{cm}$ and with $\rho_\mathrm{Si} = 6\,\Omega\mathrm{cm}$.

strate. The resistivity of the substrate is defined as ρ_sub, the resistivity of the top silicon layer is defined as ρ_top. For both structures, it is observed that along the complete measured frequency bandwidth the measurements are similar to the simulation results when both the resistivity of the top Si and the substrate are $\rho_\mathrm{top} = \rho_\mathrm{sub} = 6\,\Omega\mathrm{cm}$. Therefore, this value is assumed in the following simulations of the TLs.

Finally, the effect of the metal thickness in the transmission and the reflection of the RF signal is investigated. The metal thickness of the structures fabricated at IMS CHIPS is $T = 0.5\,\mu\mathrm{m}$. The two L-shaped TLs, TL-A and TL-B, are simulated with metal thicknesses T of $0.5\,\mu\mathrm{m}$, $1\,\mu\mathrm{m}$, $3\,\mu\mathrm{m}$ and $5\,\mu\mathrm{m}$.

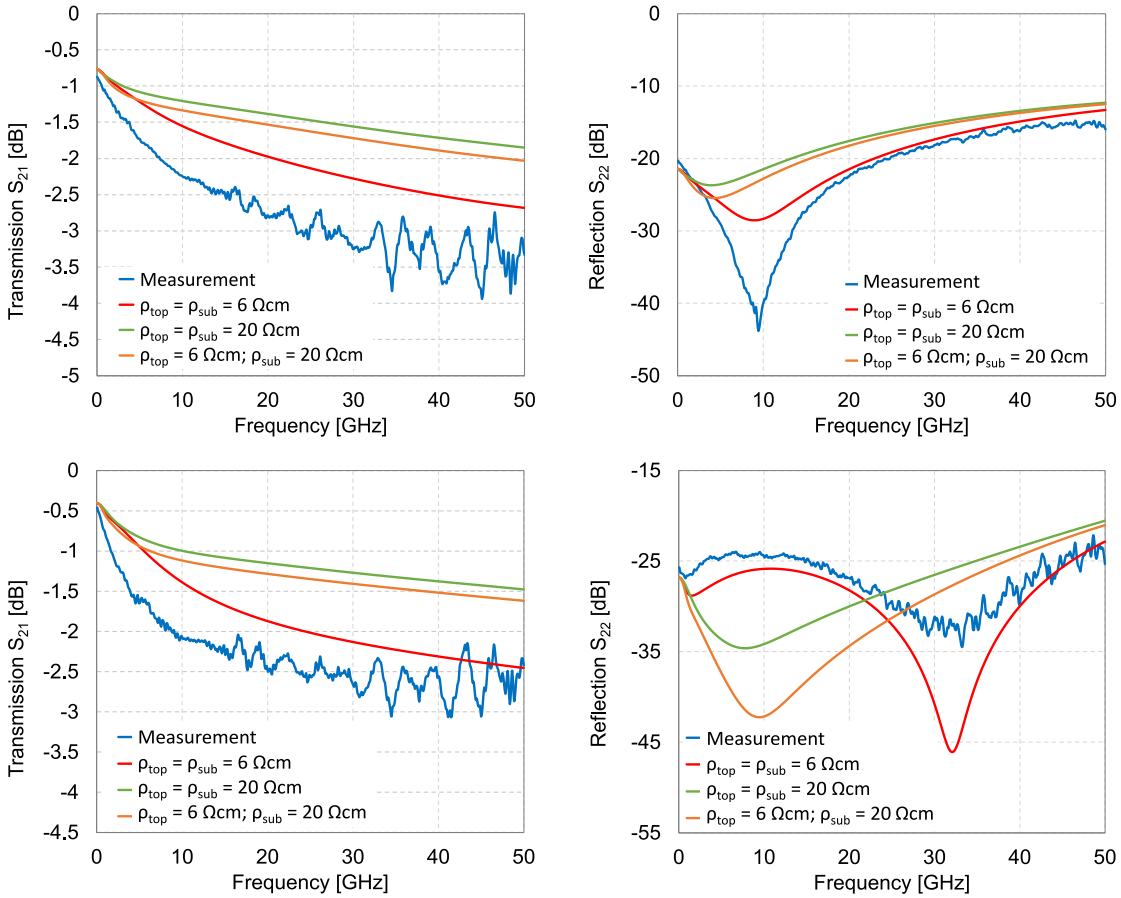

Figure 3.29: Comparison between simulation and measurement of the transmission and reflection of the L-shaped TLs for different ρ_{top} and ρ_{sub}. Top: TL-A with $W_{\text{m}} = 7.9\,\mu\text{m}$ and $s_{\text{m}} = 2.2\,\mu\text{m}$. Bottom: TL-B with $W_{\text{m}} = 16.7\,\mu\text{m}$ and $s_{\text{m}} = 2.8\,\mu\text{m}$.

The simulation results of the TL-A are plotted in Figure 3.30(top). When the thickness of the metal is increased from 0.5 µm to 1 µm, the transmission loss is reduced by around 0.4 dB at low frequencies and by 0.5 dB at 50 GHz. If the metal thickness is increased to 3 µm, the transmission loss can be reduced by around 0.7 dB at low frequencies and by 1 dB at 50 GHz. However, the reflection for $T = 3\,\mu\text{m}$ is higher than that for the lower thicknesses for some frequencies, since the minimum of the curve is shifted to lower frequencies. Nevertheless, the reflection is kept below −20 dB for the complete simulated bandwidth. For the case of $T = 5\,\mu\text{m}$, the transmission is similar than the one for $T = 3\,\mu\text{m}$. However, the reflection is higher. The positive effect on the transmission of a thicker metal starts to converge to an optimum thickness around $T = 3\,\mu\text{m}$.

For the TL-B, the comparison between the measured structure with $T = 0.5\,\mu\text{m}$ and the

simulations is shown in Figure 3.30(bottom). The increase of the metal thickness from 0.5 µm to 1 µm reduces the transmission loss by around 1 dB at 20 GHz and by around 1.5 dB at 50 GHz. Furthermore, the reflection is reduced and kept below −25 dB for all of the simulated frequencies. For this structure, the optimization of $T = 1\,\mu m$ seems to be a good compromise between transmission loss and reflection. For thicker metal, the transmission converges to similar values of the transmission as $T = 1\,\mu m$, but the reflection of the lines increases.

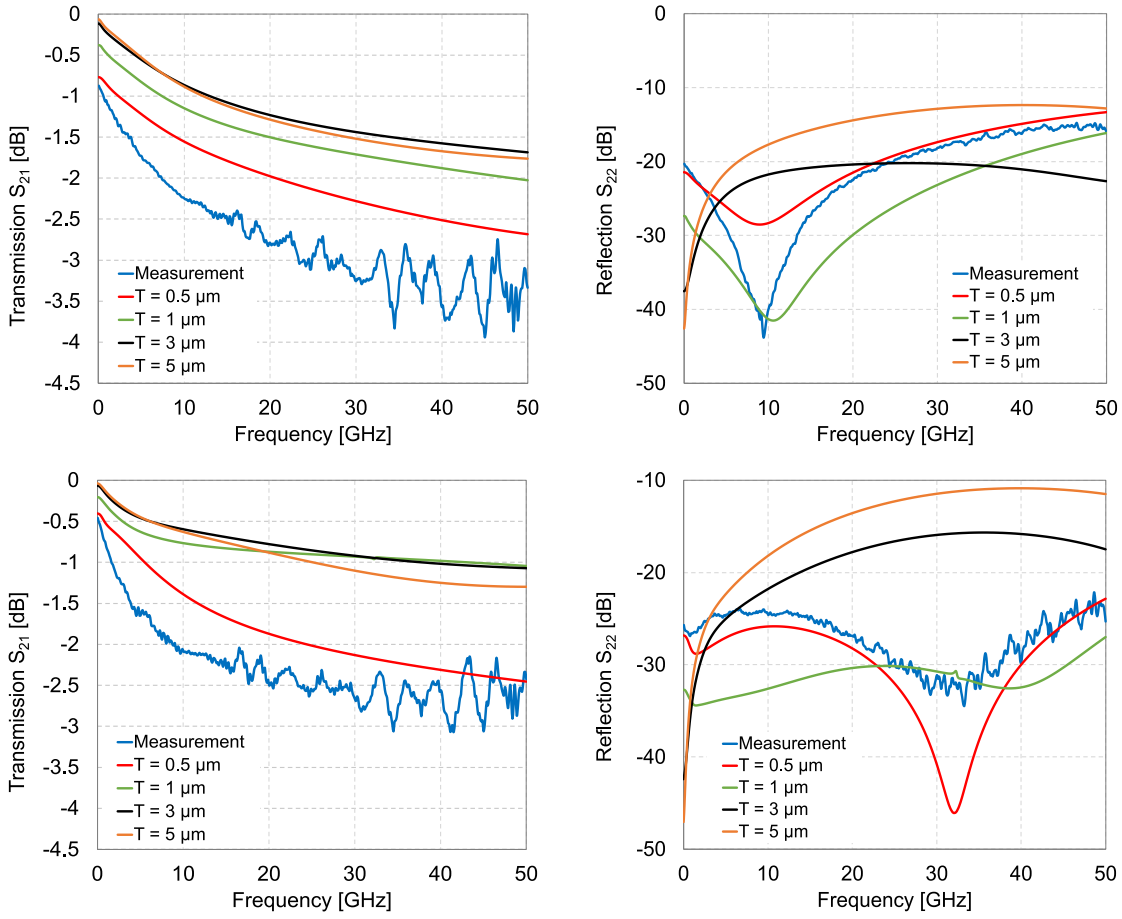

Figure 3.30: Simulation of different metal thicknesses T of the L-shaped TLs and comparison with the measurement for $T = 0.5\,\mu m$ of the TL-A (top) and TL-B (bottom).

3.4.2 Characterization of the modulator

This chapter presents the measurement results of the first optical modulator fabricated at IMS CHIPS. The device is fabricated as a prototype to prove the functionality of the novel

technology. The layout and micrograph of the complete MZM is shown in Figure 3.31. The TWE of the modulator has an L-shape with $W_{\mathrm{m}} = 7.9\,\mu\mathrm{m}$ and $s_{\mathrm{m}} = 2.2\,\mu\mathrm{m}$, i.e. the same dimensions as the TL-A. For simplification, this modulator is denominated Modulator A. The phase shifter has the length $L_{\mathrm{ph}} = 500\,\mu\mathrm{m}$. The modulator is based on the p-doped core configuration since the rib doped waveguide of the phase shifter has a core width of only 400 nm. Doping masks that do not align well during fabrication can lead to a wide undoped region in the core that reduces the performance of the modulator significantly. A scheme of the cross section of the phase modulator showing the dimensions and doping regions is presented in Figure 3.32.

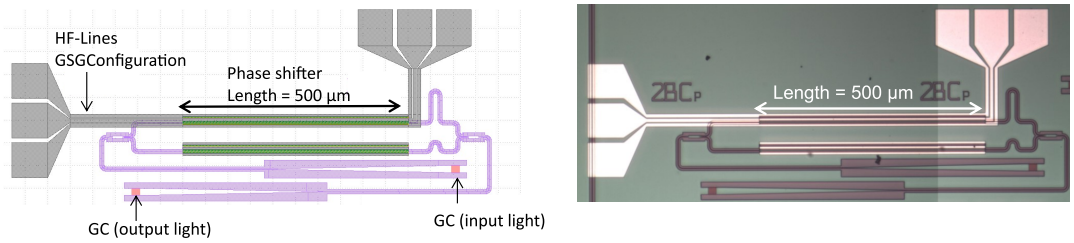

(a) (b)

Figure 3.31: (a) Layout of the Modulator A, an MZM with a phase shifter length of 500 µm, (b) MZM micrograph.

The target doping concentrations in the p- and n-doped regions are $1 \cdot 10^{17}\,\mathrm{cm}^{-3}$. In this design, the distances $s = 0.7\,\mu\mathrm{m}$ and $s_{\mathrm{n,p}} = 0.4\,\mu\mathrm{m}$ are smaller and the slab thickness $h_{\mathrm{sl}} = 80\,\mathrm{nm}$ is higher than in the optimized design for light loss shown in the previous simulations (Figure 3.16). Therefore, higher optical loss is expected for this device (see Figure 3.14(c)).

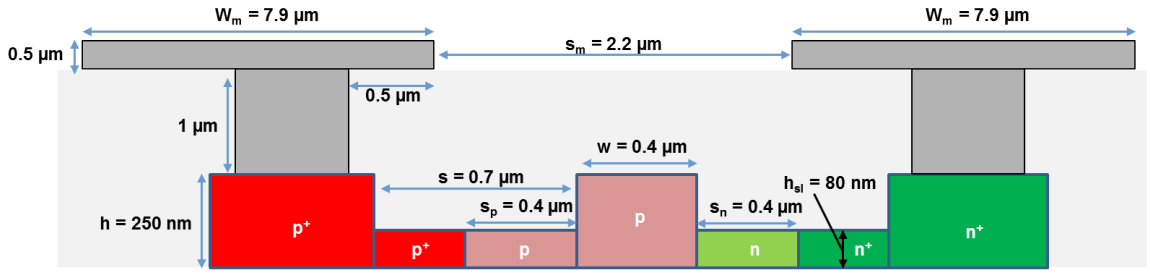

Figure 3.32: Cross section of the phase shifter of the fabricated MZM.

The optical transmission spectrum of the modulator is measured for different reverse bias voltages. The results are plotted in Figure 3.33. The passive ER is around 32 dB. The fiber-to-fiber insertion loss (IL) of the MZM, including the losses of the GCs, tapers,

MMIs, delay lines and waveguides, is 12.5 dB at $\lambda = 1550$ nm. The GCs used for this design are standard, therefore the total IL could be reduced by using the highly efficient coupler, which exhibits a coupling efficiency of -0.74 dB at $\lambda = 1550$ nm, demonstrated in [8] for the same technology. The total loss of the modulator can be reduced by approximately 6 dB. The IL only for the on-chip MZM is 4.2 dB for 0 V bias voltage, i.e. for the maximum absorption of the light signal due to the free carriers. The loss per unit length of the phase shifter is around 2 dB/mm. The measured modulation efficiency is $V_\pi L = 3.1$ Vcm at 2 V reverse bias voltage. The simulated modulation efficiency for this structure is $V_\pi L = 2.87$ Vcm with a loss of 1 dB/mm. As it was previously observed with the measurements of the optical test structures, this mismatch can be caused by misalignment of the doping masks and irregularities during the Si etching process as shown in Appendix A. For verification, the same simulations are realized with a horizontal shift of about 150 nm for the highly doped regions. These simulations match well with the measurements.

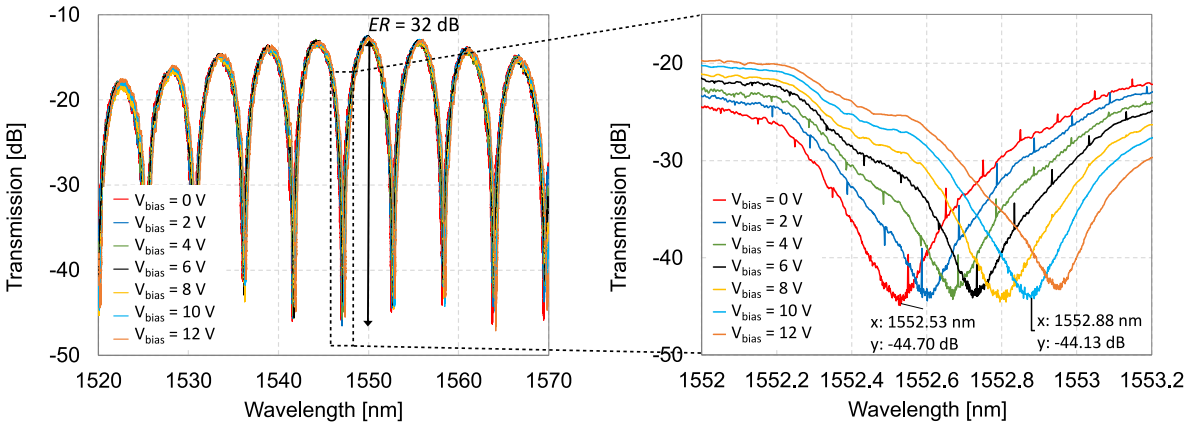

Figure 3.33: Measurement for different reverse bias voltages of the optical transmission of the MZM. Zoom: wavelength shift depending on the reverse bias voltage.

The frequency response of the MZM is characterized. RF measurements of the TWE of the modulator are realized for different bias voltages. In Figure 3.34, the results are compared with the TL with the same dimensions but without the doped etched waveguides under the metal lines. The TL shows a similar transmission than the TWE of the optical modulator. The main difference is the resonance of the TWE at around 30 GHz. The doped silicon rib waveguide used to modulate the light works as a diode. By increasing the reverse bias voltage, the depletion region of the pn-junction becomes wider. Consequently, the variable junction capacitance decreases and the electrical transmission of the modulator improves. As shown in Figure 3.35(a), there is a section where the coplanar metal lines are symmetric

(cross section 1) without an optical waveguide underneath. However, the phase shifter region has an asymmetric configuration (cross section 2), because of the diode under the lines. This transition favors the electrical mode conversion of the coplanar waveguide mode to the unwanted coupled-slotline mode. This also explains that the measurements of the TL structures in chapter 3.4.1.2 do not show the resonance: the coplanar lines are symmetric for the complete TL structure because no optical waveguide is present under the lines. To suppress the coupled-slotline mode, air-bridges could be used to flatten the frequency response curve and therefore increase the bandwidth as described by [61][62]. Therefore, the cut-off frequency of the modulator could be improved if this undesired effect is diminished. It has to be considered that the small dimensions of the ground metal lines, smaller than 8 µm could complicate the use of bond wires to minimize this effect. Nevertheless, in future designs this fact should be taken into account to avoid undesirable effects using symmetric coplanar TWE as presented in Figure 3.35(b).

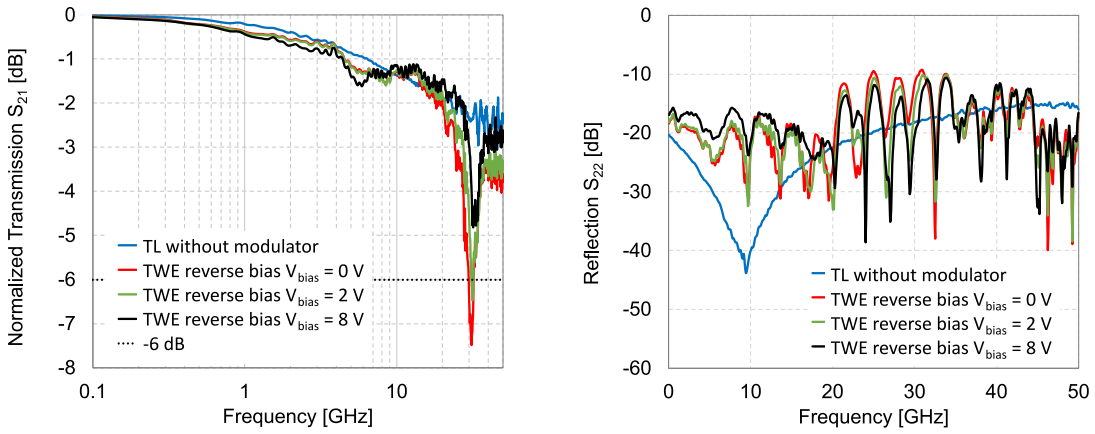

Figure 3.34: Measurement results: (a) transmission and (b) reflection of the TWE of the modulator for different reverse bias voltages and comparison with the measured TL with the same dimensions.

The 6 dB electrical bandwidth (accurately the 6.4 dB electrical bandwidth) of the TWE corresponds to the 3 dB EO bandwidth of the modulator assuming a match between the phase velocities of the driving electrical signal and the optical wave for a short phase shifter of 500 µm length. The 3 dB EO bandwidth corresponds to the frequency, for which the phase is reduced $\frac{1}{\sqrt{2}}$ of the reference level. This causes a 3 dB fall in the received optical signal, corresponding to the electrical loss of 6 dB [63][64].

The 6 dB electrical bandwidth of the modulator for the voltage range from 0 V to 2 V is

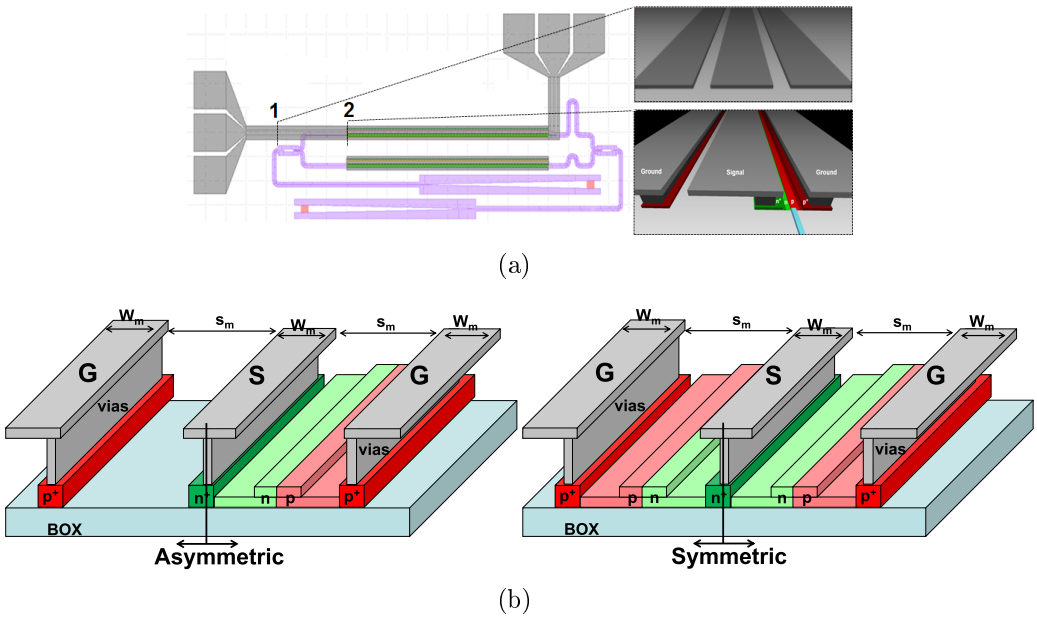

Figure 3.35: (a) Layout MZM. Cross section 1: Symmetric coplanar lines. Cross section 2: Start of the phase shifter, asymmetric coplanar lines, pn-waveguide (diode) under only one side of the metal lines. (b) Asymmetric and symmetric structure.

30 GHz. For a higher voltage of 8 V (black curve in Figure 3.34), a bandwidth higher than 50 GHz can be reached. The reflection of the TWE stays below −10 dB up to 50 GHz.

Different configurations and dimensions of the TWE are included on the die design. The optimized coplanar line with the dimensions $W_\mathrm{m} = 16.7\,\mu\mathrm{m}$ and $s_\mathrm{m} = 2.8\,\mu\mathrm{m}$ is fabricated as modulator. For simplification, this modulator is called Modulator B. The RF response of the TWE vs. the signal frequency is measured up to 50 GHz. Additionally, a different design of the TWE where the coplanar lines are straight to avoid the 90 °-bend is also measured. The dimension of the lines is $W_\mathrm{m} = 7.9\,\mu\mathrm{m}$ and $s_\mathrm{m} = 1.9\,\mu\mathrm{m}$. This modulator is called Modulator C. The most important dimensions and the measured 6 dB cut-off frequency of the Modulators A, B and C are compared in the table in Figure 3.36. Furthermore, the layouts of the Modulators B and C are depicted. The three modulators have a phase shifter length of $L_\mathrm{ph} = 500\,\mu\mathrm{m}$.

The total length of the RF lines L_m is the Manhattan distance between the metal tapers. For the modulators with the L-shape, the length is $L_\mathrm{m} = 850\,\mu\mathrm{m}$. Precisely, this is 750 µm from the left metal taper to the bend and 100 µm from the bend to the top metal taper. For the case of the Modulator C the total length is $L_\mathrm{m} = 1\,\mathrm{mm}$. More space is required to contact the fibers and the RF probes. That leads to a longer RF line for Modulator C. The

	Modulator A	Modulator B	Modulator C
L_{ph}	500 µm	500 µm	500 µm
L_m	750 µm + 100 µm	750 µm + 100 µm	1 mm
W_m	7.9 µm	16.7 µm	7.9 µm
s_m	2.2 µm	2.8 µm	1.9 µm
6 dB cut-off frequency	V_{bias} = 0 V	V_{bias} = 0 V	V_{bias} = 0 V
	30 GHz	>50 GHz	>50 GHz

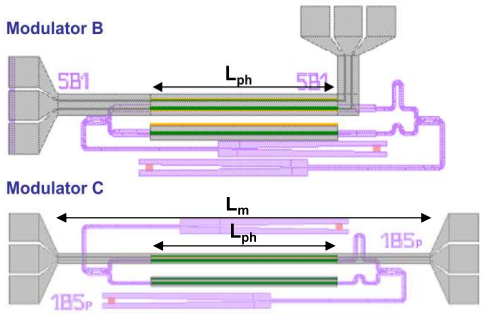

Figure 3.36: Comparison table of the measured modulators (left). Layout of the Modulator B and Modulator C (right).

6 dB cut-off frequency of the Modulator A is 30 GHz. The new designs of the Modulator B and Modulator C exhibit better performance of the TWE, since the resonance at 30 GHz is diminished. For both designs, the bandwidth is higher than 50 GHz. The measured frequency response of these modulators is shown in Figure 3.37. The reflection is lower than −9 dB and −19 dB up to 50 GHz for the Modulator B and C, respectively. The design without the 90 °-bend of the metal lines (Modulator C) shows lower losses of both the transmission and the reflection. But, it has to be considered that a significant complexity for the positioning of the fibers and probes is thereby added. In order to measure this kind of straight modulator, the measurement setup is modified to position the optical fibers and the RF probes in parallel at both sides of the probe station.

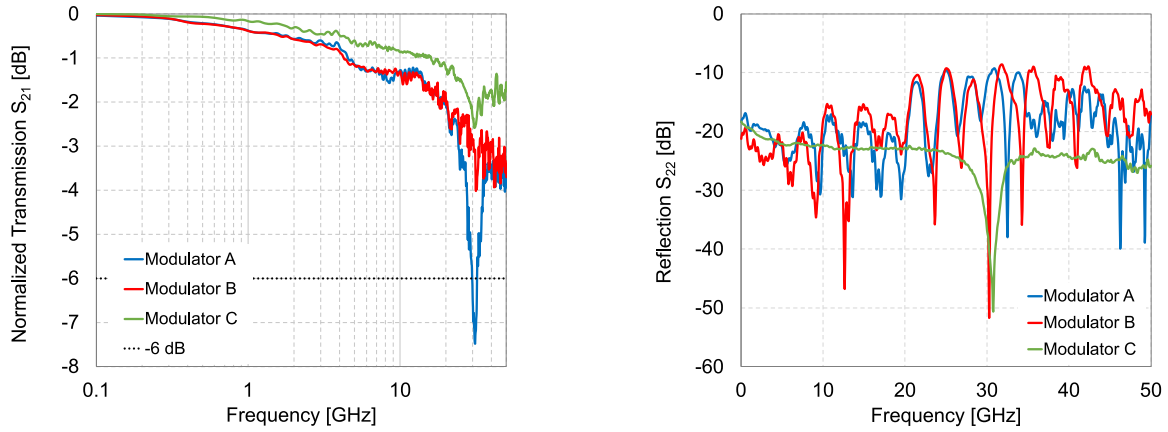

(a) (b)

Figure 3.37: Measurement results of the (a) transmission and (b) reflection vs. frequency for the Modulator A, B and C.

3.4.3 Measurement setup

The measurements of the optical response, of the electrical response, of eye diagrams and of the EO performance: all need a special measurement setup.
The optical response is measured for GC, waveguides, MMIs, tapers, bends and for the modulator itself. The measurement setup was introduced in Figure 2.25. In addition to the measurements in chapter 2.5.2, the setup allows to determine the optical loss of the doped waveguides. For this purpose, doped waveguides with different lengths and doping profiles are measured and the results are compared to a reference intrinsic waveguide as described in chapter 3.4.1.1.
Additionally, the optical transmission of the MZM for different applied bias voltages is measured. A DC-power supply connected to the coplanar metal pads of the TWE sets the bias voltage.
The measurement setup for the RF response is illustrated in Figure 3.38. It is composed of a vector network analyzer (VNA) with a frequency range between 0.5 GHz and 50 GHz. The S-parameters of the DUT are extracted and the RF performance of the modulator can be analyzed for different bias voltages. For the bias voltages, a broadband (65 GHz) bias-T is used. This component combines the RF signal from the VNA and the DC-voltage provided by a DC-power supply and sends it by means of a GSG broadband probe to the TWE of the embedded modulator. Two GSG probes are used for this measurement. One at the input and the other one at the output of the TWE. The probe at the output is connected using a broadband RF cable and a DC-block. The DC-block at the second port provides improved protection for the VNA.

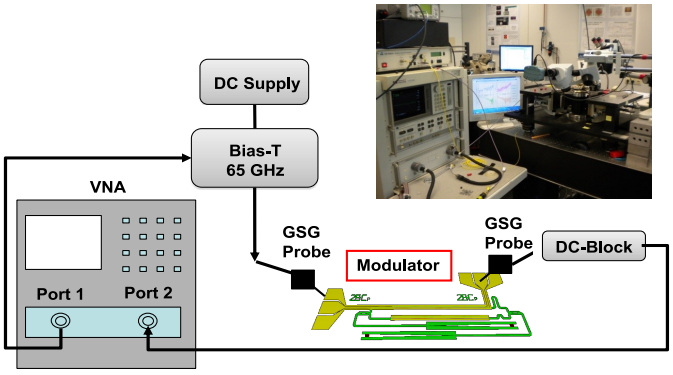

Figure 3.38: Measurement setup used for the characterization of RF response of the TWE of the modulator.

With the S-parameters, the transmission (S_{21}, S_{12}) and the reflection (S_{11}, S_{22}) of the DUT are characterized. The calibration of the setup is very important to get reliable

results. Hence, the complete setup is first calibrated using a calibration substrate where the GSG probes are contacted. The calibration substrate consists of short, open, 50 Ω-load and thru standard structures. Thereby, the effect of the setup components on the RF response of the modulator is removed.

For the measurement of eye diagrams, a modified setup depicted in Figure 3.39(a) is built. A bit pattern of 1010 is sent using a signal generator connected to a pulse pattern generator. The optical signal path is shown with a blue dotted line and the electrical signal path with a solid black line. The input optical signal is provided by a tunable laser and the polarization is set with a polarization controller. At the output of the modulator a 10 dB-coupler splits the modulated light in two paths, one to control the transmitted optical power, which is measured with the optical power meter. The other path is amplified by an erbium doped fiber amplifier (EDFA) and measured by a photodiode. The length of the modulator is very short, so the phase shift of the optical signal caused by the electrical signal is limited and the amplitude of the resulting optical modulated signal is small. Therefore, an electrical amplifier is also needed after the photodiode. Finally, the eye diagram of the modulator is measured by a sampling oscilloscope, which is triggered by the pulse pattern generator.

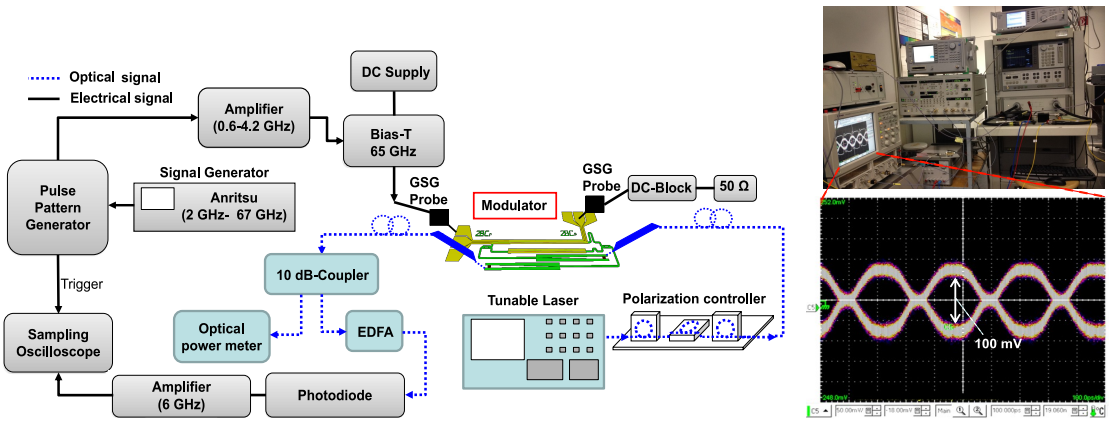

Figure 3.39: (a) Eye diagram measurement setup. (b) Picture of the setup used (top). Eye diagram measurement of the designed Modulator A (depicted in Figure 3.31) with a data rate of 4 Gbit/s for a bit pattern 1010 (bottom).

The measured eye diagram of the Modulator A (Figure 3.31) is shown in Figure 3.39(b). The working point of the modulator is at $\lambda = 1549.3\,\text{nm}$ with an applied reverse bias voltage of 8 V. Due to the limitation in the bandwidth of the amplifiers used in the setup, the measurements are realized at 4 Gbit/s. A picture of the setup is presented on top of

Figure 3.39(b).
For the characterization of the EO performance, the setup described in Figure 3.38 is extended and allows to measure optical response as well. The VNA provides an electrical sinusoidal signal. This signal is amplified and sent to the embedded modulator. The amplifier is necessary if the modulator dimensions are too short to achieve an optimal phase shift of the optical wave to reach a large amplitude modulation. The bias voltage is applied by a power supply by means of the bias-T device. At the output pads of the TWE a $50\,\Omega$ termination is connected in order to avoid undesired reflections of the electrical signal. For the optical path, a setup similar to the eye diagram setup is implemented. However, in this case the output of the photodiode is connected to the second port of the VNA. The broadband photodiode detects the amplitude modulated optical signal and converts it into an electrical signal. For this reason, the amplitude of the optical signal shall be large enough to be detected by the photodiode.
For the calibration of this setup, the RF response of the power amplifier and the bias-T is measured with the VNA. Afterwards, a heterodyne measurement setup is built to obtain the RF response of the photodiode as described in Appendix B. Finally, these calibration curves of the amplifier, bias-T and photodiode are subtracted from the measurement result of the EO response of the modulator. In Figure 3.40, a graphical representation of the described setup is illustrated and the measured results of the Modulator A are plotted. The transmission is very low, i.e. $< -42\,\mathrm{dB}$, since the responsivity of the photodector is not high enough to reach a higher electrical signal power range. For a reliable result, the length of the modulator should be longer or the two arms of the MZM could work as phase shifters in a push-pull configuration. Thereby, a higher amplitude of the optical signal and accordingly a stronger electrical signal from the photodiode could be achieved. Another factor to be considered is the bandwidth of the electrical amplifier $HP83020$. It is specified to operate only between 2 GHz and 26.5 GHz. The measured RF response of this amplifier together with the bias-T shows a nonuniform curve and high correction values for the frequency ranges from 2 GHz to 5 GHz and from 23 GHz to 26.5 GHz. Therefore, the estimation of the 3 dB EO bandwidth is with these results not reliable enough: at low frequencies, around 2 GHz, the transmission is lower than for higher frequencies. An amplifier with a wider and smoother broadband response is necessary to obtain significant results.
For future investigations, the same modulator can be fabricated with a longer phase shifter or as push-pull configuration and the EO-bandwidth can be validated using this EO-response measurement setup.

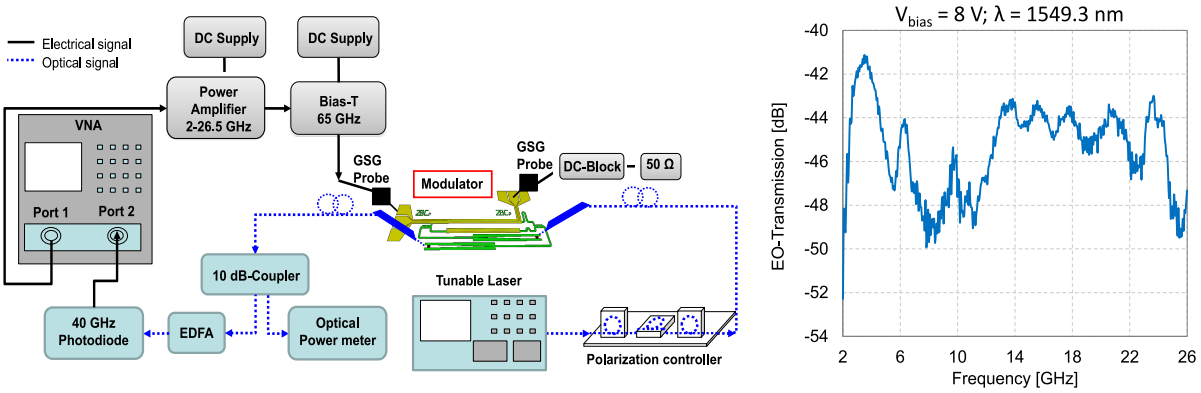

Figure 3.40: Scheme of the measurement setup used for the characterization of the electro-optical response of the modulator and measurement result of the EO-transmission of the Modulator A.

3.4.4 Equivalent circuit model

For the characterization of the TL and the modulator, the electrical behavior of the device is modeled with an equivalent circuit. A basic scheme of the TL with the most important electrical elements is illustrated in Figure 3.41. The impedance and the inductance of the transmission lines are represented by R_{ss} and L, respectively. The metal lines are separated by a distance s and can be modeled as a plate capacitor C_{SG}. The TL together with the active Si and together with the Si substrate have a capacitive behavior defined as C_{SSi} and as C_{sub}, respectively. The effect of the conductivity of the substrate is added in the circuit as the conductance G_{sub}.

This model can be extended to characterize the modulator as shown in Figure 3.42. The pn-region of the optical Si waveguide is modeled with the variable junction capacitor C_{J}. The value of the capacitance depends on the depletion region width, which varies with the applied voltage. The series resistance of the doped Si is defined as R_{s}. The capacitance of the metal vias is modeled by C_{via}.

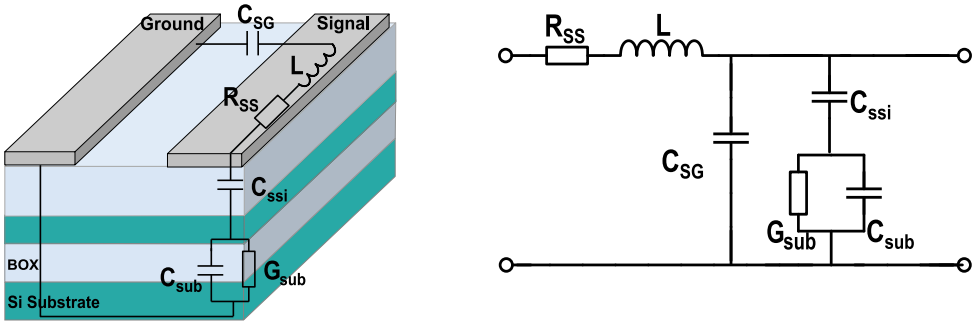

Figure 3.41: 3D Scheme of the TL and the fundamental equivalent circuit.

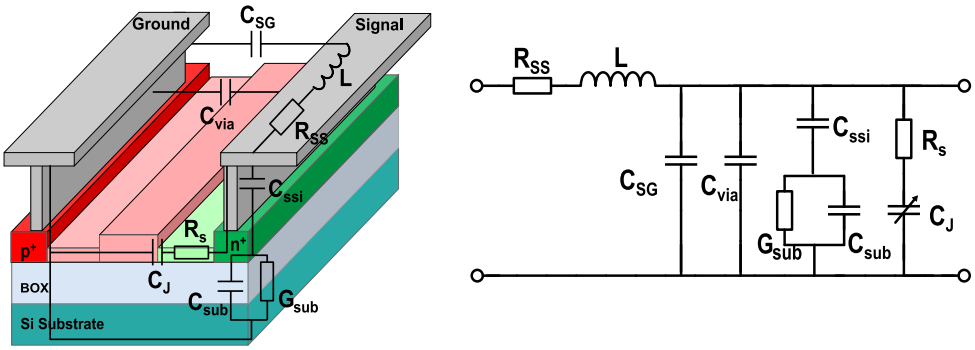

Figure 3.42: 3D Scheme of the modulator and the fundamental equivalent circuit.

A model of the measured straight TL, depicted in Figure 3.26, is realized. The dimensions of the TL are $L_\mathrm{m} = 500\,\mu\mathrm{m}$, $W_\mathrm{m} = 7.9\,\mu\mathrm{m}$ and $s_\mathrm{m} = 2.2\,\mu\mathrm{m}$. This structure has the same substrate as the modulator but without the etched doped waveguide. This simplifies the analysis of the structure. In fact, it allows to identify the impact of the pn-doped Si comparing it with the results of the modulator. An equivalent circuit model of the described TL is presented in Figure 3.43. The resulting values for each electrical component of the simulation realized with the tuning and optimization tool of Schematic ADS are shown. The frequency response, i.e. the S-parameters, of the simulated model are fitted to match the measurements of the TL. The results are plotted in Figure 3.44. The simulated transmission and reflection of the circuit model match well with the measurement results.

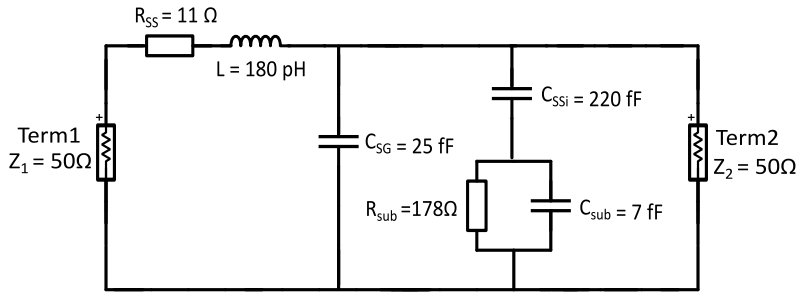

Figure 3.43: Equivalent circuit model of the straight TL with $W_\mathrm{m} = 7.9\,\mu\mathrm{m}$, $s_\mathrm{m} = 2.2\,\mu\mathrm{m}$ and $L_\mathrm{m} = 500\,\mu\mathrm{m}$.

The modulator requires the more elaborate circuit model in Figure 3.42. The S-parameters of the circuit are simulated for different values of the components. However, a mismatch is observed between the simulations and measurements. The results of the theoretical R_s and C_J calculated in chapter 3.3.3 with $V_\mathrm{bias} = 0\,\mathrm{V}$ are added to the equivalent circuit of the TL to model the pn-junction. The circuit model of the modulator is shown in Figure 3.45.

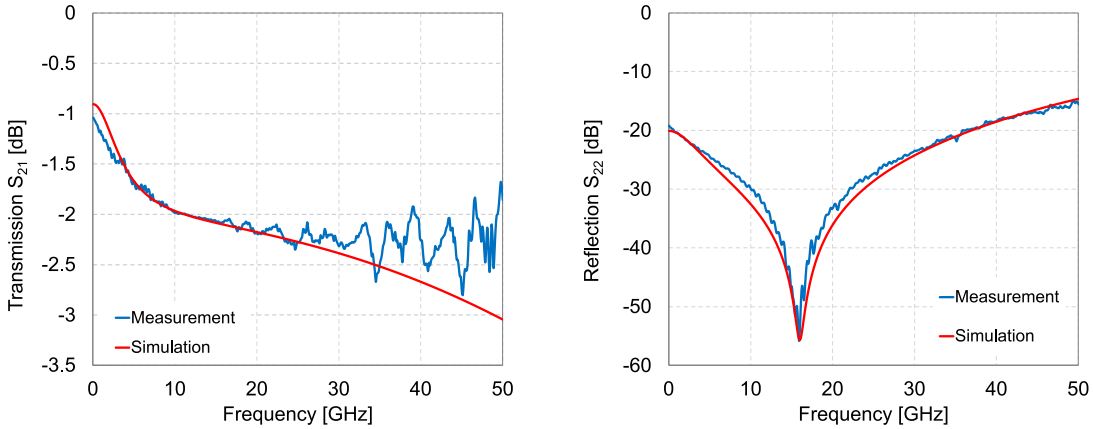

(a) (b)

Figure 3.44: Comparison of the simulated equivalent circuit model of Figure 3.43 with the measurements of the fabricated straight TL with same dimensions. (a) Transmission and (b) reflection.

The comparison of the transmission and reflection between simulation of the circuit model and the measurement is plotted in Figure 3.46. The measurement results of the transmission show a resonance at 30 GHz that is missing in the simulation results of the equivalent circuit model. The resonance is caused due to the propagation of undesired microwave modes. In addition to the coplanar waveguide (CPW) mode, other microwave modes as the slotline mode and the surface wave mode can propagate in a coplanar transmission line [65]. These modes are shown in Figure 3.47. Undesired modes can be limited if certain design guidelines are ensured. For instance, parasitic modes can be reduced if the width of the ground metal line W_g is larger than the signal line width and the space between the lines, i.e $W_g > W_m + 2s_m$. An analysis of the coplanar line modes for different substrates and the design guidelines are given in [66].

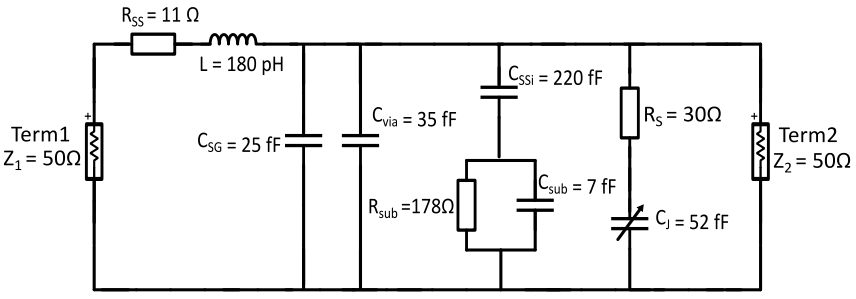

Figure 3.45: Equivalent circuit model of the Modulator A shown in Figure 3.31.

The measured single drive modulator is an asymmetric structure since the pn-structure is

built between the signal line and one of the ground lines of the coplanar transmission line. This asymmetry allows for mode conversion of the CPW mode into the slotline mode. In order to characterize this effect, a simulation is realized with the ADS Schematic tool with the CPW model shown in Figure 3.48 based on the analysis realized in [63]. The TWE of the phase shifter is divided arbitrarily in 5 sections, each one with 100 µm length. An RC-element with $C = 10.4\,\text{fF}$ and $R = 155\,\Omega$ is connected between the signal and one of the ground lines for each section. This represents the capacitance of the pn-junction and the resistance of the pn-structure for a length of 100 µm. A multilayer substrate with the dimensions and characteristics of the substrate of the measured modulator is set up. The simulations results of the transmission and reflection of this CPW effective circuit model is plotted in Figure 3.46. The simulation shows the same resonance at around 30 GHz in the transmission as measured in the fabricated modulator. However, if the ground lines were connected between them with e.g. gold wire bridges [62], the resonance disappears, since the voltage between the ground lines is equalized and the propagation of parasitic modes is avoided. Another possibility to avoid these parasitic modes is the design of a symmetric pn-structure between the coplanar lines, e.g. the push-pull modulator presented in the next chapter in Figure 3.58.

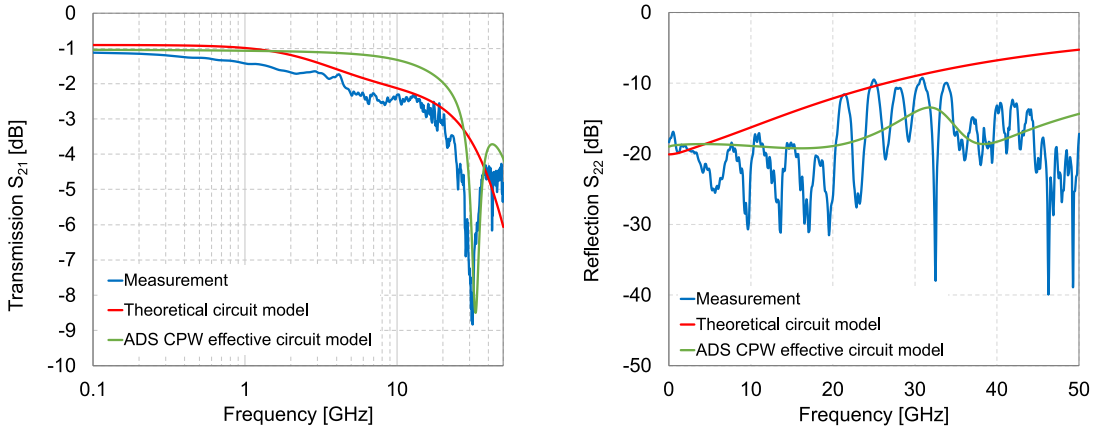

Figure 3.46: Comparison of the measurement of Modulator A ($V_{\text{bias}} = 0\,\text{V}$) with the simulated equivalent circuit model of Figure 3.45 and Figure 3.48. (a) Transmission and (b) reflection.

For the reflection, resonances are only observed for the modulators with L-shape, but not for the straight or the L-shaped TLs (see Figure 3.37(b)). Therefore, these periodic resonances are probably caused by reflections of the electrical signal between the TWE,

i.e. the phase shifter region, and the 90 °-bend of the coplanar TL.

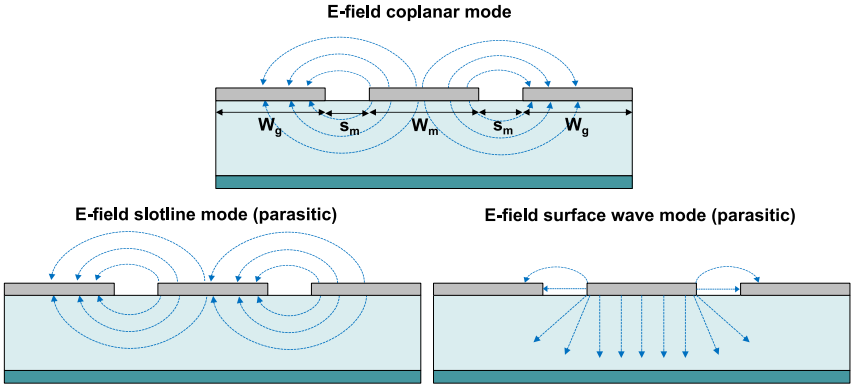

Figure 3.47: Coplanar transmission line modes.

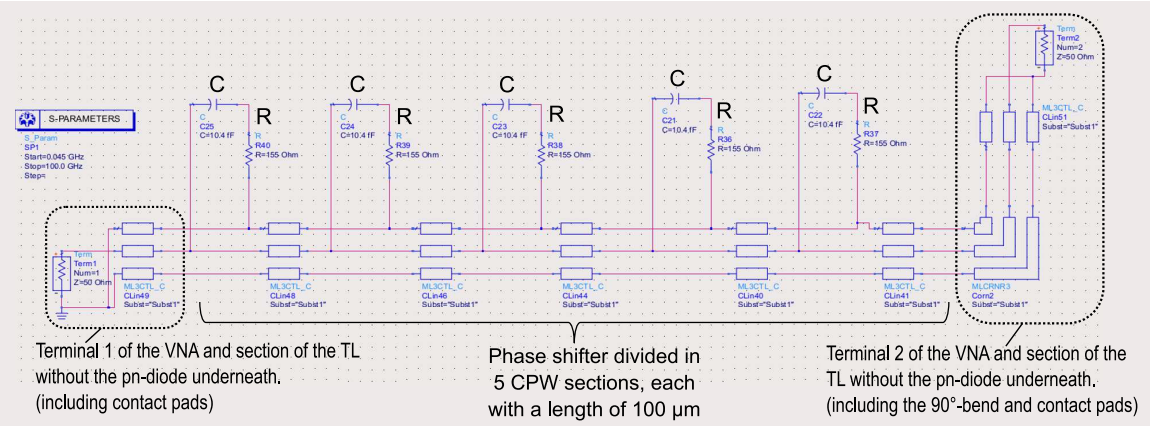

Figure 3.48: ADS CPW effective circuit model of the Modulator A.

3.5 Optimization of the doping profile

For future designs the structure is optimized using different doping concentrations for the p- and n-regions. The influence of the distance between the waveguide core and the highly doped regions on the modulation performance and on the optical loss is investigated. New simulations are realized varying the doping concentration, N_d and N_a, and the distance s_n and s_p to the highly doped regions. The fabricated Modulator A exhibits a good modulation efficiency due to the reduction of $s_\mathrm{n,p}$ with respect to s. Base on the results of the previous simulations and the measured Modulator A, the distance to the metal contacts is set to $s = 1.25\,\mu\mathrm{m}$ and to the highly doped region is set to $s_\mathrm{n,p} = 0.5\,\mu\mathrm{m}$. The cross section of the structure is shown in Figure 3.49. The Δn_eff and the optical loss α of

the structure are simulated for different acceptor concentrations N_a for two different donor concentrations $N_d = 1 \cdot 10^{17}\,\mathrm{cm}^{-3}$ and $N_d = 1 \cdot 10^{18}\,\mathrm{cm}^{-3}$. The highly doped regions are kept as $N_{a+,d+} = 1 \cdot 10^{20}\,\mathrm{cm}^{-3}$. The simulation results of the effective refractive index change are plotted in Figure 3.50(a). The Δn_{eff} for both donor concentrations is similar for a low acceptor concentration $N_a = 5 \cdot 10^{16}\,\mathrm{cm}^{-3}$. However, while Δn_{eff} decreases with larger N_a for the low donor concentration, it almost doubles to $\Delta n_{\mathrm{eff}} \approx 2.5 \cdot 10^{-4}$ for the higher donor concentration. The loss due to the free carrier absorption is shown in Figure 3.50(b). It increases with the doping concentration as expected. The offset between both curves is kept constant for the simulated range of N_a. The modulation efficiency and the figure of merit $V_\pi L \cdot \alpha$ are compared in Figure 3.50(c). From this plot an optimal doping concentration can be chosen for the trade off between the modulation efficiency and the loss. A promising configuration is shown by $N_d = 1 \cdot 10^{18}\,\mathrm{cm}^{-3}$ and $N_a = 9 \cdot 10^{16}\,\mathrm{cm}^{-3}$, since a low $V_\pi L \approx 1.8\,\mathrm{Vcm}$ at 6 V is achieved with a $V_\pi L \cdot \alpha \approx 6\,\mathrm{V} \cdot \mathrm{dB}$.

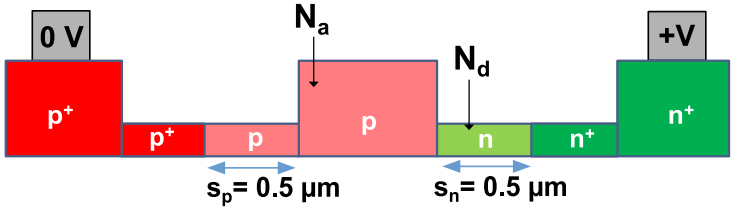

Figure 3.49: Cross section of the simulated structure. Parameters of the phase shifter: $s_p = s_n = 0.5\,\mu\mathrm{m}$, $s = 1.25\,\mu\mathrm{m}$, $h_{sl} = 50\,\mathrm{nm}$, $N_{a+,d+} = 1 \cdot 10^{20}\,\mathrm{cm}^{-3}$

Finally, for the optimized doping $N_a = 9 \cdot 10^{16}\,\mathrm{cm}^{-3}$ and $N_d = 1 \cdot 10^{18}\,\mathrm{cm}^{-3}$ the optimal distance from the waveguide core to the highly doped regions s_n and s_p is investigated. The simulation results for the loss and $V_\pi L \cdot \alpha$ are shown in Figure 3.51. The chosen distance $s_{n,p} = 0.5\,\mu\mathrm{m}$ in Figure 3.49 is a good value. It can be further optimized if the distance is increased to $s_{n,p} = 0.6\,\mu\mathrm{m}$. For this distance, the loss is $\alpha = 0.31\,\mathrm{dB/mm}$ and the modulation efficiency is $V_\pi L = 1.8\,\mathrm{Vcm}$. The figure of merit $V_\pi L \cdot \alpha \approx 5.8\,\mathrm{V} \cdot \mathrm{dB}$ is achieved.

Conclusively, the optimized structure has a p-doped waveguide core with a width of $w = 400\,\mathrm{nm}$. The slab width is $s = 1.25\,\mu\mathrm{m}$ with a thickness of $h_{sl} = 50\,\mathrm{nm}$. The distance to the highly doped regions from the core edge is optimized to $s_{n,p} = 0.6\,\mu\mathrm{m}$. The high doping concentrations are $N_{a+,d+} = 10^{20}\,\mathrm{cm}^{-3}$. The lowly doped regions have a p-doped carrier concentration of $N_a = 9 \cdot 10^{16}\,\mathrm{cm}^{-3}$ and the n-doped carrier concentration is $N_d = 1 \cdot 10^{18}\,\mathrm{cm}^{-3}$. This results in a change of the effective refractive index of $\Delta n_{\mathrm{eff}} = 2.5 \cdot 10^{-4}$ for a reverse bias voltage of 6 V. Thus, the phase shifter length needed

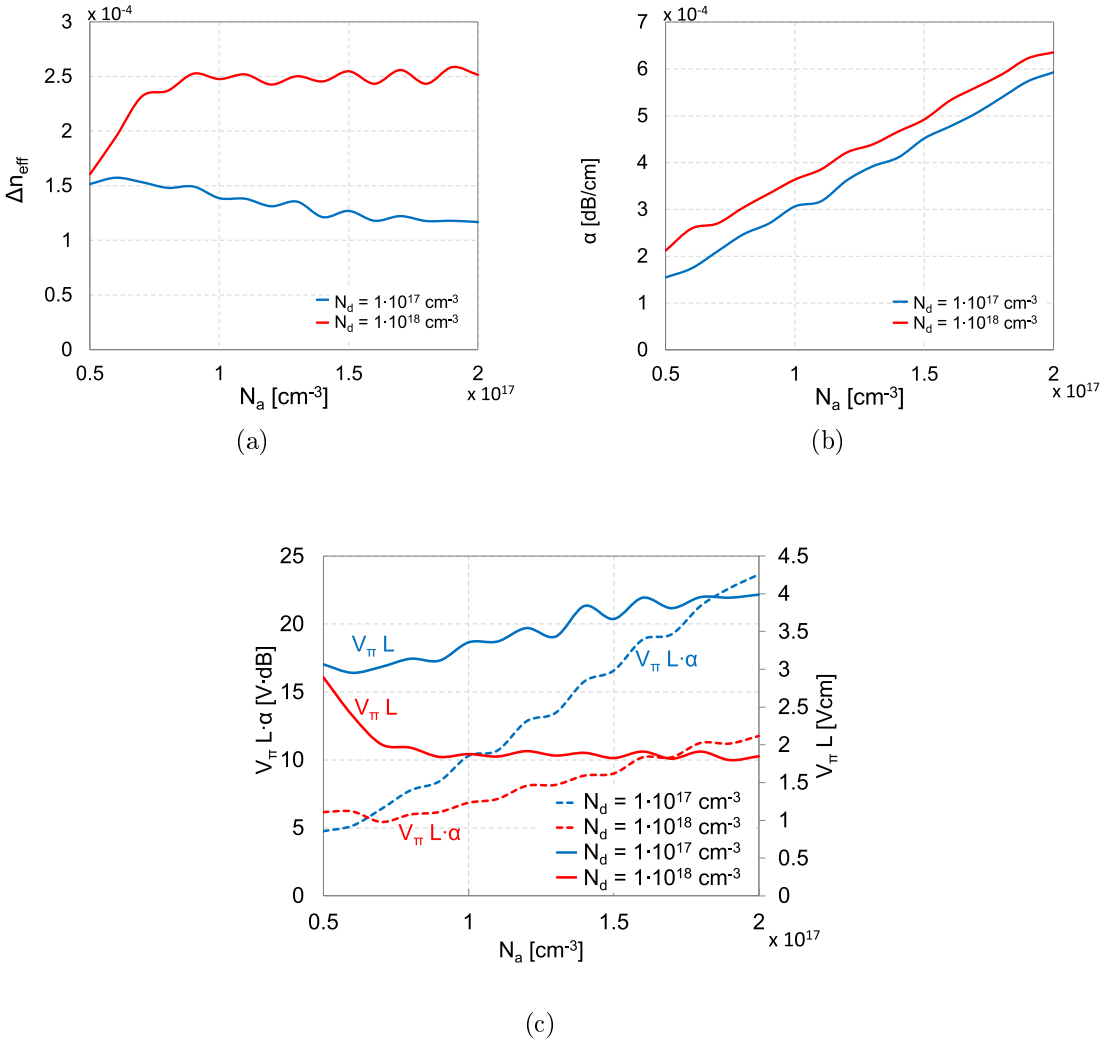

Figure 3.50: Simulations of (a) the change of the effective refractive index at 6 V reverse bias, (b) the optical loss at 0 V bias, (c) modulation efficiency and $V_\pi L \cdot \alpha$ of the phase shifter described in Figure 3.49.

to reach a phase shift of π is given by

$$L_\pi = \frac{\lambda}{2\Delta n_{\text{eff}}} \approx 3.1\,\text{mm}. \tag{3.34}$$

For this structure the calculated cut-off frequency of the pn-diode is 42 GHz and 61 GHz at 2 V and 6 V, respectively.

The fiber-to-fiber loss of the modulator is determined as the sum of the phase shifter loss of 0.97 dB for $L_\pi = 3.1$ mm and the losses of the optical components. The measured loss at $\lambda = 1.55\,\mu$m of the high coupling efficiency GCs is 0.74 dB/coupler and for each MMI

the loss is 0.05 dB. The coupling loss between the 400 nm wide strip waveguide and the rib waveguide of the phase shifter is 0.05 dB/coupling. Each of the linear tapers with a length of 400 µm has a loss of 0.4 dB and the waveguide loss due to the roughness and other imperfections during the fabrication process is 3.3 dB/cm. Therefore, for a phase shifter length of 3.1 mm and around 1 mm of additional intrinsic strip waveguides an ultra-low fiber-to-fiber loss of approximately 4.8 dB is expected for the complete modulator fabricated with the IMS CHIPS technology.

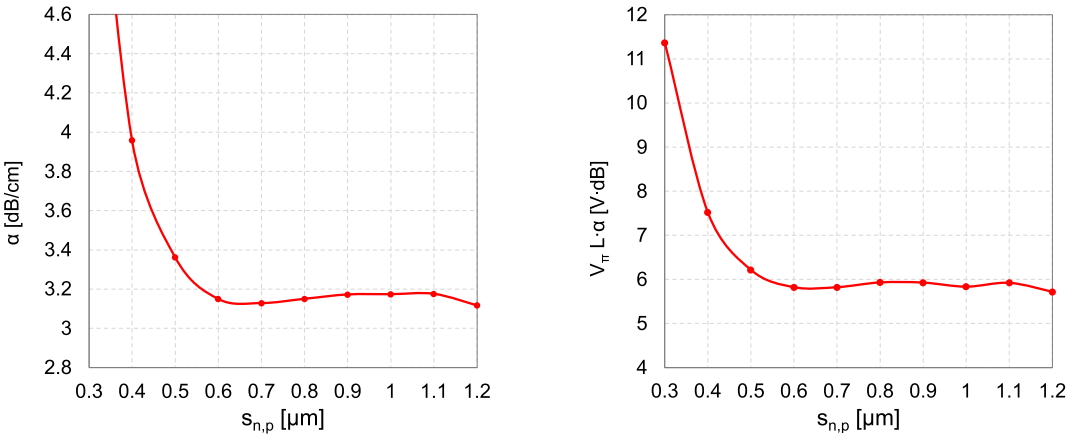

(a) (b)

Figure 3.51: Simulation of (a) the optical loss at 0 V bias and (b) $V_\pi L \cdot \alpha$ depending on the distance $s_{\mathrm{n,p}}$. Being $N_{\mathrm{a}} = 9 \cdot 10^{16}\,\mathrm{cm}^{-3}$, $N_{\mathrm{d}} = 1 \cdot 10^{18}\,\mathrm{cm}^{-3}$, $N_{\mathrm{a+,d+}} = 1 \cdot 10^{20}\,\mathrm{cm}^{-3}$, $s = 1.25\,\mu\mathrm{m}$ and $h_{\mathrm{sl}} = 50\,\mathrm{nm}$.

3.6 Comparison with other technologies

3.6.1 Design in a 220 nm SOI platform

New designs are realized during this work based on a different technology. A die with an area of 7 mm · 7 mm is manufactured at the Leibniz Institute for High Performance Microelectronics (IHP) [67]. Different MZMs and test structures are realized using the new IHP electronic-photonic integrated circuit (EPIC) technology. In Figure 3.52, the final layout and the micrograph of the fabricated die is shown. The wafer has multiple metal layers. The one used for the TLs and TWEs is the top metal with a 3 µm thickness. The TWE is connected to the highly doped Si region through the metal vias. The vias connect the different metal layers between them until reaching the active silicon layer.

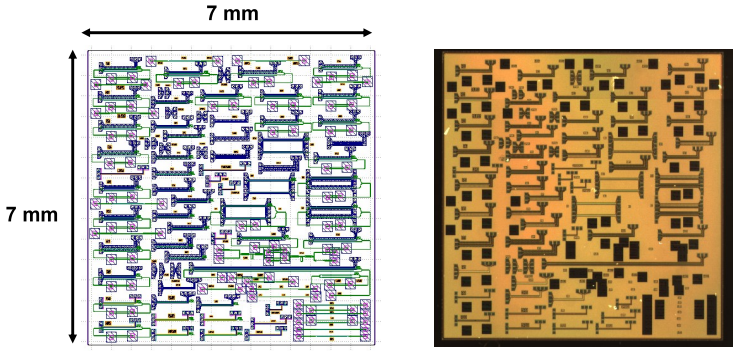

Figure 3.52: Layout and micrograph of the die fabricated with the IHP technnology.

The thickness of the dielectric layer, which isolates the top metal layer and the active Si, is 11.88 µm. The p-doped and the n-doped regions have a doping concentration of $3 \cdot 10^{17}\,\mathrm{cm}^{-3}$ and $1 \cdot 10^{18}\,\mathrm{cm}^{-3}$, respectively. For the highly doped regions, the doping concentration is $1 \cdot 10^{20}\,\mathrm{cm}^{-3}$.

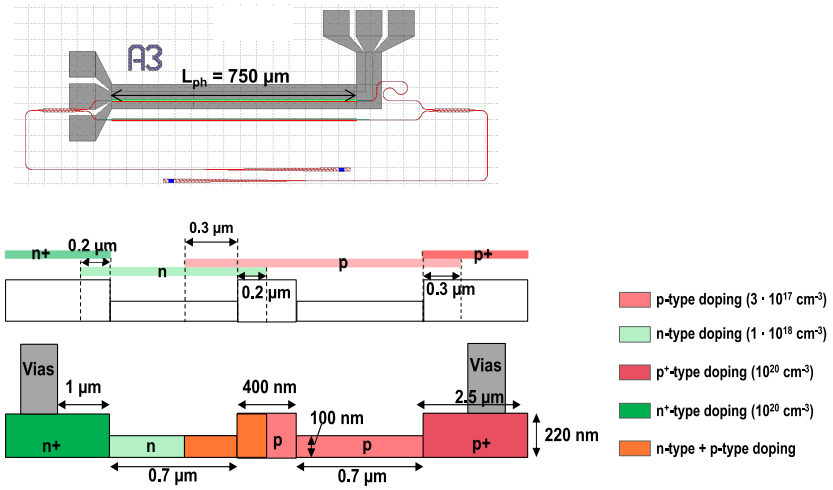

Figure 3.53: Layout and the cross section of the fabricated modulator with the IHP technology including the positioning of the doping masks.

The layout and the cross section of a designed optical MZM is presented in Figure 3.53, where the most important dimensions of the phase shifter and the doping profile are described. The modulator has a phase shifter length of 750 µm. The core of the Si waveguide has a width of 400 nm, a thickness of 220 nm and is p-doped. The slabs have a width of $s = 0.7\,\mu\mathrm{m}$ and a thickness of $h_{\mathrm{sl}} = 100\,\mathrm{nm}$. The metal vias are positioned at 1.7 µm from the waveguide core to avoid additional losses of the optical signal due to the metal. Furthermore, the figure shows the target position of the doping masks. The

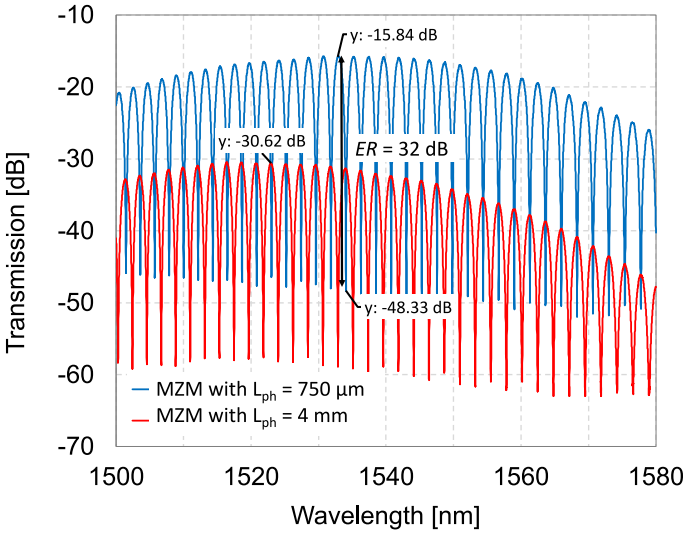

Figure 3.54: Transmission vs. wavelength of the two modulators with same design as shown in Figure 3.53 and different phase shifter lengths.

doping masks overlap in some regions of the waveguide. The goal is to avoid undoped regions in the waveguide due to misalignment of the masks during the fabrication process as it is observed previously with the pn-core waveguides of the IMS CHIPS design. For this MZM, different phase shifter lengths are measured to analyze the optical loss of the structure. Figure 3.54 shows the measured optical transmission of two MZMs with phase shifter lengths of 750 µm and 4 mm, respectively. The IL of the phase shifter is 4.6 dB/mm for 0 V bias voltage. The two arms of the MZMs are identically doped to have the same loss of light in both arms. Hence, an extinction ratio of $ER = 32\,\mathrm{dB}$ is achieved.

The performance of the modulator with the phase shifter length of 4 mm is further investigated. The optical transmission is measured for the applied reverse bias voltages between 0 V and 16 V with a step of 2 V. A phase shift of π is achieved at 16 V reverse bias. The measurement results are plotted in Figure 3.55. The modulator exhibits a modulation efficiency of $V_\pi L = 4.2\,\mathrm{Vcm}$ at 2 V reverse bias voltage. A high active ER of 26 dB is achieved. The optical loss of the 4 mm phase shifter is around 18 dB. In order to fulfill the design rules of the technology used, fillers in each substrate layer shall be used. The silicon fillers are located very close to the waveguides and that can cause additional optical losses. The same problem happens with the TWE, where metal fillers are close to the RF coplanar lines and this can increase the losses of the electrical wave signal.

The electrical RF response of modulators with different TWE designs is investigated. The dimensions of the fabricated TWE are listed in Table 3.1. TWEs with L-shape, similar to

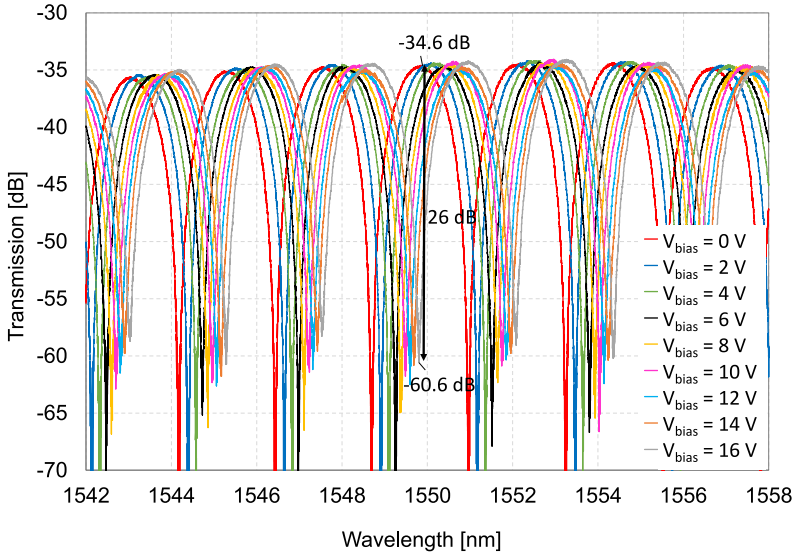

Figure 3.55: Measurement of the optical transmission depending on the reverse bias voltage of the 4 mm MZM fabricated with the IHP technology.

the ones designed for the IMS technology, are also used in this die design. The width W_{m} and the space between the lines s_{m} of the coplanar lines are optimized and adjusted for the IHP technology. In addition, longer phase shifters with $L_{\mathrm{ph}} = 750\,\mu\mathrm{m}$ or $L_{\mathrm{ph}} = 4\,\mathrm{mm}$ are fabricated. Furthermore, in this die other designs of the TWE are included. These are specially loaded coplanar lines. A micrograph of one of them is shown in Figure 3.56(a). These specific periodic transmission lines are fabricated with different metal finger periods showing a huge difference in the results depending on the period. The high frequency performance of the lines can be modified changing the period and the electrical propagation constant can be adapted for a better matching between the electrical and the optical wave velocities. The measurement results of these modulators are compared in Figure 3.56(b). The electrical transmission of all the structures is measured for a bias voltage of 0 V. A dash line, cutting the measured curves, shows the 6 dB electrical bandwidth of the modulators. The TWEs with a standard coplanar configuration, A7 and A12, exhibit a cut-off frequency of 20 GHz. The bandwidth is reduced to almost 6 GHz for the case of the phase shifter length $L_{\mathrm{ph}} = 4\,\mathrm{mm}$. For the special periodic coplanar lines, i.e A5 with a period of 19 µm and A6 with a period of 20 µm, the cut-off frequency are 8 GHz and 20 GHz, respectively. This shows the significant impact of the metal finger period on the RF performance, since the capacitive effect of the lines can be modified.

The modulation efficiency of other MZMs with different doping profiles integrated on the die is examined. An optimized structure is measured where the highly doped silicon

Table 3.1: TWE dimensions of the measured modulators.

Modulator name	A5	A6	A7	A12	A20
L_{ph} [µm]	750	750	750	750	4000
W_{m} [µm]	30	30	40	23.8	23.8
s_{m} [µm]	7	7	8.5	3	3
Period [µm]	19	20	–	–	–

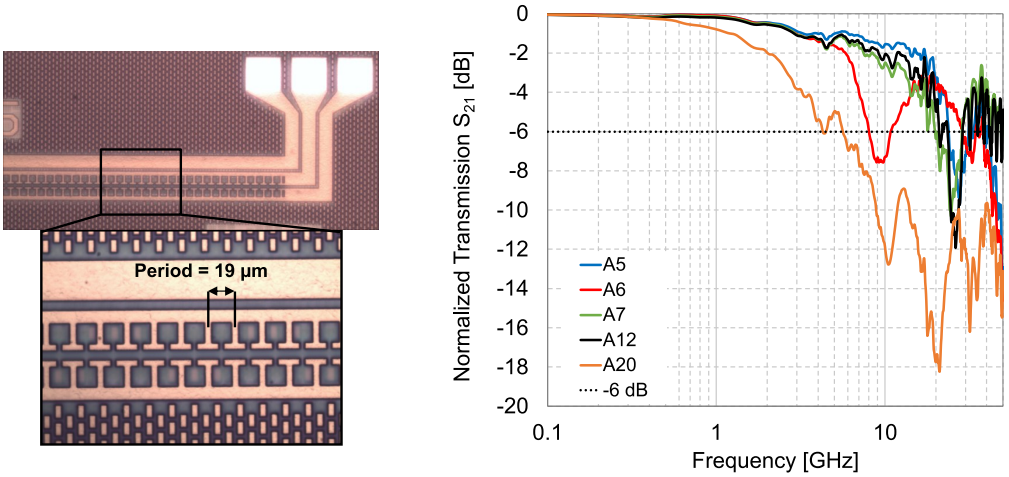

(a) (b)

Figure 3.56: (a) Micrograph of the periodic TWE of the A5 modulator. (b) Measurement of the frequency response of different modulators with 0 V bias voltage.

regions are closer to the waveguide core than the structure shown in Figure 3.53(a). This means, $s_{\mathrm{n,p}} = 0.35\,\mu\mathrm{m}$ instead of $s_{\mathrm{n,p}} = 0.7\,\mu\mathrm{m}$. Due to the overlap of the doping masks different carrier concentration regions are built along the cross section of the waveguide as depicted in Figure 3.57(a). At the same bias voltage, this optimized doping profile leads to a higher free carrier concentration change in the waveguide core where the mode is guided. Hence, the change in the effective refractive index of the fundamental mode is increased. This type of doping profile is also profitable to reduce the electrical resistance in the slabs of the modulator. This modulator has a modulation efficiency $V_\pi L = 2.9\,\mathrm{Vcm}$ at 2 V reverse bias voltage. However, the higher density of free carriers causes more loss of the light due to absorption. The IL of the phase shifter is 5.5 dB higher than the structure presented previously (Figure 3.53(a)) for the same phase shifter length of

750 µm. The optical transmission of the modulator for different reverse bias voltages is shown in Figure 3.57(b).

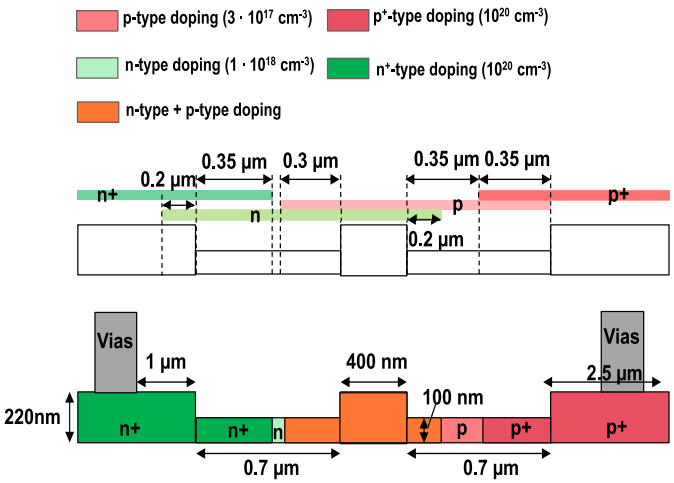

(a)

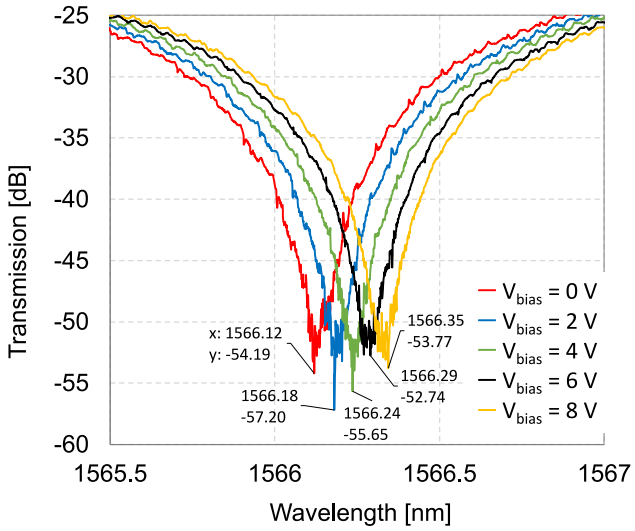

(b)

Figure 3.57: (a) Cross section of the phase shifter with the optimized doping profile and scheme of the target position of the doping masks. (b) Measurement results for different reverse bias voltages of the MZM with the optimized doping profile.

As demonstrated in Figure 3.56, the length of the TWE has a direct impact on the electrical bandwidth of the modulator. The aim is to keep the length of the device as short as possible and at the same time achieve a high modulation efficiency. Thereby, a higher phase shift of the optical signal can be obtained without diminishing the bandwidth.

For this purpose a push-pull MZM is designed. The layout of this modulator is presented in Figure 3.58(a). It has a phase shifter in both arms of the interferometer. The TWE has a GSG configuration. The signal metal line is connected through vias to both arms of the MZM. For the upper arm, the signal line is connected to the p-doped region of the rib waveguide and the ground to the n-doped region. For the bottom arm, the signal metal line is connected to the n-doped region and the ground to the p-doped region. Hence, when the RF signal travels through the TWE, one arm operates in forwards bias and the other arm in reverse bias.

The measured optical transmission of the modulator for different bias voltages is plotted in Figure 3.58(b). The passive $ER = 30\,\mathrm{dB}$ and the active ER is around 20 dB. The fiber-to-fiber IL is 18 dB for a phase shifter length of $L_{\mathrm{ph}} = 1\,\mathrm{mm}$. With this push-pull configuration, a high modulation efficiency is achieved. Figure 3.58(c) shows the modulation efficiency of the device depending on the applied bias voltage. For a bias voltage of 0.5 V the $V_\pi L$ is 1.4 Vcm. For higher bias voltages, this value is even lower, achieving 0.25 Vcm at 2 V bias voltage.

Finally, the frequency response of the TWE is plotted in Figure 3.59. The 6 dB cut-off frequency of the modulator is around 10 GHz. The reflection is above $-5\,\mathrm{dB}$ between 10 GHz and 42 GHz. This is due to the change of the impedance of the RF lines when two diodes are connected in series under the coplanar metal lines. The mismatch between the impedances causes higher reflections of the RF signal.

A comparison of the designs presented in this work based on a 220 nm SOI platform and a 250 nm SOI platform together with some of the state of the art devices developed by other research groups is presented in chapter 3.6.2. Some of the most important design parameters and figures of merit that describe the performance of the modulators are summarized in Table 3.2.

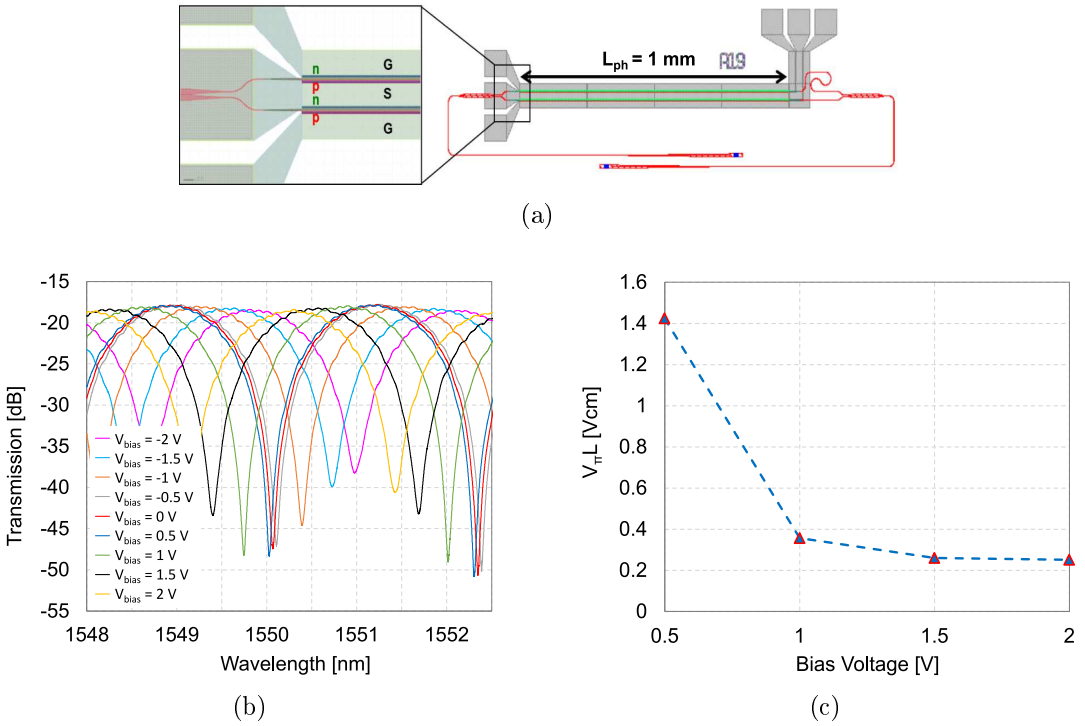

(a) (b) (c)

Figure 3.58: Push-pull MZM: (a) Layout. (b) Measurement results of the optical transmission for different bias voltages. (c) Modulation efficiency $V_\pi L$ vs. bias voltage.

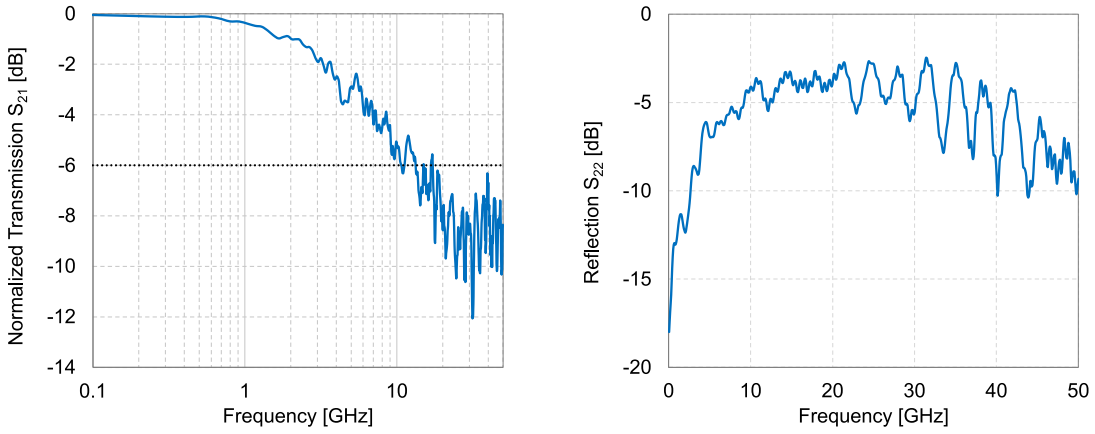

(a) (b)

Figure 3.59: Measurement of the electrical (a) transmission and (b) reflection of the push-pull MZM at 0 V bias voltage.

3.6.2 State of the art

Silicon optical modulators are developed by several research groups in the last years. High speed modulators are investigated with different materials, architectures and physical phenomenons. An overview of the state of the art is presented in [68].
Some of the most relevant published Si modulators based on the carrier-depletion effect are compared in Table 3.2 including the results of the designs of this work. The modulators are listed based on design of the pn-diode of the phase shifter. These design types are: lateral [63][69][70][71][72][73][74], interdigitated [75][62][76] or vertical pn-junction [77][71]. The vertical and interdigitated patterns exhibit a good compromise between modulation efficiency $V_\pi L$ and optical loss α. However, they require more complexity of the lithography processes to locate precisely the pn-junction.
There is a trade-off between the modulation efficiency and the phase shifter loss. Designs with high modulation efficiency, i.e. low $V_\pi L$, typically exhibit also a high optical loss, e.g. in [71] $V_\pi L = 0.97\,\mathrm{Vcm}$ and $\alpha = 7.1\,\mathrm{dB/mm}$. A notable case is the modulator based on the slow light effect [70]. This modulator can be integrated on a very small area and a very low $V_\pi L$ of 0.85 Vcm is achieved. However, the loss of the slow light modulator is significantly higher than the loss of the other modulators.
High speed modulations with up to 100 Gbit/s OOK transmission [74] and up to 60 GHz bandwidth [72] have been demonstrated. It can be observed that for the modulators with a small distance to the highly doped regions $s_{\mathrm{n,p}}$, exhibit better modulation efficiency. Besides, this allows the reduction of the series resistance of the modulator contributing to the enhancement of the bandwidth of the device. Nevertheless, this also increases the absorption of the light, i.e. optical loss α, due to the free carriers. To overcome this problem, intermediate doping concentration regions between the highly doped and the lowly doped regions can be added to reduce the series resistance while keeping a low optical loss [72]. To increase the electrical bandwidth, the Si substrate is in this design etched in some regions to diminish that the electrical mode field distribution pattern is pulling down to the high permittivity silicon substrate.
The 220 nm SOI platform is the technology that most of the research groups use. In this work, a new technology with a 250 nm SOI platform is used. The modulators are designed reducing complexity in the etching and doping fabrication processes. This shows promising results of the first prototype and simulations achieving high electrical bandwidth. Additionally, the design of a push-pull modulator fabricated with a 220 nm SOI platform is demonstrated in this work with a very good modulation efficiency of 0.25 Vcm and an electrical bandwidth of 10 GHz.

Table 3.2: State of the art of carrier-depletion phase shifter designs on different SOI technologies for C-band.

Type	h [nm]	L_{ph} [mm]	h_{sl} [nm]	$s_{\mathrm{n,p}}$ [µm]	α [dB/mm]	$V_\pi L$ [Vcm] (bias)	f_{c} [GHz] (bias) or Data rate	Reference
A	220	1	100	–	2.8	1.72 (2 V)	30 (2 V)	[69]
A*4	220	5.5	100	–	0.9	2.20 (4 V)	24 (5 V)	[63]
A	220	0.5	100	$s_{\mathrm{p}} = 0.50$ $s_{\mathrm{n}} = 0.55$	10.0	0.85 (5 V)	Data rate: 40 Gbit/s	[70]
A*1	220	2.4	100	–	7.1	0.97 (0 V – 2 V)	61 (1 V)*3	[71]
A	220	2	90	$s_{\mathrm{p}} = 0.78$ $s_{\mathrm{n}} = 0.68$	2.2	1.40 (4 V)	60 (8 V)	[72]
A	220	6	95	0.95	0.3	7.20 (4 V)	5 (4 V)	[73]
A	–	2.47	–	–	2.7 (1 V)	1.50 (1 V)	Data rate: 100 Gbit/s	[74]
B	340	0.75	80	1.0	1.0	1.62 (2 V)	20 (3 V)	[75]
B	220	1	90	0.6	2.8	2.20 (2 V)	30 (3 V)	[62]
B	220	2	45	–	1.1	0.60 (2 V)	5 (2 V)	[76]
C*1	290	1.8	–	0.8	4.2	0.74 (0 V – 2 V)	48 (1 V)	[71]
C	500	1	–	1.0	1.8	< 4	30 (3 V)*3	[77]
A*4	250	0.5	80	0.4	2.0	3.10 (2 V)	30 (2 V) > 50 (6 V)	This work
A*1*4	250	3.1	50	0.6	0.3*2	1.80 (6 V)	61 (6 V)*3	This work
A*4	220	4	100	0.7	4.6	4.20 (2 V)	6 (0 V)	This work
A*4	220	0.75	100	0.35	11.4	2.90 (2 V)	20 (0 V)	This work
A	220	1	100	0.7	4.6	0.25 (2 V)	10 (0 V)	This work

Note: Type (A) Lateral, (B) Interdigitated, (C) Vertical.
*1 Simulated/calculated
*2 Only free carrier absorption at 0 V
*3 Intrinsic pn-diode cut-off frequency
*4 Single drive

4 Summary and outlook

This chapter summarizes the most significant results of the research on two-dimensional grating couplers, tapers and optical Mach-Zehner modulators designed in this work. In addition, an outlook on possible future research is given on how to investigate further design parameters and their effects.

The first part of the work is focused on the design of two-dimensional grating couplers. These structures allow the coupling of light into embedded waveguides and split the orthogonal light polarizations, TE and TM, into different outputs. The effect on coupling efficiency and optical bandwidth of different geometrical parameters of these structures is investigated. The couplers are designed for a 250 nm SOI platform. The shape and position of the etched holes in the silicon are varied. The holes, cylinder or cuboids, of the 2DGCS are placed periodically. Additionally, for the structure with cuboidal holes, a design with an aperiodic grating is investigated. The coupling efficiency of the 2DGCS are optimized with the use of a backside metal mirror to reduce light losses into the substrate. The results and dimensions of the most relevant simulated structures are summarized in Table 4.1.

Table 4.1: Results of the simulated 2DGCS designs with backside mirror at $\lambda = 1.55\,\mu m$.

Hole Shape	R or a [nm]	Λ [µm]	N	θ [°]	TE Coupling efficiency [dB]	TM Coupling efficiency [dB]	1 dB-BW [nm]	3 dB-BW [nm]
Cylinder	200	580	19	–	−1.9	−2.0	38	66
Cylinder	200	580	23	–	−1.8	−1.9	36	62
Cuboid	360	580	23	30	−1.9	−2.1	35	61
Cuboid	-	Aper.	23	0	−1.7	−1.9	36	63

For identical dimensions of the 2DGCS the coupling efficiency is enhanced with a higher number of holes $N \cdot N$ until the coupling efficiency converges at $N = 23$. This is correlated

with the dimensions of the electric field profile of the optical fiber. However, the 1 dB-BW and 3 dB-BW are higher for the structure with $N = 19$.

The 2DGCSs are designed by optimizing the period of the holes Λ and the hole radius R for the structure with cylindrical holes. For the one with cuboids, the edge length a and the rotation angle θ are optimized. The 2DGCS design with cylindrical holes exhibits a slightly higher coupling efficiency than with cuboids.

From the optimized periodic structure with cuboids, research on aperiodic grating is conducted. It is observed that the modification of the hole dimensions of the first lines of holes of the grating contributes to a better matching of the fiber electric field profile and the one of the diffraction grating. A genetic algorithm is used to calculate the length and width of the holes for the first 5 lines. In order to avoid an overlapping of the holes, the rotation angle is set to $\theta = 0\,^\circ$. The coupling efficiency achieved is -1.7 dB for the TE polarization and -1.9 dB for the TM polarization. The 1 dB-BW and 3 dB-BW are 36 nm and 63 nm, respectively. This shows promising results using this technology and further research in this field is recommended for future work.

A simulation sweep with a variation of the dimensions of more grating lines as sweep parameter can be realized to continue the study of the effect on the coupling efficiency and bandwidth of the aperiodic grating. It would be interesting to modify the holes independently to accurately match the electric field profiles of the fiber and the grating. However, the optimization of such a large number of parameters leads to a high time consuming simulation effort.

Moreover, the algorithm used for the simulation of the aperiodic grating can be modified to sweep the dimension of the cylinders instead of the cuboids. In this case, the resulting holes of the aperiodic grating would have an elliptical shape. Other design parameters as the depth of the etched holes or a different hole shape could also be investigated.

In order to reduce the area of the grating coupler and the taper to couple light from the fiber to a single mode waveguide with a width of 400 nm, two-dimensional focusing grating couplers are investigated. The holes in this type of gratings are positioned along cofocal ellipses defined by the parameter q. This special position of the holes allows for a higher focusing of light. The distance from the coupler edge to the point with the maximum focus of light is calculated and defined as b. The simulation results of the most relevant structures with and without a backside mirror are presented in Table 4.2. A 2DFGC design with cylindrical holes and with a focal distance $b = 26.2\,\mu$m exhibits a coupling efficiency of -2.4 dB and -2.5 dB for the TE and the TM polarizations, respectively. Other designs are optimized to reduce the distance of the maximum focus of the light up

to $b = 17.5\,\mu m$, achieving a coupling efficiency of $-2.7\,dB$ for the TE polarization and $-2.9\,dB$ for TM and a 1 dB-BW of 45 nm.

Table 4.2: Results of the simulated 2DFGC designs with and without backside mirror. $\Lambda = 610\,\mu m$ and $\lambda = 1.55\,\mu m$.

Hole Shape	R or a [nm]	N	θ [°]	q_{min}	b [µm]	Mirror	TE Coupling efficiency [dB]	TM Coupling efficiency [dB]	1 dB-BW [nm]
Cyl.	255	23	–	50	26.2	No	−4.5	−4.7	–
						Yes	−2.4	−2.5	40
Cub.	440	19	36	34	17.5	No	−5.4	−5.4	45
						Yes	−3.1	−3.2	46
Cyl.	255	19	–	34	17.5	No	−5.0	−5.1	43
						Yes	−2.7	−2.9	45

The total coupling efficiency and the 1 dB-BW of the 2DFGC together with the taper is summarized in Table 4.3. Using a customized taper with the same length as the focal distance b to couple light into a monomode waveguide, a coupling efficiency of $-3.1\,dB$ and $-3.2\,dB$ are achieved for the TE and TM polarizations, respectively.
A different construction is designed where the coupler is followed by a waveguide with the same width as the 2DFGC and with length b. This waveguide is followed by an adiabatic taper with a length of $100\,\mu m$. The total coupling efficiency for this coupling system is $-2.4\,dB$. This means, no losses are added due to the taper. However, if the orthogonal 2DGCS is used to couple the light into a monomode waveguide with a width of 400 nm, the linear adiabatic taper has to have a length of at least $400\,\mu m$ to avoid additional loss. The 2DFGC coupler design allows for the reduction of the taper length by a factor of 4.
A prototype of the 2DFGC with customized tapers is fabricated at IMS CHIPS. The area of 2DFGC including the tapers is $30\,\mu m \cdot 32\,\mu m$. The device is measured showing a coupling efficiency of $-7\,dB$ and $-7.6\,dB$ for the TM and TE polarizations, respectively. This coupling efficiency can be significantly improved with the use of a backside metal mirror, since the IMS CHIPS technology is optimized to add a metal mirror at the bottom of the BOX layer. A future tape-out, adding a metal mirror fabrication step, is recommended.

Table 4.3: Results of the 2DFGC designs with taper. $\Lambda = 610\,\mu m$

Hole Shape	R [nm]	N	Taper	q_{min}	Taper length [µm]	Mirror	TE Coupling efficiency [dB]	TM Coupling efficiency [dB]	1 dB-BW [nm]
Cyl.*1	255	23	Custom	50	26.2	Yes	−3.1	−3.2	40
Cyl.*1	255	23	Adiabat.	50	100	Yes	−2.4	−2.5	40
Cyl.*2	250	19	Custom	34	19.6	No	−7.6	−7.0	30

*1 Simulated ($\lambda = 1.55\,\mu m$). *2 Measured ($\lambda = 1.56\,\mu m$).

The second part of the work is focused on the design of an optical carrier-depletion MZM in a 250 nm SOI technology. The parameters of the device, e.g. the doping concentration and profile of the free carriers in the rib Si waveguide, the dimensions of the waveguide and the TWE, are optimized to achieve a high bandwidth and modulation efficiency while maintaining low electrical and optical losses of the signals. An analysis of the electrical bandwidth of the modulator for different doping profiles is described. Furthermore, RF coplanar lines with different dimensions and shapes are simulated and measured achieving a 3 dB-bandwidth higher than 50 GHz.

A single-drive MZM is fabricated and measured delivering a modulation efficiency of $V_\pi L = 3.1\,Vcm$ at 2 V reverse bias voltage. The length of the phase shifter is 0.5 mm with an optical loss of $\alpha = 2\,dB/mm$. The electrical bandwidth of the modulator is 30 GHz. The TL and the modulator are modeled with an equivalent circuit. This allows for further optimization of the modulator on the electrical circuit level. In future, the modulator model can be simulated together with the electrical circuit of the transmitter and the complete circuit can be improved matching the impedance to avoid undesired reflections.

Further simulations are realized to enhance the modulation efficiency and optical loss of the modulator achieving a theoretical modulation efficiency of $V_\pi L = 1.8\,Vcm$ and a maximum optical loss of the phase shifter of $\alpha = 0.31\,dB/mm$. The expected fiber-to-fiber loss of an MZM with a phase shifter length of 3.1 mm is 4.8 dB.

In the fabricated die, a higher optical loss compared to the same test structures of other tape-outs fabricated with the IMS CHIPS technology are observed. The difference might derive from a fabrication deviation. For further research, it is recommended to fabricate the measured modulator and the optimized design again and compare the results. In

addition, in order to avoid undesired undoped regions or incomplete etched Si regions of the waveguides, an overlap of the doping and the etching masks has to be considered.
Finally, single-drive and dual-drive MZMs are fabricated in a 220 nm SOI technology with the IHP technology. A modulation efficiency of $V_\pi L = 0.25\,\mathrm{Vcm}$ at 2 V reverse bias voltage is demonstrated for a push-pull modulator. The 6 dB electrical bandwidth of the TWE is 10 GHz. Different TWE designs are simulated and measured for this technology achieving a 3 dB electrical bandwidth of 6 GHz for a phase shifter length of 4 mm and 20 GHz for a length of 750 µm.
For future designs, the use of sub-λ doped waveguides to build compact modulators is an interesting field to be investigated. With the IMS CHIPS technology some designs are reported showing excellent results for sub-λ intrinsic Si waveguides [78] and MMIs [55]. With the knowledge of this work regarding the doping process and modulation results of the respective technology this research field can be further improved. To enhance the bandwidth of the device, the fabrication of symmetrical MZMs to avoid unwanted microwave parasitic modes is recommended. In addition, etching the complete active silicon layer, except the modulator waveguides, avoids extra losses of the electrical mode along the TWE. Moreover, wafers with a high resistivity Si substrate would also reduce the electrical loss. The use of intermediate tunable delay lines to adjust the phase velocity of the optical and the electrical signal for long modulators can also be studied to analyze its influence on the EO-bandwidth of the modulator.

A Fabrication deviations

The measurement results of some optical waveguides and coplanar lines fabricated with the IMS technology shows undesired ripples or higher losses than simulated. Courtesy of IMS CHIPS, a scanning electron microscope (SEM) is used to take pictures of some parts of the fabricated structures. The SEM pictures are presented in Figure A.1. The two pictures on top show the top view of the transition between a 400 nm width silicon waveguide and the phase shifter section of the modulator. The red ellipses mark the regions where the silicon was not etched properly. That can produce additional losses of the optical signal that could be avoided. In addition, deviations of the target dimensions are observed. For instance, the width of the monomode waveguide is 14 nm wider than specified and the slabs of the modulator have a width of 0.65 µm instead of 0.7 µm. These points can be taken into account for developing the technology in collaboration with IMS CHIPS. For instance, the layouts can be redesigned with some overlap of the etching layers and also between the doping layers. A design kit where the fabrication rules are described, e.g. the minimum and maximum dimensions of the structures, the tolerances and the overlap of the mask layers, can be developed for future designs.
The bottom left picture shows the cross section of the rib waveguide of the modulator. The slab thickness target was 50 nm. Due to difficulties of the etching process to achieve this thin slab thickness, the structures are fabricated finally with 80 nm slab thickness.
The bottom right picture shows a monomode waveguide inside the red dashed lines and on top the AlSiCu metal line. Due to the 1 µm SiO_2 coating over the Si waveguide, the metal line is not flat any more. That could cause additional losses for the electrical high frequency signal. These irregularities are not taken into account by the simulations and that could be a reason for a deviation between measurements and simulations.

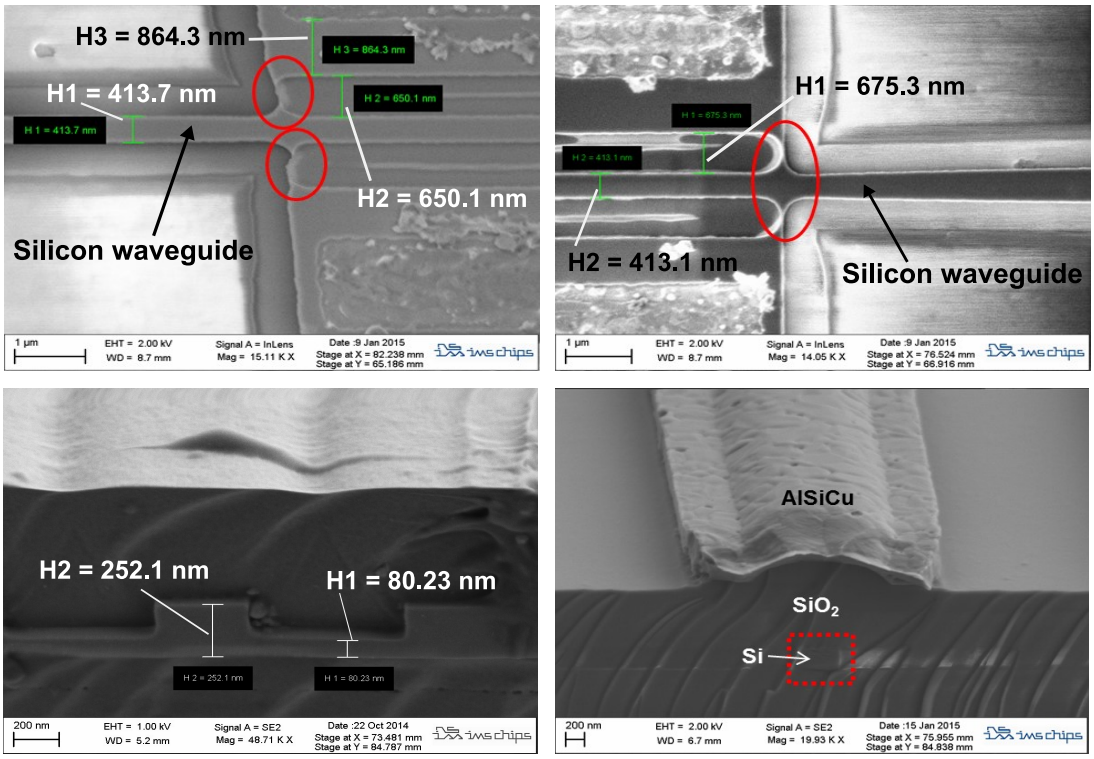

Figure A.1: SEM pictures of some structures of the die fabricated by IMS CHIPS.

B Heterodyne measurement setup

A heterodyne measurement setup is used to measure the frequency response of the broadband photodiode used for the measurements of the optical modulator. The characterization of the photodiode is realized for the later calibration of the modulator measurement setup. A scheme of the heterodyne setup is shown in Figure B.1. Two tunable lasers are used as light source. One of them emits a light signal with a wavelength $\lambda = 1550\,\text{nm}$ and the other laser the same but with adding a small wavelength difference $\Delta\lambda$. Both light outputs are combined with a 3 dB-coupler. Afterwards, the light is amplified with an EDFA and filtered to avoid undesired frequencies. The optical power is adjusted by means of an optical attenuator and the light signal is later divided with a 10 dB-coupler. The 10 % of light is sent to an optical powermeter and the other 90 % is sent to the photodiode under test. The photodiode can be embedded on wafer or a separate device. In this last case, the optical fiber is connected to the photodiode by means of an standard optical connector and the output RF signal with and electrical broadband RF cable without the need of an RF probe. In order to measure the electrical transmission depending on the frequency, an electrical power meter is connected through a bias-T to the output of the photodiode. The bias voltage is applied by a voltage source and this is connected to the DC connector of the bias-T. The measured results for the desired frequency range are collected by means of an automatized software.

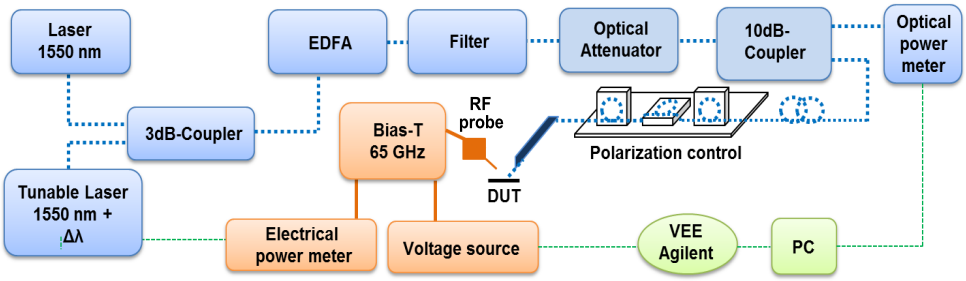

Figure B.1: Scheme of the heterodyne measurement setup.

An example of a measurement realized with this setup is shown in Figure B.2. An u^2t photodiode with a 3 dB-bandwidth of 50 GHz is measured. The results are compared

with the specifications, i.e. datasheet, of the device. It can be observed that very similar results between specifications and measurement with the heterodyne setup are obtained.

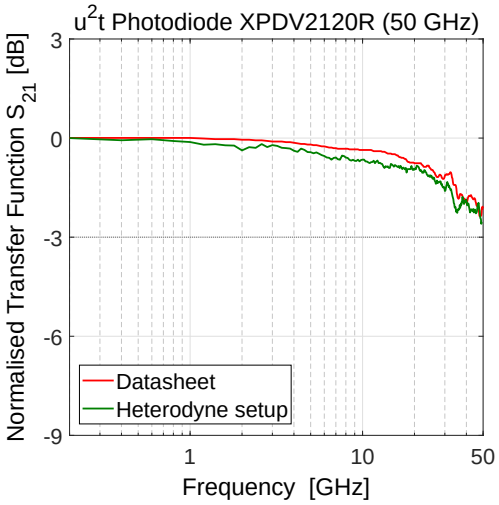

Figure B.2: Comparison between specifications and measurement with the heterodyne setup of the transfer function curve of a 50 GHz u^2t photodiode.

Supporting Research Works

The following student works have contributed to the accomplishment of this thesis. Their support and motivation have helped for the realization of the research.

- Andreas Zibold: *Design and Simulation of an Optical Modulator in SOI Technology.* Research Thesis, March 2014.
- Lotte Rathgeber: *E*ntwurf von integrierten optischen Silizium-Modulatoren mit Sub-Lambda-Wellenleitern. Master Thesis, July 2015.
- Pablo De La Torre Castro: *Design and Simulation of Two Dimensional Grating Couplers in Silicon-on-Insulator Technology.* Master Thesis, September 2016.
- Kateryna Guguieva: *Design of electrical transmission lines for the measurements in a rubidium vapor cell.* Bachelor Thesis, November 2016.
- Fatema Tasneem: *Simulation of transmission lines.* Student assistant, 2016.
- Raik Elster: *Charakterisierung von Wanderwellenelektroden für optische Siliziummodulatoren.* Masterarbeit, February 2017.

Bibliography

[1] Ebeling, K. J.: *Integrated Optoelectronics: Waveguide Optics, Photonics, Semiconductors.* Springer, Berlin, Heidelberg, 1993.

[2] Berroth, M.: *Optoelectronic Devices and Circuits II.* 2014.

[3] Thorne, K. S., Blandford, R. D.: *Modern Classical Physics: Optics, Fluids, Plasmas, Elasticity, Relativity, and Statistical Physics.* Princeton University Press, Princeton, Oxford, 2017.

[4] Serway, R. A., Jewett, J. W.: *Physics for Scientists and Engineers.* Brooks/Cole-Thomson Learning, Belmont, CA., 6th International Student edition, 2004.

[5] Radi, H. A., Rasmussen, J. O.: *Principles of Physics for Scientists and Engineers.* Undergraduate Lecture Notes in Physics. Springer, Berlin, Heidelberg, 2013.

[6] Bai, B., Laukkanen, J., Kuittinen, M., Siitonen, S.: *Optimization of Nonbinary Slanted Surface-Relief Gratings as High-Efficiency Broadband Couplers for Light Guides.* Applied Optics, Vol. 49 : 5454–5464, 2010.

[7] Cheng, L., Mao, S., Li, Z., Han, Y., Fu, H. Y.: *Grating Couplers on Silicon Photonics: Design Principles, Emerging Trends and Practical Issues.* Micromachines, Vol. 11 (No. 7), 2020.

[8] Sfar Zaoui, W., Kunze, A., Vogel, W., Berroth, M., Butschke, J., Letzkus, F., Burghartz, J.: *Bridging the Gap between Optical Fibers and Silicon Photonic Integrated Circuits.* Optics Express, Vol. 22 (No. 2): 1277–1286, 2014.

[9] Taillaert, D.: *Grating Couplers as Interface between Optical Fibres and Nanophotonic Waveguides.* PhD Thesis, Ghent University, 2004.

[10] Petit, R.: *Electromagnetic Theory of Gratings: Ed. by Roger Petit.*, volume 22 of *Topics in Current Physics.* Springer, Berlin, Heidelberg, 1980.

[11] Peng, S. T., Tamir, T., Bertoni, H. L.: *Theory of Periodic Dielectric Waveguides.* IEEE Transactions on Microwave Theory and Techniques, Vol. 23 (No. 1): 123–133, 1975.

[12] Bienstman, P.: *Rigorous and Efficient Modelling of Wavelength Scale Photonic Components.* PhD Thesis, Ghent University, 2001.

[13] CAMFR: *http://camfr.sourceforge.net/index.html*, 2021.

[14] FIMMPROP: *Photon Design. Version 6.1.1.*, 2014.

[15] FullWAVE: *RSoft tool. Synopsys Product. FDTD Simulation of Photonic Structures.*, 2014.

[16] Matlab: *Genetic Algorithm. http://de.mathworks.com/discovery/ genetic-algorithm.html*, 2016.

[17] Sfar Zaoui, W., Félix Rosa, M., Vogel, W., Berroth, M., Butschke, J., Letzkus, F.: *Cost-effective CMOS-compatible Grating Couplers with Backside Metal Mirror and 69% Coupling Efficiency.* Optics Express, Vol. 20(No. 26):B238–B243, 2012.

[18] Chen, X., Li, C., Fung, C. K. Y., Lo, S. M. G., Tsang, H. K.: *Apodized Waveguide Grating Couplers for Efficient Coupling to Optical Fibers.* IEEE Photonics Technology Letters, Vol. 22 (No. 15): 1156–1158, 2010.

[19] Marchetti, R., Lacava, C., Khokhar, A., Chen, X., Cristiani, I., Richardson, D., Reed, G., Petropoulos, P., Minzioni, P.: *High-Efficiency Grating-Couplers: Demonstration of a New Design Strategy.* Scientific Reports, Vol. 7 , 2017.

[20] Benedikovic, D., Cheben, P., Schmid, J. H., Xu, D.-X., Lamontagne, B., Wang, S., Lapointe, J., Halir, R., Ortega-Monux, A., Janz, S., Dado, M.: *Subwavelength Index Engineered Surface Grating Coupler with Sub-decibel Efficiency for 220-nm Silicon-on-insulator Waveguides.* Optics Express, Vol. 23 (No. 17): 22628–22635, 2015.

[21] Ding, R., Liu, Y., Ma, Y., Yang, Y., Li, Q., Lim, A. E.-J., Lo, G.-Q., Bergman, K., Baehr-Jones, T., Hochberg, M.: *High-Speed Silicon Modulator With Slow-Wave Electrodes and Fully Independent Differential Drive.* Journal of Lightwave Technology, Vol. 32 (No. 12): 2240–2247, 2014.

[22] Sfar Zaoui, W., Kunze, A., Vogel, W., Berroth, M.: *CMOS-Compatible Polarization Splitting Grating Couplers With a Backside Metal Mirror.* IEEE Photonics Technology Letters, Vol. 25 (No. 14): 1395–1397, 2013.

[23] Bogaerts, W., Taillaert, D., Dumon, P., van Thourhout, D., Baets, R., Pluk, E.: *A Polarization-diversity Wavelength Duplexer Circuit in Silicon-on-Insulator Photonic Wires.* Optics Express, Vol. 15 (No. 4): 1567, 2007.

[24] Carroll, L., Gerace, D., Cristiani, I., Menezo, S., Andreani, L. C.: *Broad Parameter Optimization of Polarization-Diversity 2D Grating Couplers for Silicon Photonics.* Optics Express, Vol. 21 (No. 18): 21556–21568, 2013.

[25] Carroll, L., Gerace, D., Cristiani, I., Andreani, L. C.: *Optimizing Polarization-Diversity Couplers for Si-Photonics: Reaching the -1dB Coupling Efficiency Threshold.* Optics Express, Vol. 22 (No. 12): 14769–14781, 2014.

[26] Chen, B., Zhang, X., Hu, J., Zhu, Y., Cai, X., Chen, P., Liu, L.: *Two-dimensional Grating Coupler on Silicon with a High Coupling Efficiency and a Low Polarization-dependent Loss.* Optics Express, Vol. 28 (No. 3): 4001–4009, Feb 2020.

[27] Taillaert, D., Chong, H., Borel, P. I., Frandsen, L. H., de La Rue, R. M., Baets, R.: *A Compact Two-Dimensional Grating Coupler Used as a Polarization Splitter.* IEEE Photonics Technology Letters, Vol. 15 (No. 9): 1249–1251, 2003.

[28] Zou, J., Yu, Y., Zhang, X.: *Single Step Etched Two Dimensional Grating Coupler Based on the SOI Platform.* Optics Express, Vol. 23 (No. 25): 32490–32495, 2015.

[29] Luo, Y., Zhichao, N., Shengqian, G., Huamao, H., Yuntao, Z., Liu, L., Lidan, Z., Jian, X., Lin, L., Siyuan, Y., Xinlun, C.,: *Low-loss Two-dimensional Silicon Photonic Grating Coupler with a Backside Metal Mirror.* Optics Letters, Vol. 43(No. 3):474–477, 2018.

[30] Watanabe, T., Fedoryshyn, Y., Leuthold, J.: *2-D Grating Couplers for Vertical Fiber Coupling in Two Polarizations.* IEEE Photonics Journal, Vol. 11 (No. 4): 1–9, 2019.

[31] De La Torre Castro, P.: *Design and Simulation of Two Design and Simulation of Two Dimensional Grating Couplers in Silicon-on-Insulator Technology.* Master Thesis, University of Stuttgart, 2013.

[32] Fu, Y., Ye, T., Tang, W., Chu, T.: *Efficient Adiabatic Silicon-on-insulator Waveguide Taper.* Photonics Research, Vol. 2 (No. 3): A41–A44, 2014.

[33] Waldhäusl, R., Schnabel, B., Dannberg, P., Kley, E. B., Bräuer, A., Karthe, W.: *Efficient Coupling into Polymer Waveguides by Gratings.* Applied Opt. (Applied Optics), Vol. 36 (No. 36): 9383–9390, 1997.

[34] van Laere, F., Bogaerts, W., Dumon, P., Roelkens, G., van Thourhout, D., Baets, R.: *Focusing Polarization Diversity Grating Couplers in Silicon-on-Insulator.* Journal of Lightwave Technology, Vol. 27 (No. 5): 612–618, 2009.

[35] Verslegers, L., Mekis, A., Pinguet, T., Chi, Y., Masini, G., Sun, P., Ayazi, A., Hon, K. Y., Sahni, S., Gloeckner, S., Baudot, C., Boeuf, F., De Dobbelaere, P.: *Design of Low-Loss Polarization Splitting Grating Couplers.* In *Advanced Photonics for Communications*, page JT4A.2, 2014.

[36] Zou, J., Yu, Y., Zhang, X.: *Two-dimensional Grating Coupler with a Low Polarization Dependent Loss of 0.25 dB Covering the C-Band.* Optics Letters, Vol. 41 (No. 18): 4206–4209, 2016.

[37] Guenther, B. D. (editor): *Encyclopedia of Modern Optics.* Elsevier, Amsterdam, 2005.

[38] Soref, R., Bennett, B.: *Electrooptical Effects in Silicon.* IEEE Journal of Quantum Electronics, Vol. 23 (No. 1): 123–129, 1987.

[39] Poole, C., Darwazeh, I. (editor): *Microwave Active Circuit Analysis and Design.* Elsevier Science, 2015.

[40] Koyama, F., Oga, K.: *Frequency Chirping in External Modulators.* Journal of Lightwave Technology, Vol. 6 (No. 1): 87–93, 1988.

[41] Laser Components: *Introduction to Mach-Zehnder Modulators Bias Controllers. https:/www.lasercomponents.com*, 2019.

[42] Shi, S., Yuan, J., Huang, Q., Shi, C., Luo, X., Lu, S., Yuan, P., Yu, H., Yue, Q.: *Bias Controller of Mach-Zehnder Modulator for Electro-Optic Analog-to-Digital Converter.* Micromachines, Vol. 10(12) , 2019.

[43] Russell, P.: *Photonic Crystal Fibers.* Science (New York, N.Y.), Vol. 299 (No. 5605): 358–362, 2003.

[44] Liu, Z., Zhang, Z., Tam, H.-Y., Tao, X.: *Multifunctional Smart Optical Fibers: Materials, Fabrication, and Sensing Applications.* Photonics, Vol. 6 (No. 2): 48, 2019.

[45] Noda, J., Okamoto, K., Sasaki, Y.: *Polarization-maintaining Fibers and their Applications.* Journal of Lightwave Technology, Vol. 4 (No. 8): 1071–1089, 1986.

[46] Celler, G. K., Cristoloveanu, S.: *Frontiers of Silicon-on-Insulator.* Journal of Applied Physics, Vol. 93 (No. 9): 4955–4978, 2003.

[47] Stenmark, T., Word, R. C., Könenkamp, R.: *Determination of the Goos-Hänchen Shift in Dielectric Waveguides via Photo Emission Electron Microscopy in the Visible Spectrum.* Optics Express, Vol. 24 (No. 4): 3839–3848, 2016.

[48] Quimby, R. S.: *Photonics and Lasers: An Introduction.* Wiley-Interscience, Hoboken, NJ, 2006.

[49] Sankaran, S., O, K. K.: *A Ultra-Wideband Amplitude Modulation (AM) Detector Using Schottky Barrier Diodes Fabricated in Foundry CMOS Technology.* IEEE Journal of Solid-State Circuits, Vol. 42 (No. 5): 1058–1064, 2007.

[50] Zhang, J., Kuo, B. P.-P., Radic, S.: *64Gb/s PAM4 and 160Gb/s 16QAM Modulation Reception Using a Low-voltage Si-Ge Waveguide-integrated APD.* Optics Express, Vol. 28 (No. 16): 23266–23273, 2020.

[51] Multi-Physics Utility: *RSoft, v2014.09 User Guide. Synopsys, Inc., Optical Solutions Group.*, 2014.

[52] Li, H. H.: *Refractive Index of Silicon and Germanium and Its Wavelength and Temperature Derivatives.* Journal of Physical and Chemical Reference Data, Vol. 9 (No. 3): 561–658, 1980.

[53] FemSIM: *RSoft, v2014.09 User Guide. Synopsys, Inc., Optical Solutions Group. https://www.synopsys.com/photonic-solutions/rsoft-photonic-device-tools/passive-device-femsim.html*, 2014.

[54] Momemtum: *ADS, Keysight. Theory of Operation for Momentum: https://edadocs.software.keysight.com/display/ads2011/Theory of Operation for Momentum*, 2011.

[55] Föhn, T., Vogel, W., Schmidt, M., Berroth, M., Butschke, J., Letzkus, F.: *Optimized 90° Hybrids with Sidewall Grating in Silicon on Insulator.* Optical Fiber Communication Conference (OFC), 2014.

[56] Masetti, G., Severi, M., Solmi, S.: *Modeling of Carrier Mobility Against Carrier Concentration in Arsenic-, Phosphorus-, and Boron-doped Silicon.* IEEE Transactions on Electron Devices, Vol. 30 (No. 7): 764–769, 1983.

[57] Yu, H., Bogaerts, W.: *An Equivalent Circuit Model of the Traveling Wave Electrode for Carrier-Depletion-Based Silicon Optical Modulators.* Journal of Lightwave Technology, Vol. 30 (No. 11): 1602–1609, 2012.

[58] Chang, W. H.: *Analytical IC Metal-Line Capacitance Formulas (Short Papers).* IEEE Transactions on Microwave Theory and Techniques, Vol. 24 (No. 9): 608–611, 1976.

[59] CST: *Simulation Tool CST STUDIO SUITE by Dassault Systèmes Simulia. https://www.3ds.com/products-services/simulia/products/cst-studio-suite*, 2005.

[60] Butschke, J., Ehrmann, A., Höfflinger, B., Irmscher, M., Käsmaier, R., Letzkus, F., Löschner, H., Mathuni, J., Reuter, C., Schomburg, C., Springer, R.: *SOI Wafer Flow Process for Stencil Mask Fabrication.* Microelectronic Engineering, Vol. 46 (No. 1-4): 473–476, 1999.

[61] Jongjoo, L., Heeseok, L., Woopoung, K., Jaehoon, L., Joungho, K.: *Suppression of Coupled-Slotline Mode on CPW Using Air-bridges Measured by Picosecond Photoconductive Sampling.* IEEE Microwave and Guided Wave Letters, Vol. 9 (No. 7): 265–267, 1999.

[62] Hao, X., Xianyao, L., Xi, X., Zhiyong, L., Yude, Y., Jinzhong, Y.: *Demonstration and Characterization of High-Speed Silicon Depletion-Mode Mach–Zehnder Modulators.* IEEE Journal of Selected Topics in Quantum Electronics, Vol. 20 (No. 4): 23–32, 2014.

[63] Tu, X., Chang, K.-F., Liow, T.-Y., Song, J., Luo, X., Jia, L., Fang, Q., Yu, M., Lo, G.-Q., Dong, P., Chen, Y.-K.: *Silicon Optical Modulator with Shield Coplanar Waveguide Electrodes.* Optics Express, Vol. 22 (No. 19): 23724–23731, 2014.

[64] Besten, d. J. H.: *Integration of Multiwavelength Lasers with Fast Electro-optical Modulators.* PhD Thesis, Technische Universiteit Eindhoven, 2004.

[65] Yao, X., Jaeger, N. A. F.: *Ultra Wideband Coplanar Waveguide Based Impedance Transformer using Slow-wave Electrodes.* Proc. SPIE, Photonics North, Vol. 8007, 2011.

[66] Riaziat, M., Majidi-Ahy, R., Feng, I.: *Propagation Modes and Dispersion Characteristics of Coplanar Waveguides.* Microwave Theory and Techniques, IEEE Transactions on, Vol. 38 : 245 – 251, 1990.

[67] IHP: *Leibniz Institute for High Performance Microelectronics.*, 1983.

[68] Rahim, A., Hermans, A., Wohlfeil, B., Petousi, D., Kuyken, B., Van Thourhout, D., Baets, R.: *Taking Silicon Photonics Modulators to a Higher Performance Level: State-of-the-Art and a Review of New Technologies.* Advanced Photonics, Vol. 3, 2021.

[69] Wang, J., Qiu, C., Li, H., Ling, W., Li, L., Pang, A., Sheng, Z., Wu, A., Wang, X., Zou, S., Gan, F.: *Optimization and Demonstration of a Large-bandwidth Carrier-depletion Silicon Optical Modulator.* Journal of Lightwave Technology, Vol. 31 (No. 24): 4119–4125, 2013.

[70] Brimont, A., Thomson, D. J., Gardes, F. Y., Fedeli, J. M., Reed, G. T., Marti, J., Sanchis, P.: *High-Contrast 40 Gb/s Operation of a 500 μm Long Silicon Carrier-depletion Slow Wave Modulator.* Optics Letters, Vol. 37 (No. 17): 3504–3506, 2012.

[71] Azadeh, S. S., Merget, F., Romero-García, S., Moscoso-Martir, A., von den Driesch, N., Müller, J., Mantl, S., Buca, D., Witzens, J.: *Low V(pi) Silicon Photonics Modulators with Highly Linear Epitaxially Grown Phase Shifters.* Optics Express, Vol. 23 (No. 18): 23526–23550, 2015.

[72] Li, M., Wang, L., Li, X., Xiao, X., Yu, S.: *Silicon Intensity Mach-Zehnder Modulator for Single Lane 100 Gb/s Applications.* Photonics Research, Vol. 6 (No. 2): 109–116, 2018.

[73] Goi, K., Ogawa, K., Tan, Y. T., Dixit, V., Lim, S. T., Png, C. E., Liow, T.-Y., Tu, X., Lo, G.-Q., Kwong, D.-L: *Silicon Mach-Zehnder Modulator Using Low-Loss Phase Shifter with Bottom PN Junction Formed by Restricted-Depth Doping.* IEICE Electronics Express, Vol. 10 : 20130552, 2013.

[74] Li, K., Liu, S., Thomson, D. J., Zhang, W., Yan, X., Meng, F., Littlejohns, C. G., Du, H., Banakar, M., Ebert, M., Cao, W., Tran, D., Chen, B., Shakoor, A., Petropoulos, P., Reed, G. T.: *Electronic–photonic convergence for silicon photonics transmitters beyond 100 Gbps on–off keying.* Optica, Vol. 7 (No. 11): 1514–1516, 2020.

[75] Xu, H., Xiao, X., Li, X., Hu, Y., Li, Z., Chu, T., Yu, Y., Yu, J.: *High Speed Silicon Mach-Zehnder Modulator based on Interleaved PN Junctions.* Optics Express, Vol. 20 (No. 14): 15093–15099, 2012.

[76] Giesecke, A. L., Prinzen, A., Füser, H., Porschatis, C., Lerch, H., Bolten, J., Suckow, S., Chmielak, B., Wahlbrink, T.: *Ultra-efficient Interleaved Depletion Modulators by Using Advanced Fabrication Technology.* In *42nd European Conference on Optical Communication*, Berlin and Offenbach, 2016.

[77] Liao, L., Liu, A., Rubin, D., Basak, J., Chetrit, Y., Nguyen, H., Cohen, R., Izhaky, N., Paniccia, M.: *40 Gbit/s Silicon Optical Modulator for High-Speed Applications.* Electronics Letters, Vol. 43 (No. 22): 1196, 2007.

[78] Föhn, T., Hoppe, N., Vogel, W., Schmidt, M., Félix Rosa, M., Berroth, M., Butschke, J., Letzkus, F.: *3D-simulation and Charac-*

terization of Subwavelength Grating Waveguides in SOI. Proceedings of the International Conference on Numerical Simulation of Optoelectronic Devices, NUSOD, pages 137–138, 2014.

Personal publications

[P.1] Sfar Zaoui, W.; **Félix Rosa, M.**; Vogel, W.; Berroth, M.; Butschke, J. and Letzkus, F.: *High-Efficient CMOS-Compatible Grating Couplers with Backside Metal Mirror* In: *European Conference on Optical Communication (ECOC)*, 2012.

[P.2] Sfar Zaoui, W.; **Félix Rosa, M.**; Vogel, W. and Berroth, M.: *Grating Coupler Serving as Polarization Beam Splitter in Silicon-On-Insulator Platform* In: *7th Joint Symposium on Opto-and Microelectronic Devices and Circuits (SODC)*, 2012.

[P.3] Sfar Zaoui, W.; **Félix Rosa, M.**; Vogel, W.; Berroth, M.; Butschke, J. and Letzkus, F.: *Cost-effective CMOS-compatible grating couplers with backside metal mirror and 69% coupling efficiency* In: *Optics Express, Vol. 20, No. 26, B238 - B243*, 2012.

[P.4] Föhn, T.; Hoppe, N.; Vogel, W.; Schmidt M.; **Félix Rosa, M.**; Berroth, M.; Butschke, J. and Letzkus, F.: *3D-Simulation and Characterization of Subwavelength Grating Waveguides in SOI* In: *14th International Conference on Numerical Simulation of Optoelectronic Devices (NUSOD)*, 2014.

[P.5] Berroth, M.; Föhn, T.; Sfar Zaoui, W.; **Félix Rosa, M.**; Hoppe, N.; Vogel, W.; Butschke, J.; Letzkus, F. and Kaschel, M.: *Subwavelength Structures for Advanced Silicon Photonic Circuits* In: *Optische Komponenten für Cloud-Datacenter, 12. ITG-Workshop der ITG-Fachgruppe 5.3.2, Seiten 25–26*, 2015.

[P.6] **Félix Rosa, M.**; Ferenci, D.; Föhn, T.; Vogel, W.; Berroth, M.; Kaschel, M.; Schmidt, M.; Oehme, M; Kasper, E. and Schulze, J.: *High speed opto-electronic receiver with a 3-dB bandwidth of* 22 GHz In: *International Symposium on Microwave and Optical Technology (ISMOT)*, 2015.

[P.7] Hoppe, N.; Föhn, T.; **Félix Rosa, M.**; Vogel, W.; Sfar Zaoui, W.; Kaschel, M.; Butschke, J.; Letzkus, F. and Berroth, M.: *Integrated Dual-Mode Waveguide Interferometer* In: *15th International Conference on Numerical Simulation of Optoelectronic Devices (NUSOD)*, 2015.

[P.8] Vogel, W.; Föhn, T.; Hoppe, N.; **Félix Rosa, M.** and Rathgeber, L.: *Siliziumphotonik für Datacom-Anwendungen* In: *Workshop Photonics ,IMS Chips*, 2016.

[P.9] Hoppe, N.; Rothe, C.; Föhn, T.; **Félix Rosa, M.**; Rathgeber, L.; Vogel, W.; Ludwigs, S. and Berroth, M.: *Zweimoden-Interferometer in optischen organischen Silizium-Hybrid-Modulatoren* In: *Kleinheubacher Tagung*, 2016.

[P.10] **Félix Rosa, M.**; Rathgeber, L.; Föhn, T.; Hoppe, N.; Schmidt, M.; Vogel, W.; Berroth, M. and Kaschel, M.: *Design and Simulation of Silicon Optical Modulators in Silicon-on-Insulator Technology* In: *Kleinheubacher Tagung*, 2016.

[P.11] Hoppe, N.; Föhn, T.; Diersing, P.; Scheck, P.; Vogel, W.; **Félix Rosa, M.**; Kaschel, M.; Bach, M. and Berroth, M.: *Design of an Integrated Dual-Mode Interferometer on* 250 nm *Silicon-on-Insulator* In: *IEEE Journal of Selected Topics in Quantum Electronics*, 2016.

[P.12] **Félix Rosa, M.**; de la Torre Castro, P.; Hoppe, N.; Rathgeber, L.; Vogel, W. and Berroth: *Novel Design of Two-Dimensional Grating Couplers with Backside Metal Mirror in* 250 nm *Silicon-on-Insulator* In: *International Conference on Numerical Simulation of Optoelectronic Devices (NUSOD)*, 2017.

[P.13] Hoppe, N.; Haug, M.; Vogel, W.; **Félix Rosa, M.**; Föhn, T.; Rathgeber, L. and Berroth, M.: *Packaging Process for Efficient Coupling Using a Grating Coupler with Backside Mirror* In: *International Conference on Numerical Simulation of Optoelectronic Devices (NUSOD)*, 2017.

[P.14] Hoppe, N.; Rothe, C.; Celik, A.; **Félix Rosa, M.**; Vogel, W.; Widmann, D.; Rathgeber, L.; Carmen Ruiz Delgado, M.; Villacampa, B.; Ludwigs, S. and Berroth, M.: *Single waveguide silicon-organic hybrid modulator* In: *Advances in Radio Science, 15, 141-147*, 2017.

[P.15] Hoppe, N.; Haug, M.; Polder, T.; **Félix Rosa, M.**; Vogel, W.; Scheck, P.; Rathgeber, L.; Widmann, D. and Berroth, M.: *Sealed and Compact Fiber Links to Integrated Photonics Using Grating Couplers* In: *IEEE International Conference on Group IV Photonics*, 2017.

[P.16] **Félix Rosa, M.**; Rathgeber, L.; Elster, R.; Hoppe, N.; Föhn, T.; Schmidt, M.; Vogel, W. and Berroth: *Design of a carrier-depletion Mach-Zehnder modulator in* 250 nm *silicon-on-insulator technology* In: *Advances in Radio Science, 15, 269-281*, 2017.

[P.17] Dreyer, F.; Hoppe, N.; Köhler, J.; Vogel, W.; Dahlinger, M.; **Félix Rosa, M.**; Rathgeber, L.; Werner, J. and Berroth, M.: *Schottky-Fotodioden basierend auf laserkristallisierten Germanium-Schichten* In: *Kleinheubacher Tagung*, 2017.

Acknowledgement

Many people helped me along the way on this journey. I would like to thank all of them who helped me directly or indirectly during this work.

I thank Prof. Berroth for giving me the opportunity to work on this research topic at the INT. Thank you for the support and motivation until the end of my work.

I also thank Prof. Frühauf for agreeing to be the co-reporter of my work.

I would like to thank all the INT-Team. You all were always ready to help me when I had questions. I would like to acknowledge Wissem Sfar Zaoui since working with you as student introduced me to the amazing optical world. Special thanks to the optical group leader Wolfgang Vogel and my optical group colleagues Thomas Föhn, Niklas Hoppe and Lotte Nagy. You made the time and work with you very special. I will not forget the enjoyable time that I spent with the lunch group. Each work break with you was an injection of energy and fun.

I am very grateful to Matthias Buck and Martin Schmidt for proofreading this dissertation, for all the constructive discussions and support during all these years.

Many thanks to the students for their support that contributed to the accomplishment of this work.

I am also thankful to Martin Pohl and Michael Huonker for the motivation and for allowing me to find time to write my dissertation.

Words cannot express my gratitude to my parents and my sister. You are the best that I have. With your unlimited support and faith in me, you motivate me with all what I intend to do.

Special thanks to Santi, Youssef and Sandra because you are always there when I need you.

To all my family and friends, thank you for letting me know that you are proud of me. This gives me the energy to keep going.

Thank you Patri, because you taught me to fight and never give up.